MODELLING, ANALYSIS AND DEVELOPMENT OF HOMOGENOUS SCAFFOLD-BASED CUSTOMIZED CRANIAL IMPLANTS

Submitted in partial fulfillment of the requirements

for the award of the degree of

Doctor of Philosophy

by

V PHANINDRA BOGU

Roll No: 714018

Under the Supervision of

Dr. Y. Ravi Kumar
Associate Professor, MED

and

Dr. Asit Kumar Khanra
Associate Professor, MMED

Department of Mechanical Engineering
NATIONAL INSTITUTE OF TECHNOLOGY
WARANGAL – 506004
Telangana State, INDIA.
August - 2018

THESIS APPROVAL FOR Ph.D.

This thesis entitled **"Modelling, Analysis and Development of Homogenous Scaffold-based Customized Cranial Implants"** by **Mr. V Phanindra Bogu** is approved for the degree of Doctor of Philosophy.

(External Examiner)

Dr. Y. Ravi Kumar
Supervisor

Associate Professor, Department of Mechanical Engineering, NIT Warangal

Dr. Asit Kumar Khanra
Co-Supervisor

Associate Professor, Department of Metallurgical and Materials Engineering, NIT Warangal

Prof. P. Bangaru Babu
Chairman and Head

Department of Mechanical Engineering, NIT Warangal

NATIONAL INSTITUTE OF TECHNOLOGY

WARANGAL – 506 004, Telangana State, INDIA

CERTIFICATE

This is to certify the thesis entitled **"Modelling, Analysis and Development of Homogenous Scaffold-based Customized Cranial Implants"** submitted by **Mr. V Phanindra Bogu** for, Roll No. 714018, to **National Institute of Technology, Warangal** in partial fulfilment of the requirements for the award of the degree of **Doctor of Philosophy in Mechanical Engineering** is a record of bonafide research work carried out by him under our supervision and guidance. This work has not been submitted elsewhere for the award of any degree.

Place: Warangal.

Date:

Dr. Y. Ravi Kumar
Supervisor
Associate Professor,
Department of Mechanical Engineering,
National Institute of Technology,
Warangal, Telangana State.

Dr. Asit Kumar Khanra
Co-Supervisor
Associate Professor,
Department of Metallurgical and Materials Engineering,
National Institute of Technology,
Warangal, Telangana State.

NATIONAL INSTITUTE OF TECHNOLOGY

WARANGAL – 506 004, Telangana State, INDIA

DECLARATION

This is to certify that the work presented in the thesis entitled **"Modelling, Analysis and Development of Homogenous Scaffold-based Customized Cranial Implants"**, is a bonafide work done by me under the supervision of **Dr. Y. Ravi Kumar**, Associate Professor, Department of Mechanical Engineering, NIT Warangal, India & **Dr. Asit Kumar Khanra,** Associate Professor, Department of Metallurgical and Materials Engineering, NIT Warangal, India and has not been submitted for the award of any degree to any other University or Institute.

I declare that this written submission represents my ideas in my own words and where ever others ideas or words are included have been adequately cited and referenced with the original sources. I also declare that I have adhered to all principles of academic honesty and integrity and have not misrepresented or fabricated or falsified any idea/data/fact/source in my submission. I understand that any violation of the above will cause for disciplinary action by the institute and can also evoke penal action from the sources which have thus not been properly cited or from whom proper permission has not been taken when needed.

Place: Warangal. **V Phanindra Bogu**

Date: **Roll No. 714018**

Dedicated to my goddess "Shyamala Devi"

Gurus, My Parents & Brothers.

ఆవి'ర్భూతం చ' సృష్ట్యాదౌ ప్రకృతే"ఃపురుషాత్ప'రమ్

ACKNOWLEDGEMENTS

Firstly, I would like to express my sincere gratitude to my beloved supervisor **Dr. Y. Ravi Kumar,** Associate professor, Department of Mechanical Engineering for the continuous support during my research work, for his patience, motivation, and immense knowledge. His guidance helped me in all the time of research and writing of this thesis. I could not have imagined having a better advisor and tremendous mentor for my Ph.D. study. His advice on both research as well as on my career have been priceless. Without his guidance and persistent help this dissertation would not have been possible.

My heart fully thanks to my Co-Supervisor **Dr. Asit Kumar Khanra,** Associate Professor, Department of Metallurgical and Materials Engineering for his excellent supervision, skilled guidance, unfailing support, stimulating discussions, critical evaluation and constant encouragement during this dissertation work. I thank him for his time and efforts for making me a better researcher. I am extremely thankful to him for spending his valuable time in spite of his busy schedule.

I am very much thankful to **Prof. P. Bangaru Babu**, Head, and Mechanical Engineering Department for his support and also valuable suggestions. I would like to extend my sincere thanks to my Doctoral Scrutiny Committee members, **Prof. R.V. Chalam**, Professor, Department of Mechanical Engineering, **Prof. L. Krishnanand**, Professor, Department of Mechanical Engineering, and **Dr. Abdul Azeem P**, Associate Professor, Department of Physics for serving as my committee members. I would also like to thank them for their insightful comments and encouragement, but also for the hard question which incented me to widen my research from various perspectives.

I express my sincere thanks to the Director, National Institute of Technology, Warangal for providing necessary facilities for my research and for the encouragement by providing necessary financial assistance for attending the conferences.

I am also grateful to **Dr. MohanRaj Bogu,** Scientist, Hyderabad, **Dr. Gireesh Bogu,** Postdoctoral Research Fellow, Department of Genetics, and Stanford University, USA for providing help in the direction of human anatomy and tissue engineering. Without their precious support it would not be able to conduct this research.

I take this opportunity to express gratitude to the entire faculty members of Mechanical Engineering Department for their help and support.

I would like to thank administrative and technical staff members of the institute who have been kind enough to advise and help in their respective roles.

I thank my friends **V. Venkateswarlu, K.V. Koteswararo,** and **J. Rahul** for all the fun we have had in the last four years. Also I thank my co-researchers **Dr. A. Manmadhachary, G. Venkatesh, M. Santosh Kumar, S. Rakesh** and M.Tech students **Madhu M.N, L. Daloji, Nrupendranath .I** and **G. Sachin.**

A special thanks to my parents **Mrs. Krishna Kumari** and **Mr. Bogu Anjaiah** for the unceasing encouragement, support, attention and for all of the sacrifices they have made on my behalf and incented me to strive towards my goal.

V Phanindra Bogu

ABSTRACT

Cranioplasty is one of the oldest and lifesaving surgical procedure in order to repair cranial defects and extremely challenging for most experienced neurosurgeons. Cranioplasty often performs an aesthetic purpose, improves neurological function of brain tissue, and arrest cerebrospinal fluid leak (CSF). Earliest, the cranial defect reconstruction is performed through autografts, allografts and biocompatible materials such as gold, stainless steel, titanium and various polymer materials. These surgical procedures are gradually improved and enhanced with the help of computer-aided design (CAD) and computer-aided manufacturing (CAM) technologies. Recently, these surgical procedures are notoriously enhanced with 3D printing technology which helps to manufacture large-sized cranial defects with contour surface.

The main objective of this research work is to develop the customized cranial implants for severely injured patients. The computer-aided modelling and reconstruction techniques are creating an essential role in various cranial defects such as symmetrical and asymmetrical defects respectively. The symmetrical defects are modelled through mirroring technique, however, modelling of cranial implants for asymmetrical defects is quite difficult such as beyond midline deformities, multipoint defects and frontal bone defects. The complexity depends upon the surface area of the implant and curvature, whenever these defects are less than 5 cm^2 almost flat surface, which is considered as small defects and the large defects are in the order of >100 cm^2 .

The first part of this research is started with modelling of the cranial implant through mirroring technique. The skull is damaged in frontal, parietal and temporal regions and a small portion of frontal region damaged away from the sagittal plane. The cranial bone thickness is calculated at different regions such as temporal and parietal regions etc. The implant is modelled at a thickness of 2.5mm and the edges of the implant are corrected to arrest the CSF leak. Here, the complexity is to maintain the curvature and implant thickness is constrained. To overcome these limitations the computer-aided reconstruction technique is developed.

In the second part of the research, the above mentioned limitations are overwhelmed through computer-aided reconstruction technique, which can handle various cranial defects such as symmetrical and partially asymmetrical defects. This technique is involved with systematic steps such as section the skull, draw the line at each section and develop the surface patch, which can fit damage skull. This surface is extruded longitudinally at 4 mm of thickness to withstand at intracranial pressure (ICP) and the normal ICP range is varying from 7 to 15 mm of Hg.

Additionally, the finite element analysis is conducted on the cranial implant under ICP with a minimum number of anatomical locations. The anatomical locations allow the implant behaviour with respect to intracranial pressure conditions. However, increased anatomical locations lead to variation in deformation and equivalent stress. The implant is designed with eight fixation points and ten fixation points respectively. Consequently, the mechanical deformation and equivalent stress (von Mises) are calculated in ANSYS 15 software with distinctive material properties such as titanium alloy (Ti6Al4V), polymethyl methacrylate (PMMA) and polyether ether ketone (PEEK). It is observed that Ti6Al4V material shows low deformation and PEEK material shows less equivalent stress. However, this implant is completely solid one which required to promote tissue regeneration. In this aspect, the implant is embed with optimum permeable scaffold structures.

The third part of the research is discussed with the permeability of scaffold structures. The tissue engineering aims at the development of biological substitutes that restore, maintain and improve tissue function. The tissue scaffolds provide structural support for cell attachment and subsequent tissue growth. In this work, homogeneous interconnected scaffold structures are modelled by variable pore-size, porosity, various strut cross-section and keeping the uniform unit cell size. The CFD analysis is done in ANSYS 15 software to know the permeability of scaffold with blood properties as a fluid. The Permeability is found to be in the range of $4.8\times10^{-9}\ m^2 - 2.3\times10^{-8}\ m^2$ for strut cross-section 300 to 500 μm. the cross-section of the strut and porosity are the influencing parameters and plays important role in scaffold design. Among all cross sections, the circular section shows effective permeability. The solid implant is embedded with unit cell based scaffold structures to mimic the original cranial bone.

The final part of the research is discussed with a novel free-form closed curve network (FCN) technique which is successfully developed to model the cranial implant. This modelling methodology is the easiest one and addressing both the symmetrical and asymmetrical defects. The implant is embedded in a unit cell based porous structure with the help of an algorithm, and this algorithm is simple to manage the consistency in porosity and pore size of the scaffold. Totally six types of implants are modelled with variation in porosity and replicate the original cranial bone. Among six implants, Type 2 (porosity 82.62%) and Type 5 (porosity 45.73%) implants are analysed with the meshless approach under ICP. The total deformation and equivalent stress (von Mises stress) of porous implants are compared with the solid implant under same ICP conditions. Consequently, distinctive materials are used for structural analysis such as titanium alloy

(Ti6Al4V) and polyether-ether-ketone (PEEK), respectively. It is observed from the results that the titanium-based solid implant is showing optimum results in deformation aspect while considering weight and cost the PEEK based Type 5 implant is most appropriate.

The entire research work made an attempt to develop innovative possibilities in cranial implant modelling techniques. These techniques can handle symmetrical and asymmetrical defects and effectively model the cranial implant with optimum number of fixation points, which help to arrest the CSF leak. Finally, to develop the porous cranial implant, which mimics the cranial bone in order to enhance tissue regeneration.

TABLE OF CONTENTS

LIST OF FIGURES

LIST OF TABLES

ABBREVIATIONS

2D	2-Dimenstional
3D	3-Dimenstional
3DP	3-Dimensional printing
ABS	Acrylonitrile butadiene styrene
AM	Additive manufacturing
ASCII	American standard code for information interchange
CAD	Computer aided design
CFD	Computational fluid dynamics
CSF	Cerabrospinal fluid
CT	Computed tomography
DICOM	Digital imaging and communication in medicine
DMD	Direct metal deposition
DMLS	Direct metal laser sintering
EBM	Electron beam melting
EFC	Epidural fluid collection
FCN	Freeform closed curve network technique
FDA	Food and drug administration's
FDM	Fused deposition modelling
FEA	Finite element analysis
FVM	Finite volume method
HU	Hounsfield unit
ICP	Intracranial pressure
LENS	Laser engineered net shaping
MIMICS	Materialize interactive medical image control system
MRI	Magnetic resonance imaging
NURBS	Non-uniform rational B-spline
PLA	Poly lactic acid
PEEK	Polyether ether ketone
PMMA	Poly methyl methacrylate

RP	Rapid prototyping
SLA	Stereolithography apparatus
SLM	Selective laser melting
SLS	Selective laser sintering
SOT	Syndrome of trephined
STL	Stereolithography
STL	Standard tessellation language
US	Ultrasound scanning
UV	Ultraviolet

CHAPTER 1
1. INTRODUCTION

1.1 Anatomy of the skull

The skull is composed of various bones and it is the most complex in nature. The skull is divided in to facial and cranial bones as shown in Figure 1.1 [1]. The cranial bones combined to call it as cranium, this cranium is enclosed and protect the brain and attached to head and neck muscles.

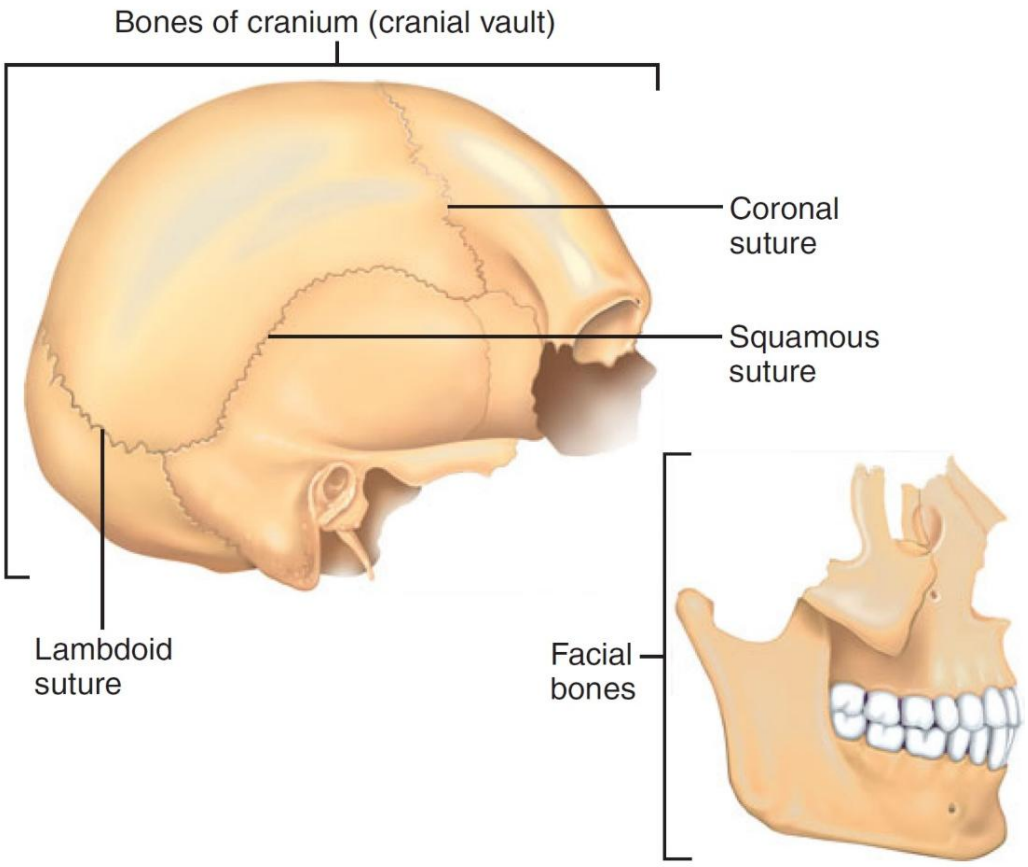

Figure 1.1 Cranial and facial divisions of the skull [1]

Most of the skull bones are non-load bearing bones. The flat bones are firmly united by interlocking, immovable joints are called sutures. These suture lines are appeared as irregular saw-toothed [1]. The longest sutures are the coronal, sagittal, squamous, and lambdoid sutures which connect the cranial bones. Moreover, the skull has 85 openings such as foramina, canals, fissures etc. Most importantly these provide passageways for the spinal cord, the major blood vessels serving the brain, and the 12 pairs of cranial nerves, which conduct impulses from the brain.

1.2 Cranial bones

The group of cranial bones are called cranium, the cranium is surrounds and protect the brain from external loads. The cranium is combination of occipital, parietal, frontal, temporal bones etc. as shown in the Figure 1.2. Among these cranial bones, the parietal, frontal and occipital are categorized as flat bones [1]. The two large parietal (i.e. wall) bones, look like a large curved rectangles, these parietal bone are greater part of the skull and act as lateral walls of the skull. The four longest sutures are formed between the parietal bones and adjacent cranial. The sutures are joint portion or unioned portions of the skull, it appeared as zig-zag patterns.

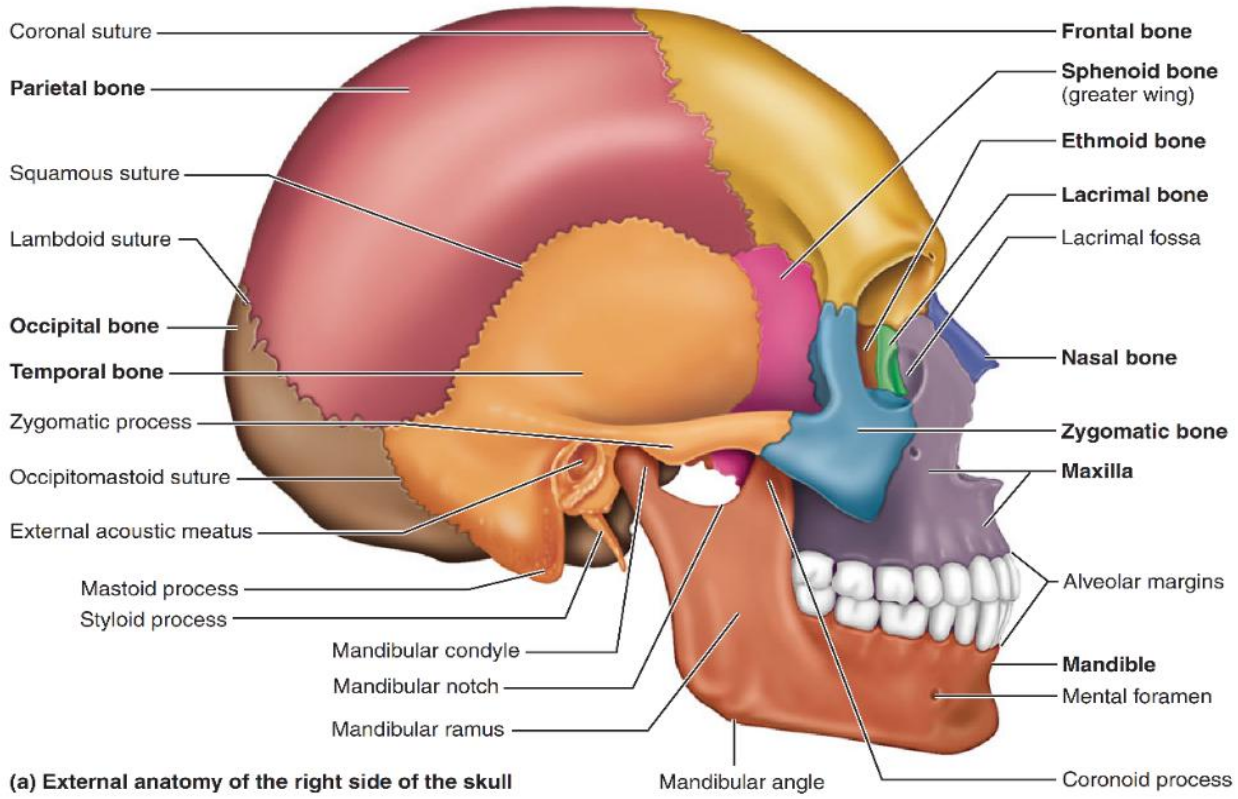

Figure 1.2 Lateral view of the skull [1]

1.3 Intracranial pressure (ICP)

The skull protects the brain from the injury, the meninges is present in between the skull and brain and the meninges is surrounding the brain and protection of the spinal cord. The choroid plexuses are capillary rich membranes which are located at brain ventricles, these choroid plexuses are produce of cerebrospinal fluid (CSF) and returns at a at rate of 500 ml per day as shown in Figure 1.3. The CSF is the clear fluid, it runs through the central canal of the spinal cord and quantitatively

high amount is at subarachnoid space through the lateral and median apertures [1]. The CSF is continuously circulating from spinal to brain.

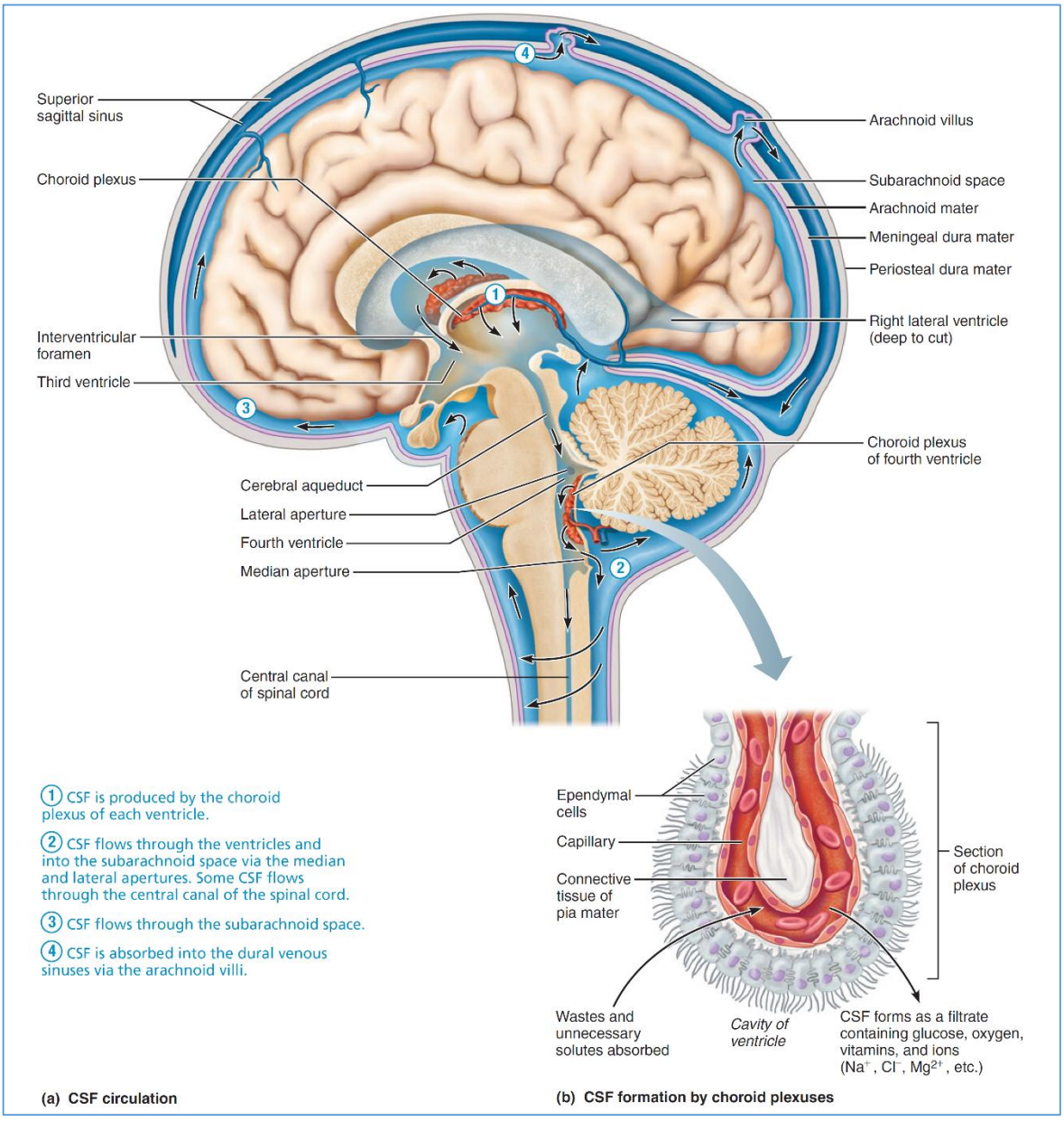

Figure 1.3 Formation, location and circulation of CSF a) Location and circulatory pattern of cerebrospinal fluid (CSF). Arrows indicate the direction of flow. b) Each choroid plexus consists of a knot of porous capillaries surrounded by a single layer of ependymal cells joined by tight junctions and bearing long cilia. Fluid leaking from porous capillaries is processed by the ependymal cells to form the CSF in the ventricles [1]

The Intracranial pressures is changes with respect to age and sex of the humans. The raised in ICP leads various adverse effects on human body such as intracranial mass lesions, disorders of CSF circulation, or more diffuse pathological processes. The ischemia is caused due to raise in ICP and

impede the CBF (cerebral blood flow). Normal range of ICP is varied from 7 to 15 mm of Hg for healthy adults in supine position, however in vertical position the ICP is about 10 mm of Hg. The ICP range varied for infants 1.5-6 mm of Hg and for children's 3–7 mm of Hg [2].

1.4 Bone structure and properties

The bone is hierarchical and complicated structure, at each level of bone the mechanical and biological functions are varied. The bone structure is divided in various levels signified by scale such as macroscale, microscale and nanoscale as shown in Figure 1.4. The microscale and nanoscales are sub classified into sub-microscale and sub-nanoscale [3]. The shape of bone which can see with naked eye call as macroscale level, majorly the bone is composed of cortical bone (compact bone) and trabecular bone (spongy bone).

The bone is natural composite which contains organic and inorganic components, the organic components are collagen and fibrillin materials [4]. The collagen is sub classified in to type-I, type-III and type-IV, subsequently the main inorganic component is hydroxyapatite which is crystalline material and substitutes the bone at 70% by weight and 50% by volume [3]. The structure of bone was replicates reinforced concreate structures as a composition of steel rod and cement, like hydroxyapatite crystals and collagen. This composition is enhanced the flexibility, strength and toughness. The Type-I collagen is an essential and primary organic component of the bone, in the Nano level the diameter 1.5 nm and 300 nm in length. The hydroxyapatite crystal is replicate the plate shaped of 50x25 nm area and thickness is 1.5-4 nm [5].

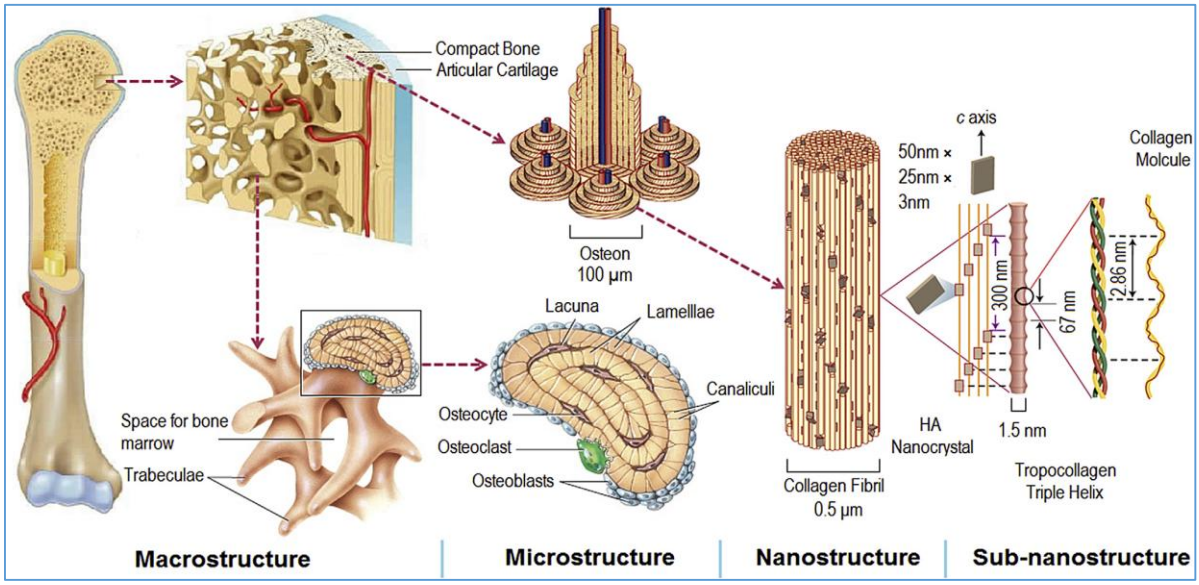

Figure 1.4 Bone structure in different levels [3]

1.4.1 Compact bone

The compact bone is appears as solid with naked eye, when this compact bone examined microscopically it is having 3-5% of spaces to support blood vessels, osteocytes and nerves. The compact bone is mainly composed of osteon, which act as structural component. The osteons are

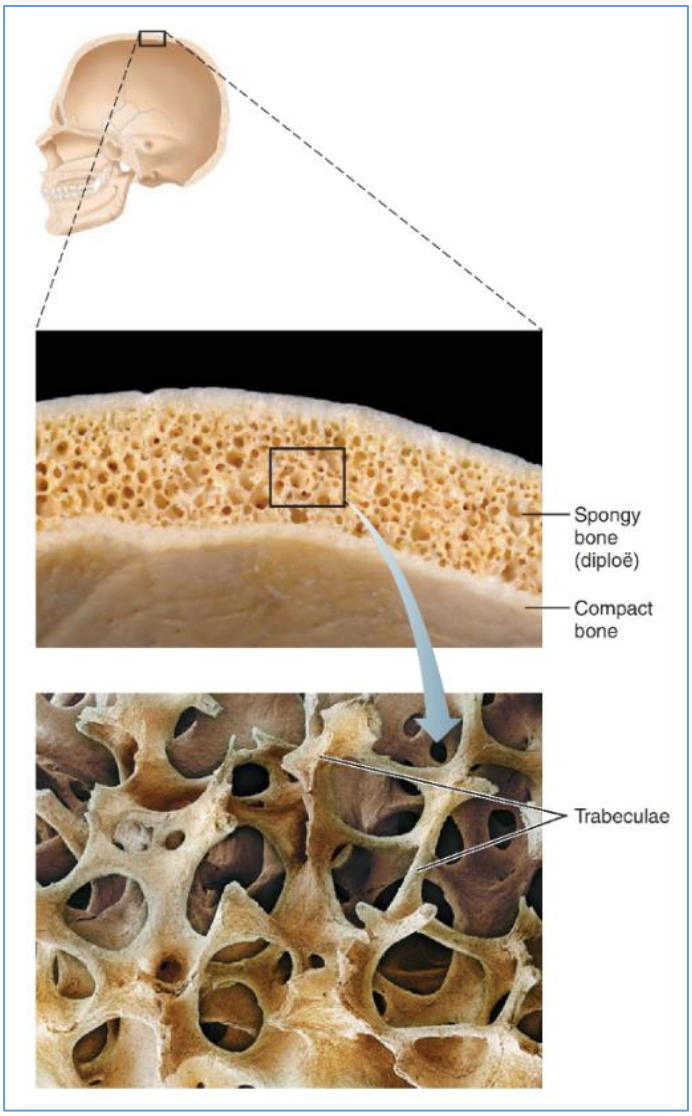

Figure 1.5 Structure of a flat bone. It consists of layer of spongy bone (the dipole) sandwich between two thin layers of compact bone [1, 37]

long cylindrical structure and oriented parallel to the long axis of bone, additionally this structure assist to sustain at compressive loads [1], [3]. Microscopically the osteons are appeared as gathering of concentric tubes, these tubes are called lamella (little plate) as shown in Figure 1.4. The collagen fibres and hydroxyapatite crystals are attached and settled in opposite directions to the lamella, due to this alternating arrangement, the bone is withstand under stresses and torsional

loads. The lamella is inhibit to crack propagation while this crack is progressively increased into deeper parts which appeared as fracture.

1.4.2 Spongy bone

The compact bone is also called spongy bone or trabecular bone, the trabecular bone is less complex structure than compact bone as shown in Figure 1.4. This bone is observed as large spaces and filled with bone marrow, the porosity is varied with age and sex in the range of 50 to 90% [4], [6]. The each trabecula consists of lamella and osteocytes, however, the presence of osteons and blood vessels are less percentage. The osteocytes receive their nutrients through this spongy bone, this bone is arranged as building blocks of osteons which are of the size 10-500 μm [4], [6].

1.4.3 Cranial bone anatomy

The flat bones and long bones have same composition, however, the shape is different. The femur bone is cylindrical in shape having diaphysis in contrast the flat bone is absence of diaphysis as shown in Figure 1.5. The flat bone is composed of compact bone and trabecular bone, the compact bone is denser and protecting the spongy bone, this spongy bone is called dipole (double) [1]. The flat bone is replicating the sandwich structure, which means high strength material is covered the low strength material. The spongy bone contains bone marrow while consider the cranial bone no marrow cavity was observed.

1.5 Head injury

The head injuries are most common cause of the death and disability of the patient, the head injuries most notably increasing day by day about 1.7 million people per year [7]. These head injuries are mentioned as brain injury or traumatic brain injury (TBI) which leads to the skull fracture, internal bleeding and damage to the brain.

The root cause of injuries are happened due to sudden impact of the objects which is harder than the skull. The injury (blow to the skull) is occurred due to penetration or impact of the object which leads to fracture of the skull as shown in the Figure 1.6 A [8]. The depressed portion (pink colour) of the skull is compressed the brain tissue. The blow of the skull is caused in the brain, however, the skull fracture is not identified. Due to this subdural hematoma may develop as shown in the Figure 1.6 B [8]. The sudden impact of the head to the surface which results in the injury has occurred opposite to the point of impact, this is called as countercoup injury as shown in the Figure 1.6 C [8]. These injuries are cause the brain dysfunction or damage and it leads to ischemia,

cerebral edema, and elevated intracranial pressure. The common term in head injury is concession, which describes the sudden loss of awareness and alertness of the patient for few minutes.

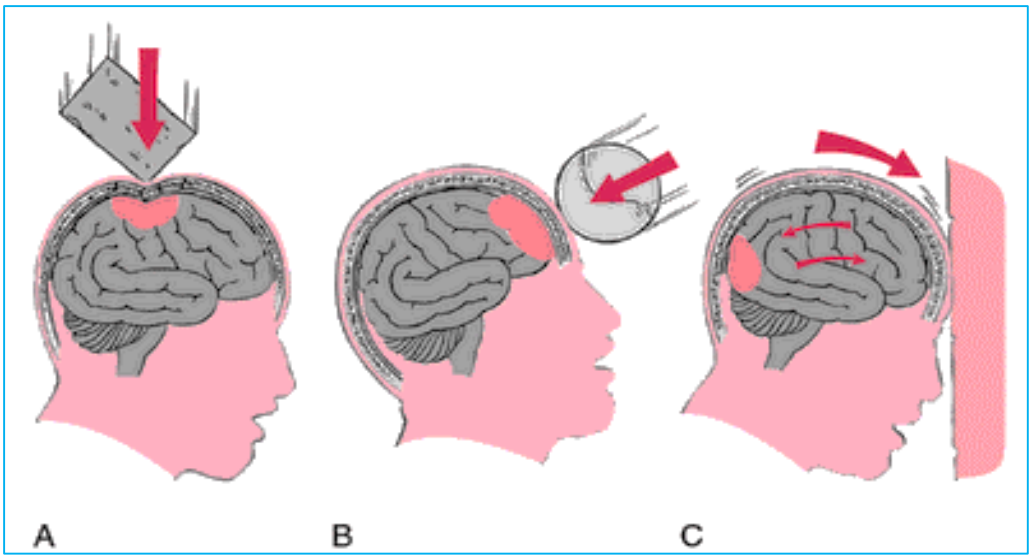

Figure 1.6 Head injuries A) Penetration or impact of the object cause skull fracture B) Impact of ball causes hematoma C) Sudden impact of head causes countercoup injury [8]

1.5.1 Types of skull fractures

The skull fractures or injuries are majorly classified as Linear, Depressed, Diastatic and Basilar [9], [10].

I. **Linear skull fractures.** These type of fractures are occurred commonly, it is observed that a linear crack is passing on the bone as shown in Figure 1.7. In this fracture, the bone will break but not separated. These patients are required to observe by the doctor in the hospital for a brief amount of time and they recover within few days. Surgical intervention is not necessary.

II. **Depressed skull fractures.** The specific area of the bone is sunken due to sudden impact of an object on the head is called as depressed skull fracture as shown in Figure 1.7 [8], [10]. These fractures are observed that with or without a cut in the scalp. This depressed fracture is treated through surgical intervention, the bone flaps are removed and cover the sunken area with cranial implant depending on severity.

III. **Diastatic skull fractures.** The diastatic fracture occurred along the suture of the cranial bones, these sutures are junctions of cranial bones as shown in Figure 1.7. These sutures are fused the cranial bones when we were children. These type of fractures are most probably occurred in new-borns and older infants. Moreover, this fracture leads to widened normal suture lines.

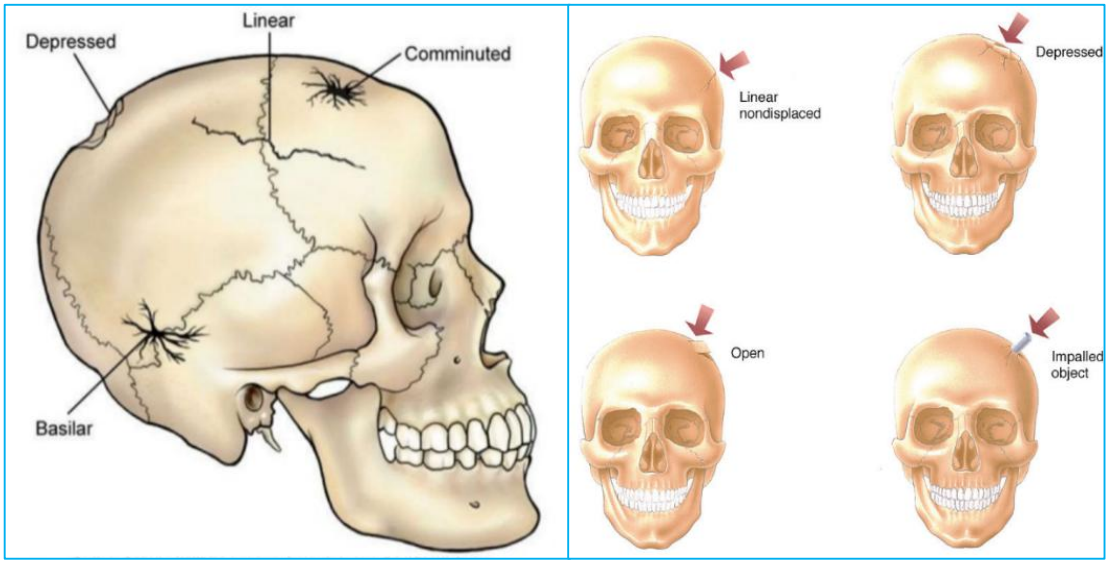

Figure 1.7 Types of skull fractures [8,10]

IV. **Basilar skull fractures.** This most serious type of fracture need to observation of patient under the supervision of surgeons. In this fracture, a break is observed at the base of the skull as shown in Figure 1.7. This fracture leads to create terrible damage to the patient such as bruises around eye and behind the ear. Additionally, a clear fluid draining from their nose or ears due to a tear in part of the covering of the brain.

Along with above skull fractures, the skull defects are classified into symmetrical defects and asymmetrical defects. The sagittal plane is the midline for the skull, the skull is damaged beyond the sagittal plane is called asymmetrical defect otherwise it is called symmetrical defects. The skull is not symmetrical about coronal and transverse planes as shown in Figure 1.8 [11].

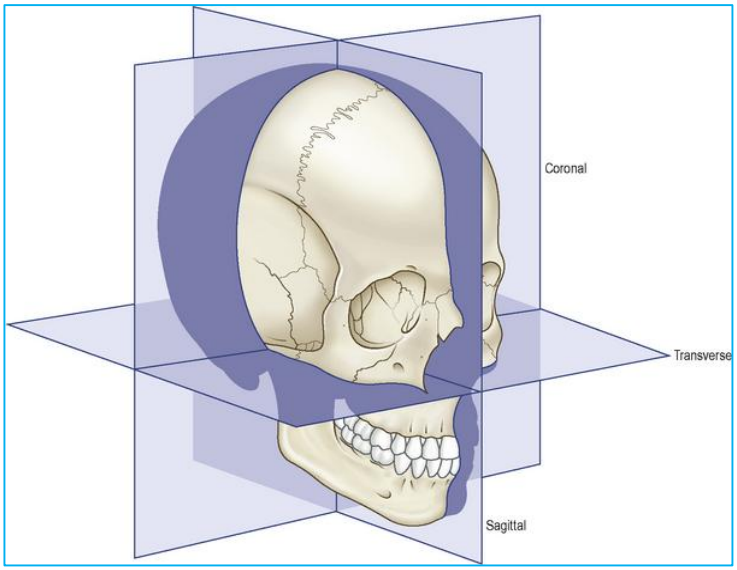

Figure 1.8 Anatomical planes [11]

Anatomically the skull is the symmetrical part for many humans. In symmetrical defect, the malformation portion can be planned with contralateral side of the skull through computer aided modelling software. Modelling of an implant for asymmetrical defects is quite challenging because mirroring of contralateral side of the skull cannot be possible. These defects deal with multi-point deformities and beyond midline deformities [12].

1.6 Medical models through 3D printing

In order to manufacture the 3D bio models for human life systems to understand problem clearly by the surgeons. The 3D bio models are developed with the help of Therapeutic imaging procedures, for example, Computed Tomography (CT) and Magnetic Resonance Imaging (MRI) or Ultrasound Scanning (US). The CT data is for hard tissue observation and others are for soft tissue observation. The CT data is observed as pile of x-rays and this data is processed through commercial or open source software's to get final 3D models. Where additional alterations or adjustments are required, it can be made to the 3D CAD model. The CAD engineers are alter the 3D CAD model to a patient specific implant based on the anatomical structure of the patient. The 3D CAD model is converted to STL file and this STL file is used as input to the 3D printing machine. Finally, the 3D printing machine is used to manufacture the required 3D model. Subsequently, the post processing is required to get the final product. The post processing contains surface finishing and support removal etc. The last advance in the work process is the medical application. The complete procedure as shown in Figure 1.9.

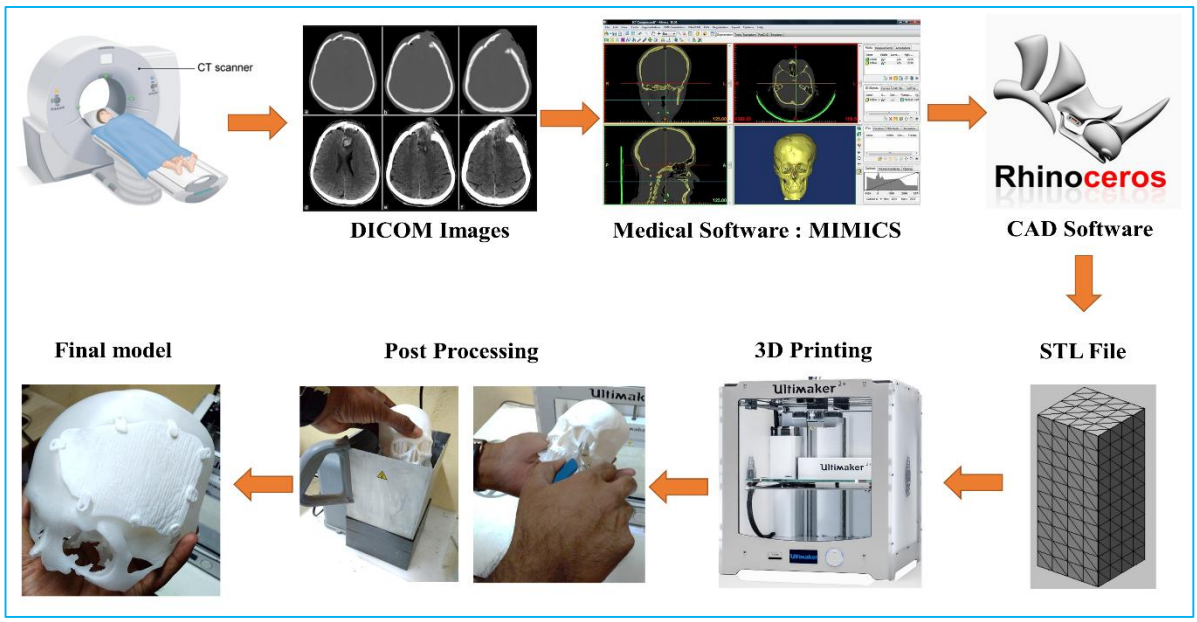

Figure 1.9 Procedure to manufacture medical models

The medical imaging techniques, with the help of Computer Aided Design and Manufacturing technologies (CAD/CAM) offers new possibilities for fabrication of customized cranial implants.

The 3D printing is creating major role in innumerable applications as functional prototypes, in the direction of biomedical applications, the 3D printed components are directly using as patient specific cranial implants, mandible implants and dental implants.

The advantages of 3D printing

1. Restoration of cranial implant for the patients to fulfil aesthetically, which impact on patient confidence level.
2. The prototypes are printed through this technology, which can creating major role in surgery time. Moreover, the prototypes help to plan the surgery, decreases surgery time at a rate of 85%, and the possibility of errors are overwhelmed while performing surgery.
3. The modifications in the implant are overwhelmed though preplanning of surgery and asses the perfect implant shape with respect to injured portion of the skull. The bio models are effectively communicate between patients and surgeons and assistance to elucidate the patient problem clearly corresponding families.

1.7 Cranioplasty

Cranial implants have experienced a significant evolution in the last decade in different aspects such as the type of materials and method of manufacture. Besides, the patient-specific cranial implants have been recently developed. Cranioplasty deals with the treatment of skull injuries and defects with established surgical procedures [13], [14]. The cranioplasty is a neurosurgical procedure to protect and cover the injured portion of the skull [15]. This surgical procedure is carried out to protect and restore the appearance of the skull shape and improve the psychological stability of the patient. The success of reconstructive skull surgery depends upon the preoperative evaluation of the cranial defect and additionally added with computer-aided design and 3D printing technologies [16] are used to know the osteotomy of implant with the host bone. The main aim of these procedures is to restore the protective function of the brain and cranial aesthetics. Due to these surgical procedures, the surgical time is drastically decreased at a rate of 85% and appearance of the patient was restored and allow him to perform daily activates safely. To date various materials have been used for the treatment of cranial defects such as titanium alloy (Ti6Al4V), polyether ether ketone (PEEK) and polymethyl methacrylate (PMMA) [17]. However, these

materials are biocompatible, successfully implanted for the skull and femur bone injuries. The ideal cranioplasty materials must have the fallowing features

- The cranial implant must fit to the host bone and achieve complete closure
- Endure at intracranial pressure (ICP)
- Easley mouldable
- Less expensive
- Ready to use
- It should non-infective and non-inflammatory
- The material is radiolucent
- Still, there is no perfect material is available to meet above conditions.

1.8 Implant materials

1.8.1 Polymethyl methacrylate

The polymethyl methacrylate gaining interest towards replacing the bone implants [18] because this acrylate is much stronger than bone technically speaking the strength of the acrylate is more than bone [15], [19]. This polymethyl methacrylate was discovered in 1939 year and done the experiments extensively in the year 1940 [20]. From these experiments to know that the mechanical properties such as compressive strength and stress resistance are high compared with hydroxyapatite as shown in Figure 1.10. In addition, the acrylate is successfully cleared in vivo tests. This material is biologically reacted with the tissue and absences of adverse effect on tissue

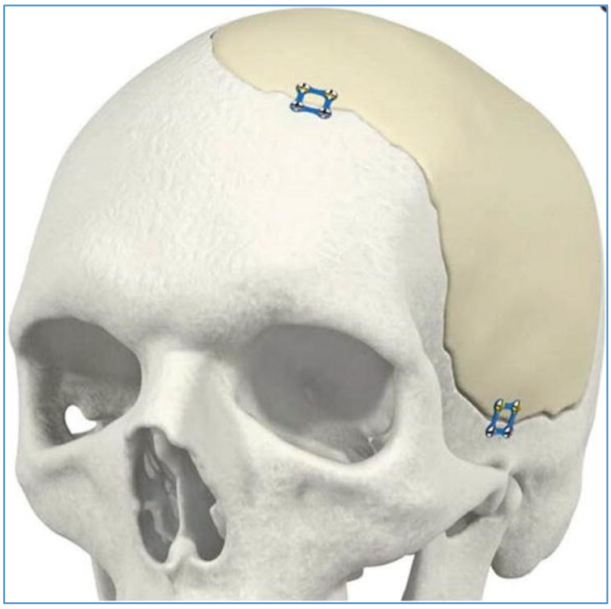

Figure 1.10 PMMA cranial implant [36]

such as necrosis etc. Moreover these results are considered that the acrylate is biocompatible as well as more strength than hydroxyapatite.

The numerous experiments were carried on the acrylate, it is observed that the acrylate is replace the metal because high heat resistant and radiolucent. While considering the radiolucent the acrylate showed the results diplomatically in positive and negative directions.

In the cranioplasty, the long term usage of polymethyl methacrylate was exhibited adverse effects, in the span of 8 years the complication rate was 23% especially infection, the infection is creating a major role. In further experimental studies are conducted on polymethyl methacrylate (PMMA), the infection rate was identifies as 12.7% [21]. This PMMA is widely using due to excellent tensile strength, while consider fracture susceptibility it is difficult to use.

1.8.2 Hydroxyapatite

The contouring of metal and synthetic implants are difficult while replacing the natural skull shape. The metals implant are showing blemishes in the CT scanned data after implantation to overwhelm these problems hydroxyapatite was introduced. The hydroxyapatite is replacing the bone mineral about 70% by weight and it is naturally available mineral compound, this is divided in to two categories such as Chlorapatite and Fluorapatite. The hydroxyapatite ($Ca_{10}(PO_4)_6(OH)_2$) is extensively used to replace bone implants [15], however the hydroxyapatite is manufactured synthetically [22]. The hydroxyapatite is combined with titanium mesh implant which give effective mechanical results as shown in Figure 1.11. In contrast to polymethyl methacrylate, which does not allow the skull to expansion in lateral direction. The hydroxyapatite is smoothly contoured through casting process to get finest cosmetic products.

Figure 1.11 a) Implant of patient with macro-porous areas located between the fixing holes b) Intra-operative view of the implant [22]

While considering the biological compatibility and chemical reactions with the bone, the hydroxyapatite is showed little adverse reactions with tissue and chemically excellent bonding with the bone. In contrast to polymethyl methacrylate, the hydroxyapatite has low mechanical properties such as brittle in nature and low tensile strength and quite high infection rates. The in vivo tests are carried out on hydroxyapatite in direction of Osseo integration [23], especially in humans the hydroxyapatite is break down in to fragments over a duration of time, due to these reasons the Osseo integration is limited. While consider the large defects in cranioplasty, to replace with hydroxyapatite is quite challenging and maintain structural integrity is difficult when exposed to cerebrospinal fluid and blood.

1.8.3 Titanium mesh

In the cranioplasty, the titanium mesh [15] is use alone and this mesh is combined with synthetic materials such as hydroxyapatite which strengthen the implant [24]. In contrast with polymers,

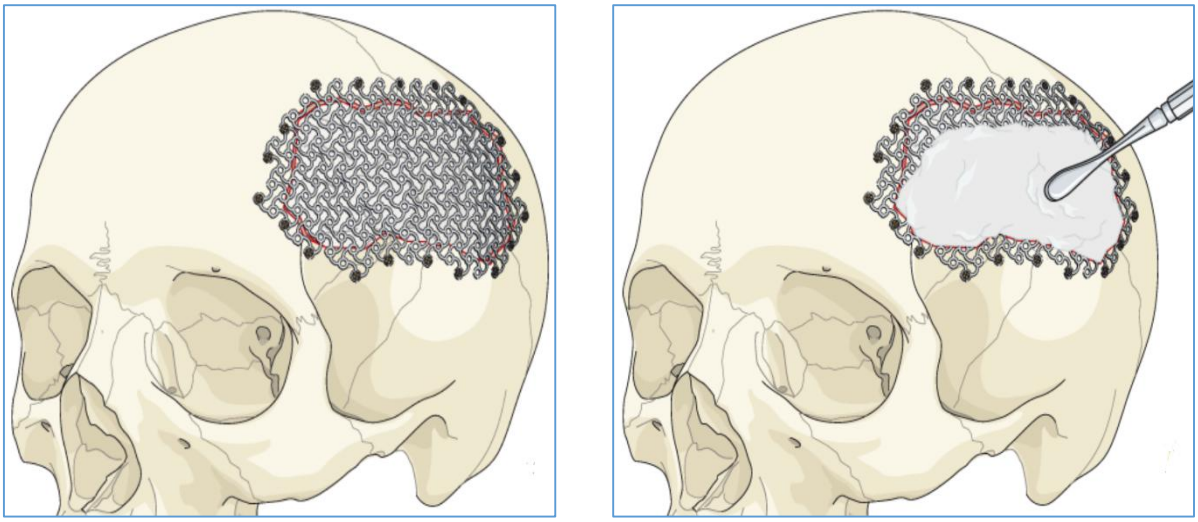

Figure 1.12 Titanium mesh implant fitted to the cranium model b) Filled with HA cement [25]

acrylates and hydroxyapatite the mechanical properties of the titanium is optimum. The titanium is a metallic alloy which exhibit high strength and malleability. Additionally, it is non-corrosive nature and non-inflammatory. Due to non-inflammatory, the infection rate is very low as 2.6% [21]. The titanium is categorized in to different alloys, among all alloys the Ti6Al4V grade 5 is predominant one to replace bone implants as shown in Figure 1.12 [25].

The use of titanium mesh in cranioplasty to decrease the rate of risk and increase the patient's life. In addition, the computer aided modelling is used to design the customized cranial implants and provide best aesthetical results even with large sized cranial defects.

1.8.4 PEEK implants

The polyether ether ketone (PEEK) is frequently used polymer to use as cranial implant with the help of 3D printing technology and computer aided modelling [26]. This PEEK is semi crystalline in nature, chemically stable material, and it is radiolucent. This can sterilized through gamma irradiation or steam. The PEEK had extensive mechanical properties such as high strength and more elastic compared with bone, due to elasticity the PEEK implant can merged properly in skull defect site with the use of miniplates as shown in Figure 1.13 [27].

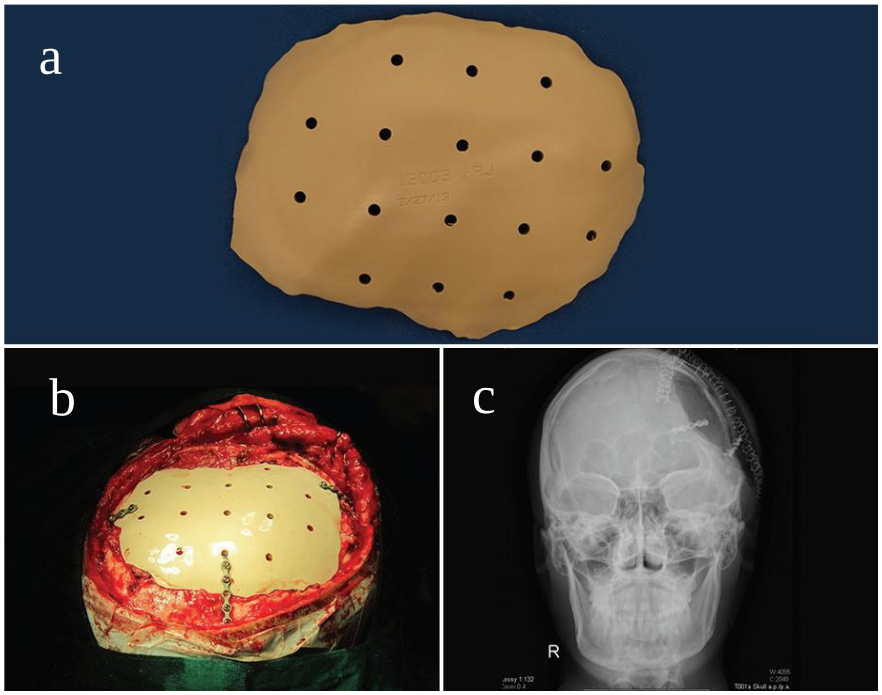

Figure 1.13 a) Machined polyether ether ketone implant b) Intraoperative fixation to the cranium c) Postoperative X-ray imaging [27]

The PEEK implant does not create blemishes while doing CT scan because it is non-reflective material. Due to less density, it is lighter in weight and handle comfortably while doing surgery. In addition to that, the thermal conductivity is low when compared to metallic materials [5]. Moreover, the PEEK had disadvantages such as little expensive and infection rate is quite high. The PEEK implant is not properly incorporate with the adjacent host bone, while removing the implant it causes high risk to the patient.

1.9 Organization of thesis

Chapter-1: Introduction

A brief background of the work has been reported in this chapter and insight to the anatomy of the skull, cranial bones, types of skull fractures, and different cranial implant materials, which was

successfully implanted. The microscopic level of the femur and cranial bone are explained with detailed information along with the types of skull fractures are discussed. These skull fractures are repaired with cranioplasty surgical technique, which is discussed in this chapter. Finally, the successfully implanted materials are explained.

Chapter-2: Literature review

The literature makes an attempt to give detailed information related to image data conversion, classification and complexity of defects, micro-CT data of cranial bones, various types of scaffold structures, intracranial pressure and CSF leak, and FEM and meshless approaches. Based on this entire literature survey, research gaps are identified and objectives are formulated. The work plan of the research is presented at the end of this chapter.

Chapter-3: 3D printed, customized cranial implant for surgical planning

This chapter discusses how to model the cranial implant through mirroring technique. This technique is used to model the cranial implant for symmetrical defects. This modelling is completely done through commercial software such as mimics and 3-matic. Finally, the implant is modelled successfully through the 3D printed machine and checked the fitting.

Chapter-4: Modelling and analysis of cranial implant: beyond mid-line deformities

This chapter discusses a novel modelling technique, which is a computer-aided reconstructive method. This study explores modelling and finite element study of the solid implant under Intracranial pressure (ICP) conditions. The implant fixation points allow implant behaviour with respect to intracranial pressure conditions. Consequently, the mechanical deformation and equivalent stress (von-Mises) are calculated with distinctive material properties such as titanium alloy (Ti6Al4V), polymethyl methacrylate (PMMA) and polyether-ether-ketone (PEEK).

Chapter-5: Design and analysis of various homogeneous interconnected scaffold structures for trabecular bone

This chapter discusses scaffolds structures, which provide temporary and permanent structural support for cell attachment and tissue regeneration. In this work, homogeneous interconnected scaffold structures were modelled by varying pore-size, porosity, strut cross-section and keeping the same unit cell size. The studies are carried out to find the impact of the design parameters such

as porosity, strut cross-section and size on the scaffold functional factor like permeability. The permeability of scaffold is studied through CFD analysis and it is calculated theoretically using Darcy's equation for incompressible laminar flow equation.

Chapter-6: Homogenous scaffold based cranial implant modelling and analysis – unit cell algorithm – meshless approach

This chapter explores a unique modelling approach of the cranial implant, homogenous scaffold algorithm, and a meshless method respectively. This modelling methodology is the easiest one and addressing both the symmetrical and asymmetrical defects. The implant is embedded in a unit cell based porous structure with the help of an algorithm, and this algorithm is simple to manage the consistency in porosity and pore size of the scaffold. Totally, six types of implants are modelled with variation in porosity and replicate the original cranial bone. Among six implants, Type 2 (porosity 82.62%) and Type 5 (porosity 45.73%) implants are analysed with the meshless approach under ICP. The total deformation and equivalent stress (von-Mises stress) of porous implants are compared with the solid implant under same ICP conditions.

Chapter-7: Conclusions and future scope

This chapter discusses various types of implant behaviours with respect to intracranial pressure and how much percentage difference in results i.e. the total deformation and equivalent stress. All the limitations encountered during the conduct of research and possible extensions to the present work are given in the form of future scope

Bibliography

The published research work reported by earlier authors in the related area in the form of journal papers, conference papers, textbooks and online sources, which are referred in this thesis and listed.

Appendix

This appendix discussed about conversion of STL file in Ansys software for simulation, benchmark analysis report for FEM vs meshless method, and convergence results are given**.**

CHAPTER 2
2. LITERATURE REVIEW

2.1 Studies on image data conversion and CAD

Hieu et al. 2003 and Gopakumar et al. 2004 explained about most of the customized cranial implants are fabricated based on patient specific data [12], [28]. Larysz et al. 2012 discussed that the patient specific data is in Digital Imaging and Communications in Medicine (DICOM) format obtained from Computed Tomography (CT) and Magnetic Resonance (MRI). A typical spatial resolution in microns with less slice thickness is required to get better solid model for hard tissues Presented by Jardini et al. 2014. This acquired image data sets are processed and subsequently converted into Standard Tessellation Language (STL) file formats that are required for 3D printing.

O'Reilly et al. 2015 and Bonda et al. 2015 worked on medical imaging techniques, Computer Aided Design and Manufacturing techniques (CAD/CAM) offers [29] new possibilities in fabrication of patient specific implants with 3D printing technology [30], [36].

2.2 Studies related to classification of skull defects

Hieu et al. 2003 and Gopakumar 2004. Chrzan et al. 2012. Jardini et al. 2014 have explained about anatomically the skull is the symmetrical part for many humans. The skull injuries are categorized into symmetrical and asymmetrical defects. In symmetrical defect, the malformation portion can be planned with contralateral side of the skull through computer aided modelling software [32]. Modelling of an implant for asymmetrical defects is quite challenging because mirroring of contralateral side of the skull cannot be possible and these defects deals with multi-point deformities and beyond midline deformities.

2.3 Studies related to complexity and classification of skull defects

Poukens et al. 2008, Williams et al. 2015 and Sahoo et al. 2017 are discussed about, **t**he skull defects leads to create an aesthetic and functional disturbances to the patient and these defects majorly classified according to their anatomical locations and degree of difficulty [33], [34], [35],. For clinical and scientific purpose, the implant ought to design properly and manufacture through 3D printing technology. In the process of designing, the complexity of implant is creating major role which involved with area of injured portion, injury is crosses the mid-line, orbital involvement, and frontal bone damage. These are more complicated defects compared with parietal bone defects

because the parietal bone easily replace through mirroring technique. The classification of skull defects are mainly depends on the size of the injured portion and extent of the injury.

The complexity of reconstruction of skull implant is based on three major factors

1. Size of defect [31], [36].
2. The skull injury crosses the sagittal plane i.e. mid plane of the skull.
3. The cranial injury associated with orbital rim.

The size of the skull injuries are creating a major role while reconstructing or modelling the implant through CAD software. Whenever the size of the defect is increases simultaneously model the implant perfectly which mimic the curvature of the host bone. The defect size is < 5 cm^2 considered as small defect , it is almost flat surface whereas defect size is > 100 cm^2 considered as large defects [18], [22], [34] due to that it requires more curved implant.

Whenever the defect cross the mid-line of the skull creates more complexity while designing the implant. Additionally, this defect involved with orbital which increases the complexity. However, the orbital area is mirrored from the other side of the skull.

Table 2.1 Classification of cranial defects according to complexity and size of the defect [33]

Surface area (a)	a< 5 cm^2	a>5cm^2 & a< 100 cm^2	a>100 cm^2	a< 5 cm^2 and orbital association	a>5cm^2 & a< 100 cm^2 and orbital association	a>100 cm^2 and orbital association
Not crossing midline (sagittal plane)	I	II	III	IV	IV	V
Crossing midline (sagittal plane)	I	II	III	IV	IV	V

The cranial bone thickness varies along the skull. However, designing anatomical locations for cranial implant the thickness of the bone has taken into account. The anatomical locations are evidently important while doing surgery. The defects are classified into six distinct classes, based on degree of difficulty and orbital involvement as shown in Table 2.1 [33].

2.4 Cranial bone thickness data observation through micro-CT

The cranial bone is complex material and since it helps to recognize the mechanism of trauma, the knowledge of its mechanical behaviour can be decisive in treatment of head injuries. Marieb 2012 and Martin 2012, the skull contains cranial and facial bones [1], [37]. The cranium surrounds and protects the brain. It consists of the occipital, parietal, frontal, temporal, etc. Among these parietal,

frontal and occipital are flat bones. A flat bone replicates a reinforced sandwich structure. However, this flat bone having thick layers of compact bone are called the internal and external tables or cortical bones. The spongy bone between the tables is known as the dipole. The top and bottom layers are high-density in nature and central trabecular layer comprises of low-density bone tissue due to numerous pores distributed through the material without any significant pattern. This low density bone is called as spongy bone or trabecular bone and the open spaces are filled with red or yellow bone marrow.

Thickness of the diploe is a crucial factor that affects the overall strength of bone and its thickness is vary along the skull. There is no significant correlation between porosity percent and overall mechanical properties. On the other hand, both elastic modulus and maximum bending stress increase with increasing percent of bone volume by Motherway et al. 2009 [38]. The outer layers represent the stiff part of the cranial bone while the lightweight core layer is an efficient energy absorber which makes the whole structure is durable.

Boruah et al. 2013 observed the skull in micro CT and a total of 84 skull core specimens harvested from 10 adult male [39]. The specimen cores were imaged prior to testing using a scanco vivaCT40 scanner (SCANCO Medical AG, Brüttisellen, Switzerland) with an isotropic resolution of 30 μm. A special core holder was used to hold the cores for μCT as shown in the Figure 2.1 [40]. The cores were submerged in saline solution inside a radio-transparent plastic tube (Figure 2.1) during imaging. Image slice direction is shown by the dotted red line. The image resolution allows identification of cortical and trabecular regions on the basis of discernible 3D structure as shown in Figure 2.1. Thickness of the three layers of the cores were measured by observing the onset of trabecular pores at four fixed 15 × 15 pixel windows on the slice image.

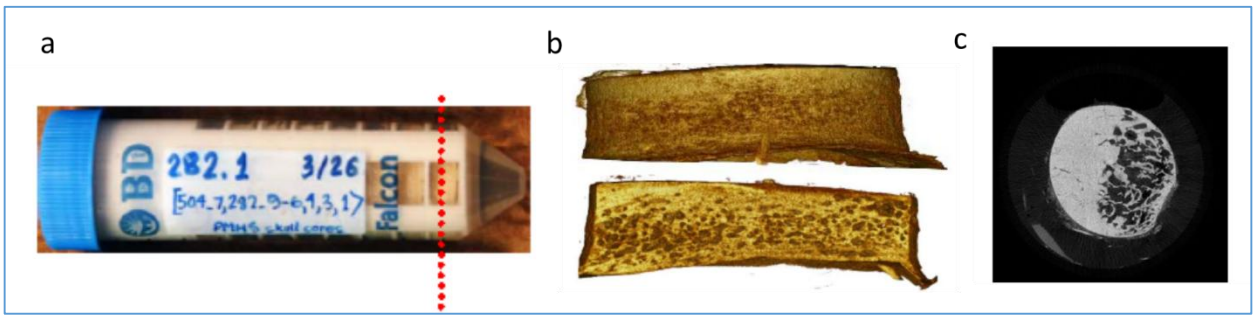

Figure 2.1 a) Custom core holding for μCT imaging, the dotted line indicates slice direction b) The 3D reconstruction of skull core c) The μCT Image sample of cortical bone [40]

The following geometric properties of the adult human cranium have been obtained as shown in Table 2.2 micro-CT data of cranial bones

1. The outer cortical layer is significantly thicker than inner cortical layer, the outer cortical layer is 0.76 mm and inner cortical layer is 0.35 mm.
2. The trabecular layer varied along the cranial bone is 5.08 ± 2.01 mm thick.
3. The compressive Elastic Modulus of through-the-thickness skull specimen is 450 ± 135 MPa.

Table 2.2 Micro-CT data of cranial bones [40]

micro-CT study results		
	Thickness [mm]	Porosity
Outer Table	0.76 ± 0.29	0.023 ± 0.017
Inner Table	0.35 ± 0.15	0.071 ± 0.032
Trabeculae	5.08 ± 2.01	0.399 ± 0.194

Suguru et al 2015 studied the mechanical properties and thickness of cranial bones such as parietal and frontal bones. Totally he collected 114 cadaver bones of Japanese among that 78 male and 36 are female cadavers [40]. From each cranium 8 samples were collected, two samples from frontal region, left and right parietal region and at sagittal suture which is near to the junction three sutures

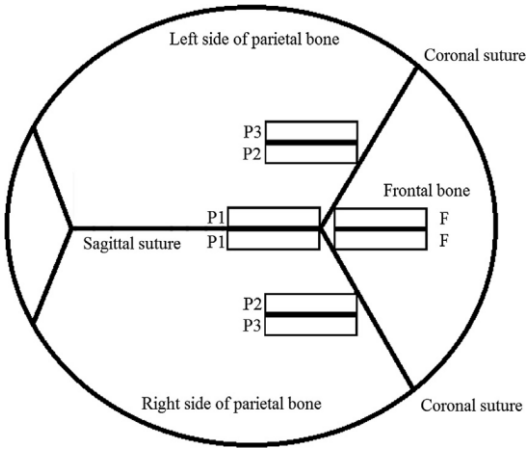

Figure 2.2 Total eight samples were collected, two samples from frontal region, left and right parietal region and at sagittal suture [41]

as shown in the Figure 2.2 [41]. Totally 912 samples were prepared, each sample was scanned in 16-row detector computed tomography system and measured the sample thickness (ST, mm) at the centre of sample. The CT was done with a slice thickness of 0.63 mm.

The thicknesses of frontal bone (F) is 7.3±1.7 mm for male and 7.2±1.7 mm for female, parietal bone (P) is 6.0±1.6 mm for male and 6.3±1.8 mm for female, left and right parietal samples (P1) is 6.7±1.7 mm for male and 6.5±1.8 mm for female, left superolateral parietal sample (P2) is 5.8±1.7 mm for male and 6.3±1.7 mm for female and left inferolateral parietal samples (P3) is 5.4±1.8 mm for male and 6.2±1.8 mm for female.

Julie et al 2009 studied the skull mechanical properties and thicknesses can provide insight to prevent the linear and depressed skull fractures associated with traumatic brain injury [41]. This complete study was used to design and develop the safety helmets which prevent the TBI. Totally 8 fresh-frozen cranial cadavers were collected among that 4 male and 4 are female cadavers at an age of 81±11 years old. From each cranium 26 samples were collected from right parietal region, 20 samples from right parietal region and 14 samples from frontal region as shown in the Figure 2.3 [42]. Totally 63 samples were prepared, each sample was scanned in micro computed tomography system at a resolution of 56.9 μm and measured the sample thickness. Finally, the average sample thickness of sample is 6.46±1.06 mm.

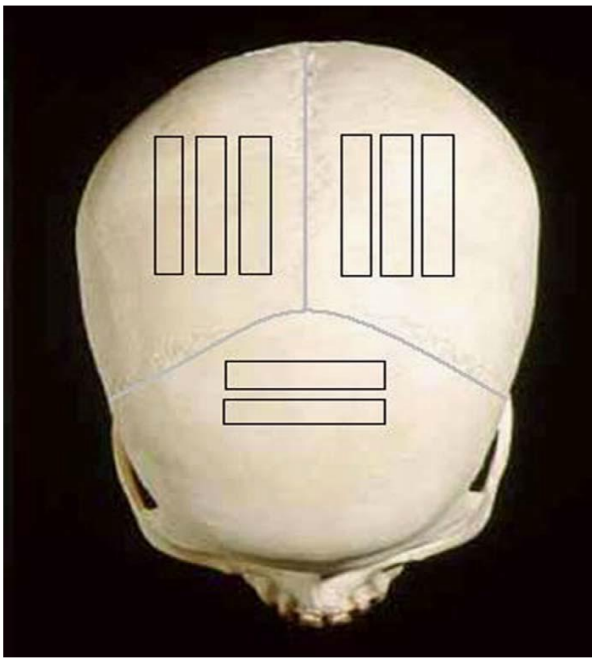

Figure 2.3 Totally 8 fresh-frozen cranial cadavers were collected among that 4 male and 4 are female cadavers [42]

Audrey et al 2014. Studied the macroscopic thickness, apparent density and an apparent elastic modulus on a large number of human fresh cranial bone samples. Totally he collected 21 human skulls [42]. From each cranium around 18 samples were collected which are from frontal region,

left and right parietal region, right and left temporal regions and suture as shown in the Figure 2.4 [43]. Totally 351 samples were prepared, each sample was 60 mm length and 13 mm width. Finally, he found that the average thickness of frontal bone is 7.0±1.1 mm, 6.5µ±1.3 mm for parietal bone and 4.7±1.0 mm for temporal regions. The average apparent densities of frontal, parietal and temporal are 1710±127 kg/m^3, 1684±124 kg/m^3 and 1782±121 kg/m^3.

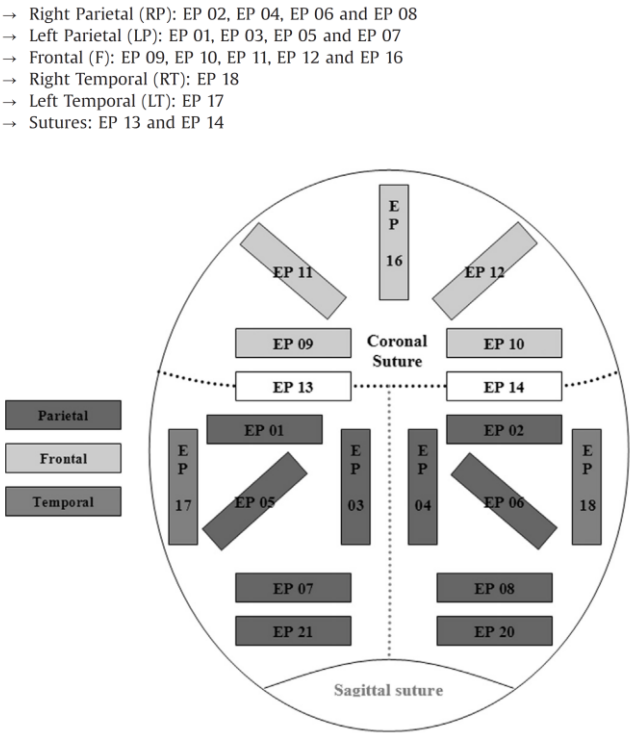

Figure 2.4 Total 18 samples collected from frontal region, left and right parietal region, right and left temporal regions and at suture [43]

2.5 Bone tissue scaffolds and modelling methods

The autograft, allograft and xenograft techniques are commonly used to replace human organs such as liver, kidney and bones. These are limitedly available for harvested site, the main disadvantage is immune rejection, host tissue necrosis and disease transmission. These disadvantages are overcome through synthetic biological substitute using concept of tissue engineering [43], which can effectively mimic functions of tissue characteristics.

Scaffold can be extricated from characteristic assets, for example, coral and animal bone or can be manufacture utilizing polymer processing techniques, for example, freeze drying, solvent casting, salt leaching and these procedures are leads to absence of uniform pore appropriation and mechanical strength. To overcome these drawbacks, the 3D printing technologies are utilized as a

part of the creation to control the scaffold properties such as pore size and strut diameter. The 3D printing approaches to utilize three-dimensional computerized geometry to manufacture the scaffold. Therefore, the scaffold properties would then be able to be predefined utilizing the computer aided design (CAD) software. In light of this strategy, the properties of scaffold can be effectively characterized and controlled, if the primitive geometry is connected. Based on these techniques, the authors are planned to design tissue scaffold. Furthermore, today computer aided design/manufacturing (CAD/CAM) and 3D printing have gotten much consideration in scaffold manufacture and these innovations meet the greater part of the scaffold design prerequisites.

2.5.1 Modelling of scaffold

2.5.1.1 CAD-based methods

The CAD based tools such as CATIA, Creo, SolidWorks, Rhinoceros, MIMICS and 3-Matic are commercially available software's to design three dimensional structures as shown in Figure 2.5. The CAD is mainly depends on two systems such as CSG (constructive solid geometry) and B-Rep (boundary representation) [44].

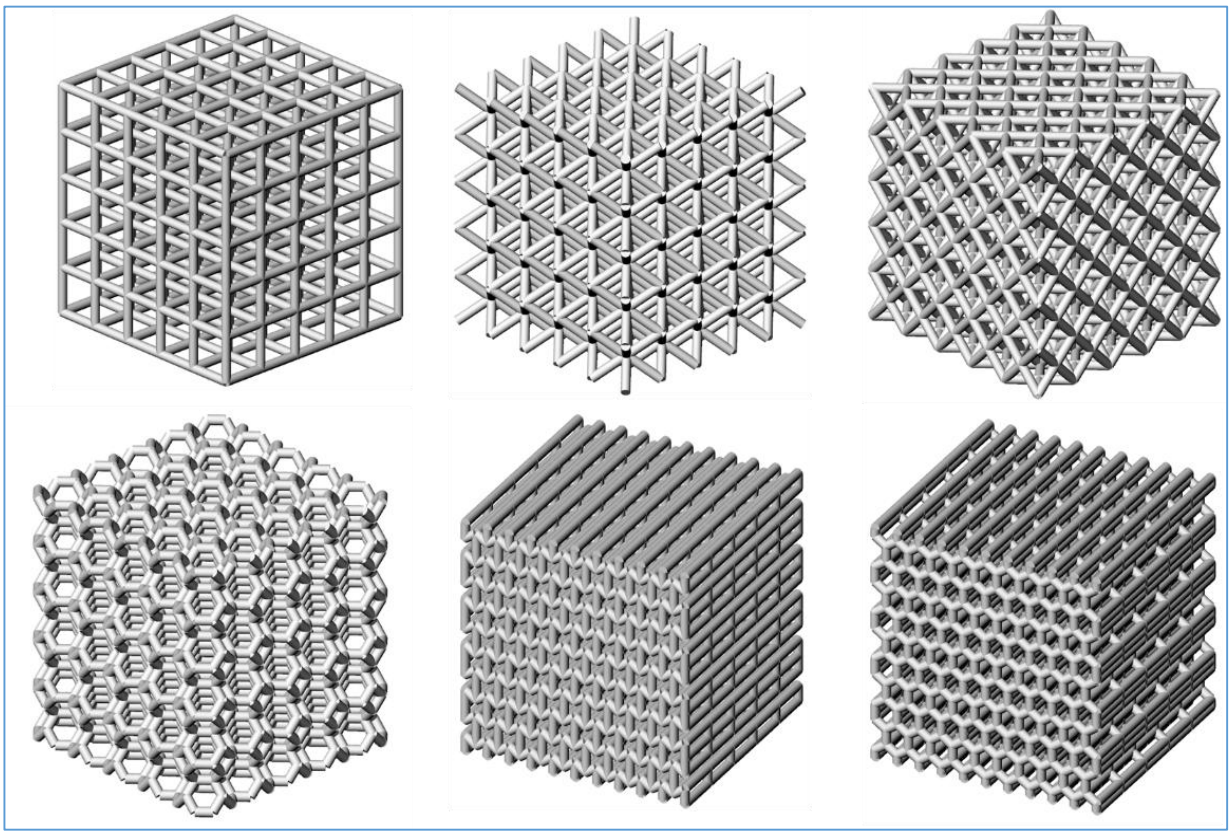

Figure 2.5 The unit cell based scaffold structures

The constructive solid geometry is step by step procedure to represent the solid model, the final solid model is developed through the combination of Geometrical primitives (such as cube, cylinder and sphere) and Boolean operations (such as addition, subtraction and intersection). However, the constructive solid geometry is limited in design capability. The boundary representation is to represent the solid through vertices, edges and loops. These vertices, edges and loops are used to find the boundary gaps and overlaps in solid model.

2.5.1.2 Implicit surfaces

The modelling and generation of cellular lattice structures are conceivably complex surface structure, these cellular structures are modelling through "Implicit surface modelling" (ISM).

This ISM is an exceedingly adaptable approach and permits platform to model scaffold architectures effortlessly using mathematical equations. These mathematical equations are used to control architecture and porosity of the scaffold effectively. Recently, the design of biomorphic cellular structures are developed through ISM. The implicit functions are using to mimic structure of insect shells and butterfly wings. The most common Implicit surfaces are P-type (Schwatz's Primitive). G type (Schoen's Gyroid) and D-type (Schwarz's Diamond) as shown in Table 2.3.

Table 2.3 Various implicit-surface-based scaffold structures [44]

Scaffold type	Mathematical function	CAD Model
Diamond	D:sin(x)·sin(y)·sin(z)+sin(x)·cos(y)·cos(z)+cos(x)·sin(y)·cos(z)+cos(x)·cos(y)·sin(z)=0	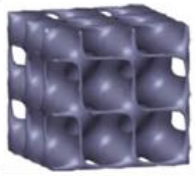
Gyroid	G:cos(x)·sin(y)+cos(y)·sin(z)+cos(z)·sin(x)=0	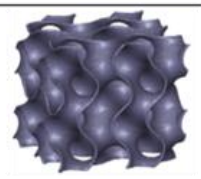
Gyroid, high porosity	GHP: cos(x)·sin(y)+cos(y)·sin(z)+cos(z)·sin(x)-k=0	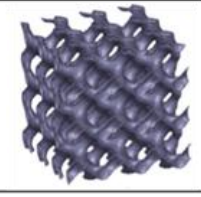
Gyroid, gradient architecture	GGA: cos(x)·sin(y)+cos(y)·sin(z)+cos(z)·sin(x)-k'z-k''=0	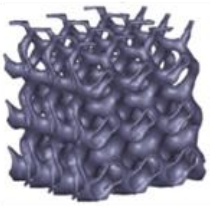

In a contemporary, the impact of pore shape on cell seeding viability and static culture result has been experimentally studied the results by considering a gyroid architecture (manufactured by SLA) with an irregular pores [44].

2.5.1.3 Space-filling curves

The fused deposition method is used to manufacture scaffold through extrusion based process. In this method flexibility to change fibre diameter range from 0.25 to 0.4 mm, line spacing in micron level, layer thickness is 0.1 to 0.4 mm and stacking direction 0 to 180 degrees. These controlled parameters are help to control porosity and pore size of the scaffold which effects the mechanical properties such as compressive strength and energy absorption etc. The scaffold observed in this method is lay-down patterns, these lay-down patterns can be controlled through stacking direction and layer thickness, which helps to model Honeycomb and Hilbert curve patterns as shown in Figure 2.6 [44].

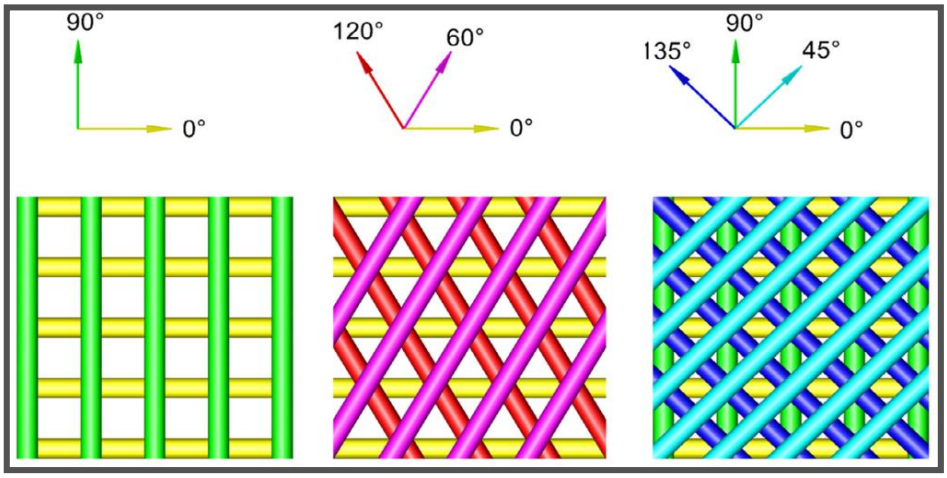

Figure 2.6 Lay-down patterns with honeycomb pores [46]

2.6 Scaffold parameters

Tissue engineering is a multidiscipline research area which applies engineering and biological sciences to develop the biological substitutes known as “scaffold”. Which restore, maintain, or improve tissue functions. These scaffolds are required to meet the preliminary criterions to encourage cell attachment, tissue growth and meet the mechanical strength. The basic need of the scaffold is permeable. However, the permeability or vascularity is depends up on scaffold parameters such as porosity and pore size. These are mutually dependent parameters, the pore size increases significantly the porosity of the scaffold is increases. The below structural parameter are influencing the bone scaffolds to integrate with the host bone for tissue regeneration. The brief discussion as fallows

2.6.1 Porosity

The tissue regeneration is predominantly depends on porosity of the scaffold. The porosity is increases respectively the open space or void volume is increases in the scaffold, this space is support to growth of new tissue, promote the blood vessels and associated with minimum amount of foreign material present in the human body. According to these, the porosity of the scaffold is maintained preferably as high as possible. The porosity defines the relationship between the volume of scaffold and the apparent volume (Bounding volume of the scaffold).

2.6.2 Pore interconnectivity

It defines the interconnectivity between the pores in scaffold, such as open or closed pores. The open pores are prominent type, which enhances tissue growth, diffusion of nutrients, oxygen and waste products. These open pores are promote ingrowth of blood vessels.

2.6.3 Specific surface area

This is specific surface area [45] is essential and key factor for cell attachment, it represent the surface per unit of the apparent volume of the scaffold. A higher the surface area of the scaffold correspondingly the higher the cell attachment and effective in osteoblast proliferation. It is the ratio of interface surface area to the apparent volume of the scaffold and unit are mm^2/mm^3.

2.6.4 Pore size distribution

The scaffold pore size is significant effect on cell seeding and tissue generation. The pore size estimate is for the most part fluctuates in view of use, for example, soft tissue scaffold and hard tissue scaffolds. The satisfactory pore size is 100 µm for osteoconduction. Higher the pore size estimate individually the porosity increment and mechanical quality will diminish. Consequently the desired scope of the pore size in the bone scaffold was favoured between 100 µm to 800 µm for bone.

2.6.5 Permeability of scaffold

Permeability is ability to transmit or transfer the fluid through its pores with respect to pressure difference, the pore size is creating important role on permeability. The permeability of scaffold is enhances the transportation of nutrients and oxygen, which is beneficial for cell attachment with scaffold and cell proliferation. The permeability of healthy cancellous bone lies $10 - 100*10^{-10}$ m^2. The permeability of scaffold is examined through computational fluid dynamics (CFD), the main

goal of this examination is to utilize CFD approach and quantify the cancellous bone permeability. The boundary conditions can be appointed to the model and imitate Darcy's law (Darcy 1856) [46].

Table 2.4 Permeability of various scaffolds with various pore sizes

Authors	Materials	Pore size (avg. µm)	Porosity (%)	Permeability (m^2)
Li et al. (2003) [47]	Z-BCP (Biphasic calcium Phosphate) D-BCP I-BCP HA-60 HA-50 (Hydroxyapatite)	565 300 528 450 250	75 78 60 60 50	0.018×10^{-9} 0.10×10^{-9} 0.35×10^{-9} 0.37×10^{-9} 0.075×10^{-9}
Lee et al. (2006) [48]	PPF: Poly(propylene fumarate)	300 600 900	21-26 38-50 51-65	0.02×10^{-9}-0.09×10^{-9} 0.55×10^{-9}-1.50×10^{-9} 1.50×10^{-9}-2.3×10^{-9}
Sanz-herrera et al. (2009) [49]	Bio glass-based foams	510–720	90-95	1.96×10^{-9}
Jeong et al. (2011) [50]	POC : poly(1,8-octanediol–co-citrate)	900 900	50 60	0.351×10^{-8} 4.74×10^{-8}
Truscello et al. (2012) [51]	Ti alloy (Ti6Al4V)	-	56.7	$0.52\times10^{-9} \pm 3.9\times10^{-12}$

Recently computation fluid dynamics was introduced to find the permeability of trabecular bone specimen, the CFD is helps to calculate the flow characteristics along the length of specimen. The CFD helps to eliminate the bench-top testing equipment to know the permeability of specimen and it helps to observe the behaviour of fluid at particular location in specimen [52].

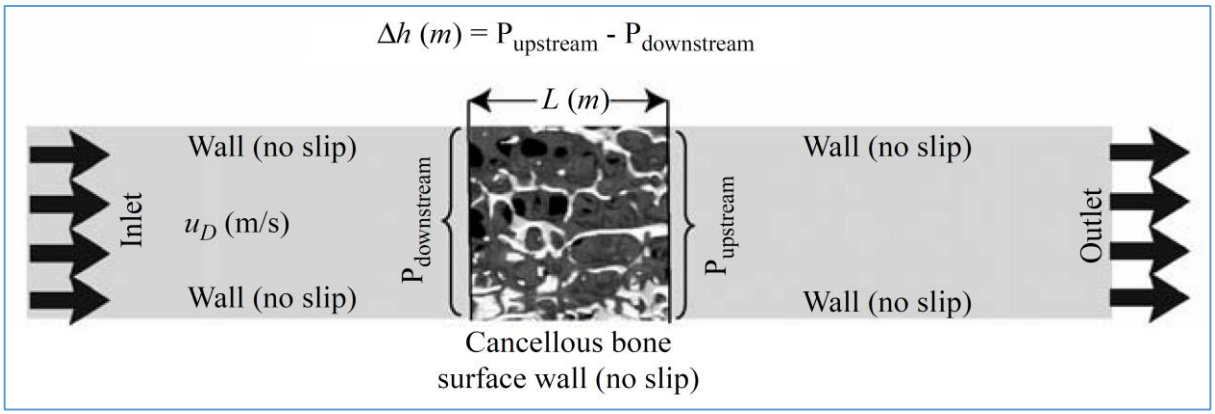

Figure 2.7 Permeability CFD setup [53]

Jeremy et al. 2012 developed a model with appropriate boundary conditions are assigned in CFD software to mimic the experimental setup and testing conditions, the trabecular bone is meshed with the tetrahedral elements convert to solid model [53]. The solid model was imported to Ansys CFX software and defined the boundary conditions as per Darcy's equation. The main boundary conditions are the inlet velocity of fluid i.e. water in m/s and assumed no-slip condition at boundary walls as shown in Figure 2.7 [53].

2.7 Scaffold design requirement

The scaffold architecture is plays major role in the rate and level of bone ingrowths. It is important to recollect that mechanical properties and mechanical strength of the scaffold throughout the healing process and the scaffold should equally encourage a fast and proficient healing process. The standard requirements of the scaffold as shown in Table 2.5 [44]. To accomplish these objectives the pore size must be sufficiently expensive to permit flow of free supplement i.e. nutrients and osteoblast transport yet sufficiently little to guarantee satisfactory mechanical properties as shown in Table 2.6 [44].

Table 2.5 Required Standards of ideal scaffold for bone tissue engineering [45]

Criteria	**Required standards**
Biocompatibility	Support stem cell attachment to scaffold, proliferation rate and differentiation, and initiate tissue regeneration both in vitro and in vivo
Osteoconductivity	Encourage host bone to regenerate in the scaffold
Biodegradability	Ability to degrade physiologically with defined rate
Mechanical properties	Scaffold should maintain sufficient mechanical strength to support tissue regeneration.
Porous structure	The scaffold should be porous which is greater than 90% depends on application and maintain the pore size 300 to 500 μm. These parameters helps to formation of new bone with proper vascularization.
Fabrication	Readily produced through various fabrication processes such as Additive manufacturing. The fabricated part is match to host bone of the patient.
Commercialization	Fabricated with an acceptable cost

Table 2.6 Required Design parameters for the scaffold [45]

Scaffold parameters	**Design requirement**
Porosity	Maximum without compromising mechanical properties significantly
Pore size	Range 300 μm – 500 μm
Pore structure	Scaffold pores should highly interconnected
Mechanical properties of the scaffold	
Cancellous bone	Tensile and compressive properties
	Strength: 5 – 10 MPa
	Elastic Modulus: 50 – 100 MPa
Cortical bone	Tension
	Tensile Strength: 80 –150 MPa Elastic Modulus: 17 – 20 GPa
	Compression
	Compressive Strength: 130 – 220 MPa
	Elastic Modulus: 17 – 20 GPa
Derivative properties	
Biocompatibility	No chronic inflammation

2.8 Successfully implanted materials for cranial implant

Advances in 3D Printing technologies have given extraordinary chances to manufacture complex structures.

The bone implants are replaced through Metals and alloys. Among them, the utilization of stainless steels, cobalt (Co) based alloys (CoCrMo), and titanium (Ti) and its alloys are recognized features such as biocompatibility and mechanical properties and non-corrosive and erosive protection in the human body [20]. The stress shielding is occurred due to dissimilarity in young's modulus of the material, the metal alloys young's modulus is greater than the bone which is inevitable

disappointment. The Ti6Al4V has young's modulus is around 110 GPa, cortical bone 3-30GPa and cancellous bone is 0.02 to 2 GPa. To overcome the stress shielding at bone-implant interface a strategic young's modulus is maintained as bulk material with proper porosity proposed by Gibson and Ashby Equation. However, in this work the Gibson and Ashby Equation is not used.

2.9 PMMA

Polymethyl methacrylate is often used material to restore and repairing cranial defects. It gained popularity during the World War II when it was used to treat cranial injures of soldiers [20]. The polymethyl methacrylate material is prepared conventionally by mixing a powder polymer with a liquid monomer form (methyl acrylate) and benzoyl peroxide that serves as an accelerator. The exothermic chemical reaction and polymerization occurs, this chemical reaction creating the final solid polymer, during preparation the mixture of polymerized methyl methacrylate and liquid monomer can be prepared at prescribed operating temperature [54]. Then the resulting material becomes malleable and can be shaped to fit the cranial defect. A sterility of powder used to mix this acrylic resin must be ensured, however, that seem to be a problem in the beginning of PMMA usage. As side effects, due to many studies, in some cases thermal damage of neural tissue and intoxication from residual methyl acrylate monomer during the material hardening appears. As a strong cytotoxic lipid solvent present in saline irrigation of PMMA implants, methyl methacrylate monomer can cause severe neural tissue damage during application. Among intoxication and nerve damage caused by heat, there have been cases reported allergic reaction related to application of PMMA implants as well. In comparison with majority of metals PMMA is lighter, cheaper, has better malleability, higher level of radiolucency and lack of thermal conduction. On the other hand, the problem with acrylic resins like PMMA is its brittleness and consequently risk of fracture of PMMA implants [55]. Therefore, titanium mesh is often used supporting the PMMA paste while doing implantation in the body. Pure PMMA has a Young's modulus between 1.8 and 3.1 GPa and a Poisson's ratio between 0.3 and 0.4. In the last decade, the improvement of computer-aided design and modelling decreased number of intraoperatively moulded PMMA implants and open a new era of PMMA usage in patient specific implants. Although, PMMA seems to be a suitable material for cranial implants, its poor Osseo integration properties [31]. Due to poor Osseo integration usage is limited. Therefore, a material with PMMA core was invented introducing a layer of porous fibre on a surface of PMMA coated with bioactive glass improving its level of biocompatibility. Despite slightly reduced mechanical properties this new type of PMMA based implants offer a new type of biological advantages including bone ingrowth.

2.10 PEEK

Polyether ether ketone (PEEK) and porous polyethylene are above of the most used plastics in clinical practice. The usage of polyethylene was limited to small cranial defects due to its softness until porous polyethylene was invented. The pores, 300–550 μm wide [22], not only improved mechanical properties of polyethylene but more importantly allowed ingrowth of soft tissue inside the pores and to deposit collagen as well.

PEEK is an organic thermoplastic polymer without any colour, commonly applied in engineering applications. It is very often used as a material for customized cranial implants but can also be shaped intraoperatively. PEEK, in terms of medical application [56], was originally used for spinal reconstruction, however, experiments have shown its great potential for cranioplasty usage as well [57], [58]. It is comparably strong, radiolucent and stiff as compact bone. PEEK has an elastic modulus of 3.6-4 GPa, and Poisson's ratio about 0.4. However, PEEK is semi crystalline thermoplastic and therefore its mechanical behaviour is highly influenced by its matrix properties that are defined according to processing conditions. PEEK is also chemically inactive, non-allergenic, and lighter than titanium and has the ability to withstand multiple high temperature. Whenever, the defect reconstruction fails due to non-destructive reasons such as infection then PEEK implants can be serialized and reused. The PEEK is a thermoplastic material able to remain stable up to 240°C and melts at a relatively high temperature of 343°C. To manufacture complexly shaped parts made of PEEK, Stereolithography is used [22], replacing conventional methods of PEEK processing such as injection molding or CNC. Nevertheless, the pure PEEK cranial implants are not biologically active, therefore at the end of manufacturing process, they must be coated by collagenous fibrous tissues to allow Osseo integration.

2.11 Titanium

The most common metallic biomaterial used in current practice as a material for cranial implants is a pure titanium or its alloys [59]. Titanium is biocompatible, has almost no risk of allergic reaction, great mechanical strength and low infection rates. Titanium is non-magnetic material with high corrosion resistant due to formation of surface coating layer of titanium oxide (TiO_2). It is also less expensive than some other metals and has a good level of radiolucency as well. Pure titanium occurs in two types of crystalline formation, alpha and beta. Alfa phase has a hexagonal close-packed crystalline structure (hcp) and is the form that occurs at room temperature. In contrast, beta phase of pure titanium is characterized by body-centred cubic crystalline structure

(bcc) and occurs at higher temperatures. Alloying elements tend to move phase transformation temperature upwards or downwards, stabilizing either the alpha or beta formation type. Based on this feature, there are alpha stabilizers (aluminium, tin, and zirconium) and beta stabilizers (vanadium, chromium, iron) creating three categories of titanium alloys: alpha alloys (α), beta alloys (β) and alpha-beta alloys (α+β). The most commonly used titanium alloy for cranial implants is Ti6Al4V. Ti6Al4V or also just Ti64 is part of the alpha-beta alloys group where aluminium stabilize alpha phase while vanadium stabilize beta phase. Very popular in practice is also Ti64 ELI, which stands for Ti6Al4V extra-low interstitial version with very low percent of impurities. Ti64 ELI has a Young's modulus of 110 GPa and Poisson ratio of 0.30. Due to its great properties titanium is also used alone as a titanium mesh or as a scaffold for cements. However, most of the times, titanium is used as a material for patient specific custom made implants using computer aided design and 3D printing technologies such as electron beam melting process [60].

2.12 Intracranial Pressure (ICP) with respect to body position and CSF leak

The term intracranial pressure is understood as a pressure inside cranial cavity. In a normal state, volume of cranial cavity, which is approximately 1700 ml and it is composed with three components such as brain tissue (80%), cerebrospinal fluid (10%) and blood (10%). Intracranial pressure depends on mutual interaction between these three components and cavity volume. The cranial cavity of and adult patient is relatively rigid structure, therefore intracranial pressure is determined by pressure of brain tissue, cerebrospinal fluid and blood on the cranial cavity wall. These three components, filling the cranial cavity space completely, are relatively incompressible due to high water content. Consequently, change of volume of one component leads to change in intracranial pressure. In reality, the volumes of all of these three components are unstable values and altering irregularly. As a result of this fact intracranial pressure is a dynamic value dependent on immediate values of volume of components involved. It also varies with age, body position ad clinical conditions. An adult human being, when lying down, has a neutral value of intracranial pressure between 7-15 mm of Hg (pressure value expressed by a height of mercury column) which corresponds to 0.9-2.0 kPa. When standing, the value can get below the level of atmospheric pressure which is 29.92 mm of Hg or 3.99 kPa. The ICP is varies with body position and age, it is normally between 7-15 mmHg in healthy adults. The ICP is showing negatively range is -10 to -15 mmHg in vertical position of the body and 1.5-6 mm of Hg for infants and 3-7 mm of Hg for

children's. This ICP is reaches 20-25 mm of Hg for TBI patients, a close observation in the intensive care unit and prominent surgical procedures are required.

Fundamentally, the cranium fontanelles and sutures are fused together which condensed the raised intracranial pressure (ICP). It states that 1) the brain fully encapsulated in the non-expandable cranial bone ii) mostly parenchyma of the brain is incompressible and the volume of blood is constant in the cranial cavity [2].

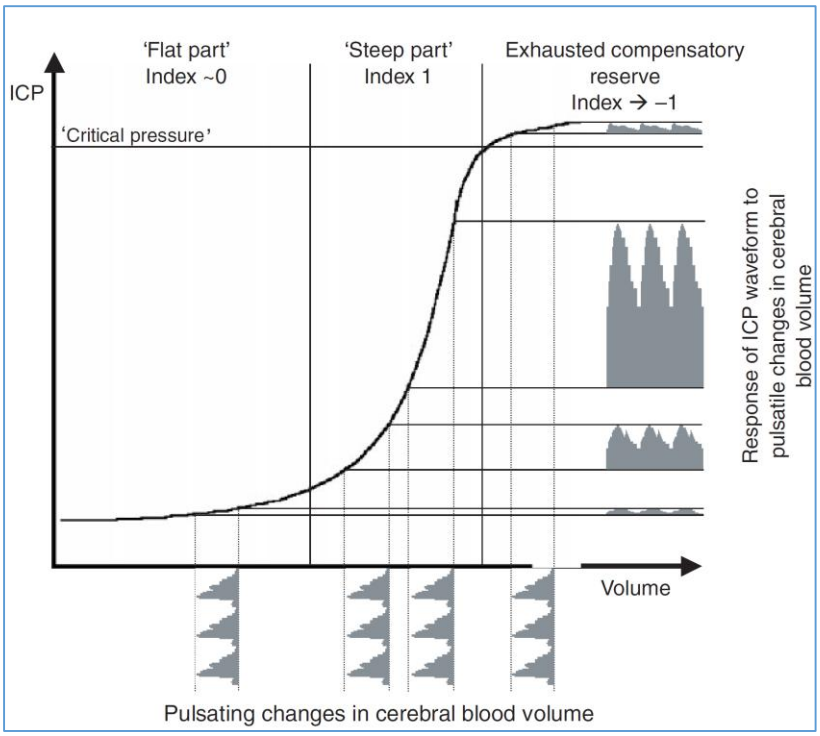

Figure 2.8 Monitoring of injured brain [2]

The ICP and intracranial volume relationship is described through non-linear curve between pressure and volume. The pressure-volume curve is divided in to three parts, in the first part the curve is flat which indicates lower intracerebral volume and ICP is remains low and micro level changes in the intracranial volume. These changes effect the reduction or increase in volume of CSF. However, this mechanism is disturbed consequently the pressure-volume curve is drastically increases. The drastic change is in second part as shown in Figure 2.8 [2]. This part represents increased ICP relatively small increase in intracerebral volume. Finally at third part, the curve is flat again which indicates cerebrovascular responses.

2.12.1 Symptomatic epidural fluid collection and CSF leak after cranioplasty

Se et al 2015 was investigated the risk factors which develop symptomatic epidural fluid collection (EFC) after cranioplasty following TBI as shown in the Figure 2.9 [61]. He observed the 82 patients who underwent decompressive cranioplasties. Among them 53 are male and 29 are female, the average age was 51.5±27.5 years. In this research most of the cranioplasties are autografts and these bone flaps were fixed through micro screws and miniplates. These bone flaps are stored at a temperature of -78 ^{o}C and a closed drainage system was maintained which is used to collect the fluid. He observed various factors which effect on EFC such as age, sex, cranioplasty and cerebrospinal fluid (CSF) leakage during cranioplasty and size of the bone flap or implant. The

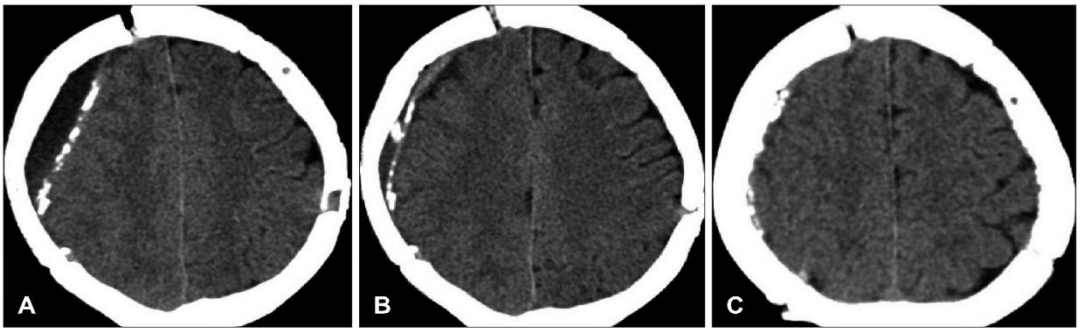

Figure 2.9 A 62 years old patient with epidural fluid collection A) CT scan of post-cranioplasty after 4 days B) Evacuation of EFC C) After 3 Months no recurrent fluid [61]

large size defect with cerebrospinal fluid leakage during cranioplasty is identified as the statistically significant risk factor. The CSF leakage is observed in 10 patients with symptomatic EFC and 2 patients with No symptomatic EFC due to this observation, however, careful attention is required to avoid CSF leakage during cranioplasty is needed to minimize the occurrence of EFC.

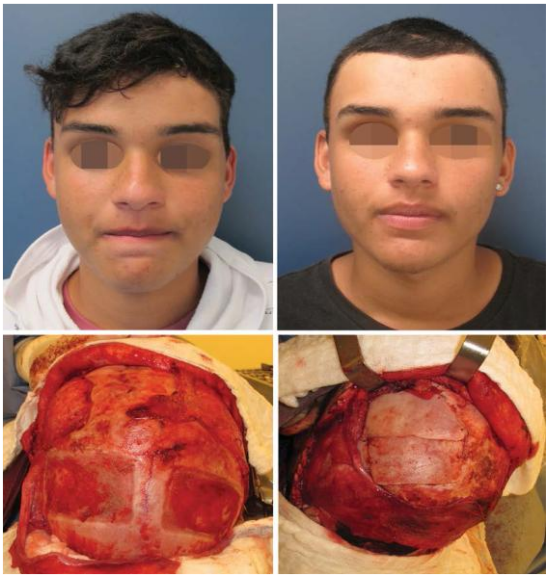

Figure 2.10 Patient with CSF leakage [62]

Pablo et al 2015 stated the various indications after carried out cranioplasty surgery such as recovery of patient against TBI, recovery of cranial contour surface and treat the SOT (syndrome of trephined) [62], [63]. He stated the report of 16 consecutive cases of cranial reconstruction among that he observed CSF leakage from the laceration of dura-mater as shown in the Figure 2.10 [62]. This was repaired using simple suture and pericranium patch; this patch is strengthened with haemostatic agents and biological glues or synthetic dura-mater. Due to SOT, the patient may get symptoms of dizziness, fatigue, vague discomfort at defect site, anxiety and intolerance to the vibration. These symptoms are not yet fully defined, however, these are related to changes in the movement of cerebrospinal fluid or atmospheric pressure which compress the cortex.

2.13 FEM and meshless approaches to analyse the implant

Skoworodko et al. 2008, Tsouknidas et al. 2011 and Dattatraya et al 2015 are extensively worked on FEA. An effective way of analysing implant design is by performing finite element (FE) based simulations [64], [65], [66]. This methodology can be employed to assess the deformation and equivalent stress in the implant with respect to variables in the design.

Tsouknidas et al. 2011 studied the mechanical behaviour of the cranial implant under sudden impact force caused by the tennis ball which causes to develop the stresses in implant. Additionally studied the behaviour of implant with gradual increase of force. The load initially applied at 100N and gradually increased up to 1780 N and impact of ball with a velocity of 30 m/s. Boundary conditions are load is evenly distributed over an area of 3 mm^2 and it is applied at centre of the

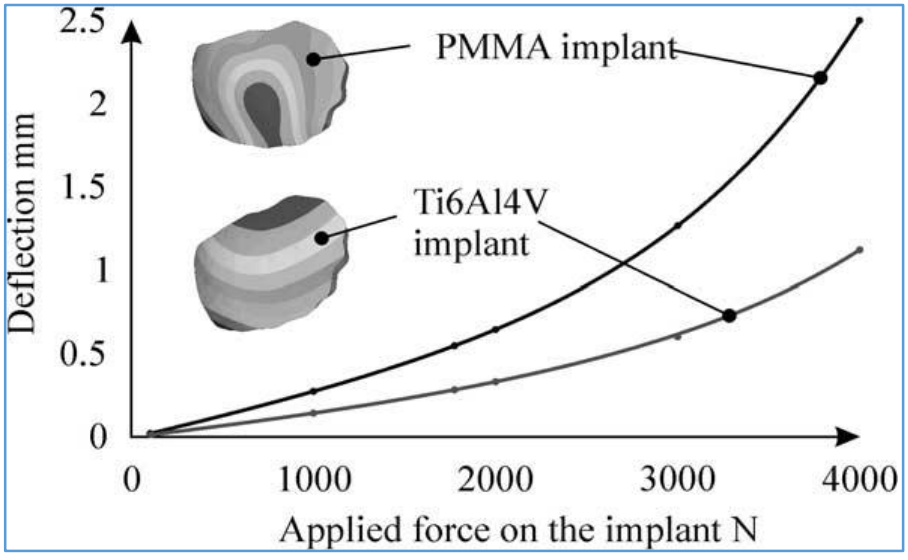

Figure 2.11 The deflection values of Ti6Al4V and PMMA implant [65]

implant. The contact was not defined between cranium and implant, except the fixation points and cranial bone.

The above mentioned boundary conditions and loading data is used to simulate the PMMA and Ti6Al4V implant. The PMMA cannot with stand at loading conditions while considering Ti6Al4V, the Ti6Al4V providing sufficient protection and withstand at higher loads in terms of absorbing higher energy and developing less stress values. Finally, the Ti6Al4V is showed significantly lower deformation over the PMMA implant as shown in Figure 2.11.

El Halabi et al. 2011 imported the STL file in Ansys 15.6 software and discretized with solid 185 elements i.e. 10 node tetrahedral element [67]. The boundary conditions are applied according to in situ condition after surgery, totally three type of boundary conditions are considered as shown in Figure 2.12

1) The implant is assigned with cortical bone properties such as young's modulus 18 GPa and poisons ratio 0.3. The contact region between skull and implant is defined as non-penetration type.
2) The second boundary condition is defined as fixed boundary condition (all DOF is arrested) on surface nodes of the skull.
3) The third boundary condition is defined as boundary nodes of the implant is constrained along normal direction of the skull surface.

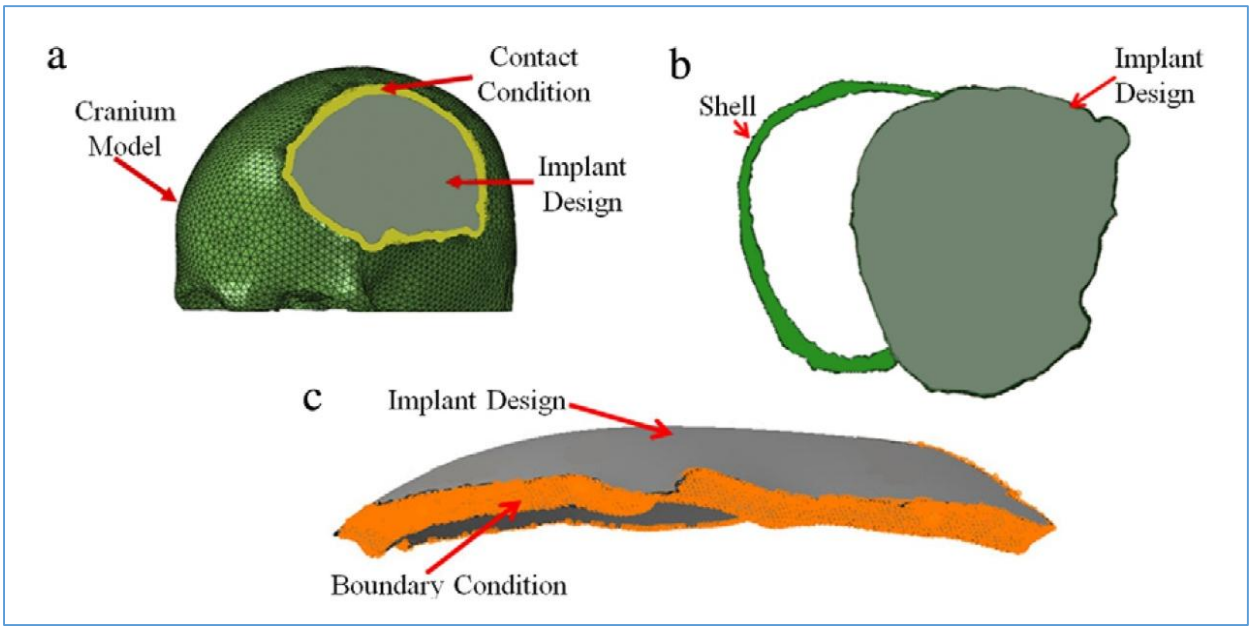

Figure 2.12 a) The contact region between skull and implant is defined as non-penetration type b) The fixed boundary condition (all DOF is arrested) on surface nodes of the skull c) Boundary nodes of the implant is constrained along normal direction of the skull [67]

The above implant is constrained in three different ways along with 60N load is applied. The implant behaviour is assessed through Displacement and Maximum principal stresses and compared the results. However, the percentage of change is observed as 8% while consider above boundary conditions. The 30% computational time was reduce in third boundary condition. Validation is done through mesh convergence test, while decreasing the element size the accuracy of the results were significantly increased and computational time also increases. Finally, mesh convergence done through repetitive mesh sizes until the change is < 1%.

Ridwan et al. 2016 investigated the cranial implant behaviour with different defect shapes (circular, triangle and irregular), contact angle (Negative, Zero and Positive) between implant and skull and furthermore the stress behaviour is studied in implant fixation screws as shown in Figure 2.13.
The bone, Ti6Al4V and PMMA material properties were considered and studied the behaviour of implant in Ansys software. The material is considered as homogenous, isotropic and linearly elastic [68]. The static load is applied at centre of the implant at a magnitude of 50N and global boundary

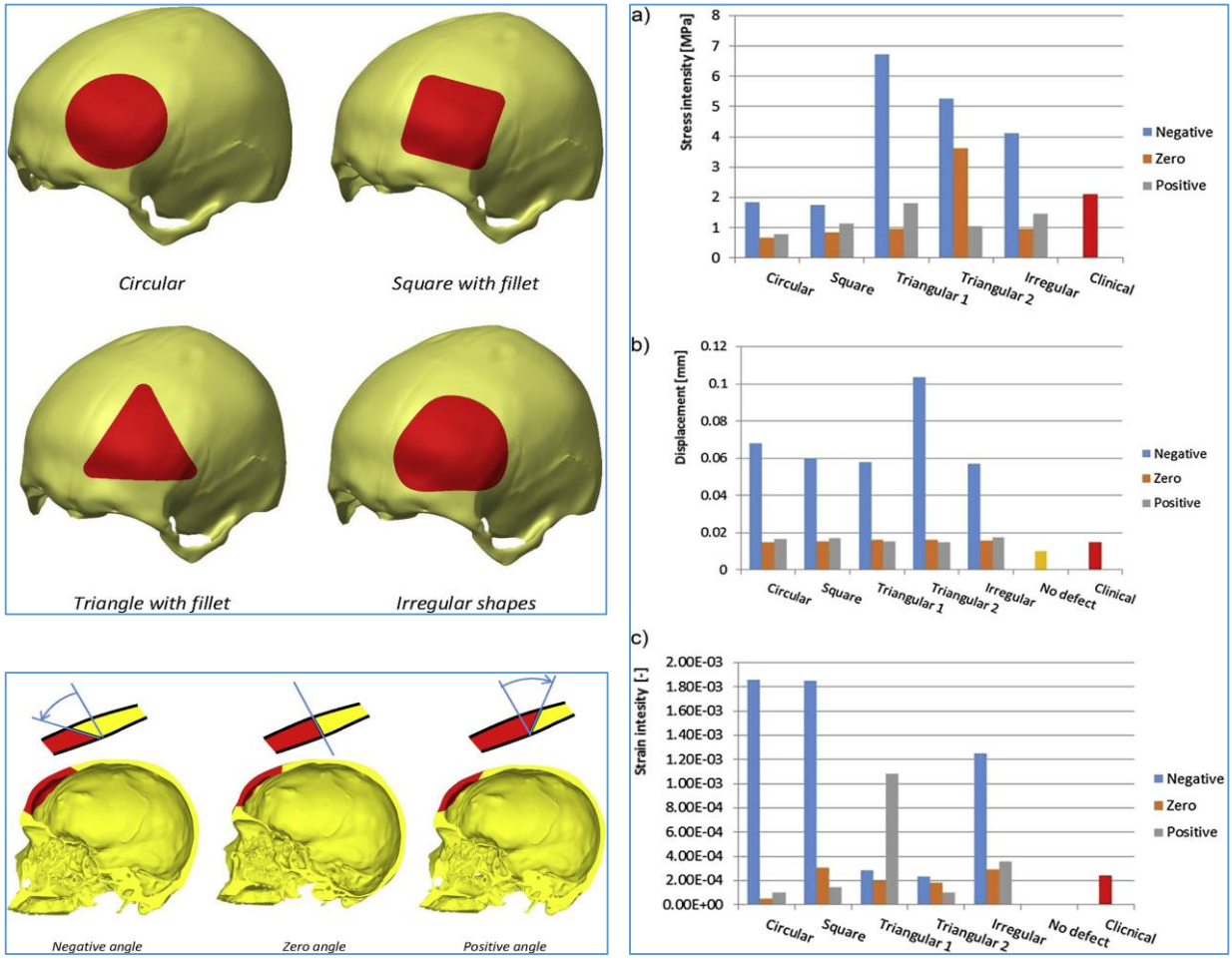

Figure 2.13 a) The skull with four different shapes circular, square, triangular and irregular b) The interface angle between skull and implant c) The implant behaviour under loading [68]

conditions are consider i.e. the contact region between skull and spine region is fixed all DOF. The frictionless contact was defined between bone and implant and remaining parts are meshed through Ansys software. The fine mesh was defined at threaded portion, and Element type is SOLID 186 and SOLID 187. Finally, the displacement and stress intensity is observed as shown in Figure 2.13.

Michael et al. 2007, Freytag et al. 2013, and Kosta et al. 2014. Recently adopted the meshless methods to investigate implant behaviour without using traditional finite element meshing [69]–[71]. These meshless methodologies are playing a vital role to simulate the human bones (CT scanned parts). The scan & solve approach is proposed and it is a solution structure method originate from Kantorovich and Rvachev [70]. This methodology is having lot of advantages over traditional FEM. The traditional FEM is an approximation method to mesh the geometry and chance to loss of original data, this meshless directly uses native geometry for simulation as shown in Figure 2.14. The mesh size is defined in FEM with smallest feature size and these are eliminated while doing simulation. However, the smallest feature size is preserved and handled automatically. The refinement of mesh is same in both systems such as h, p, and k systems [70].

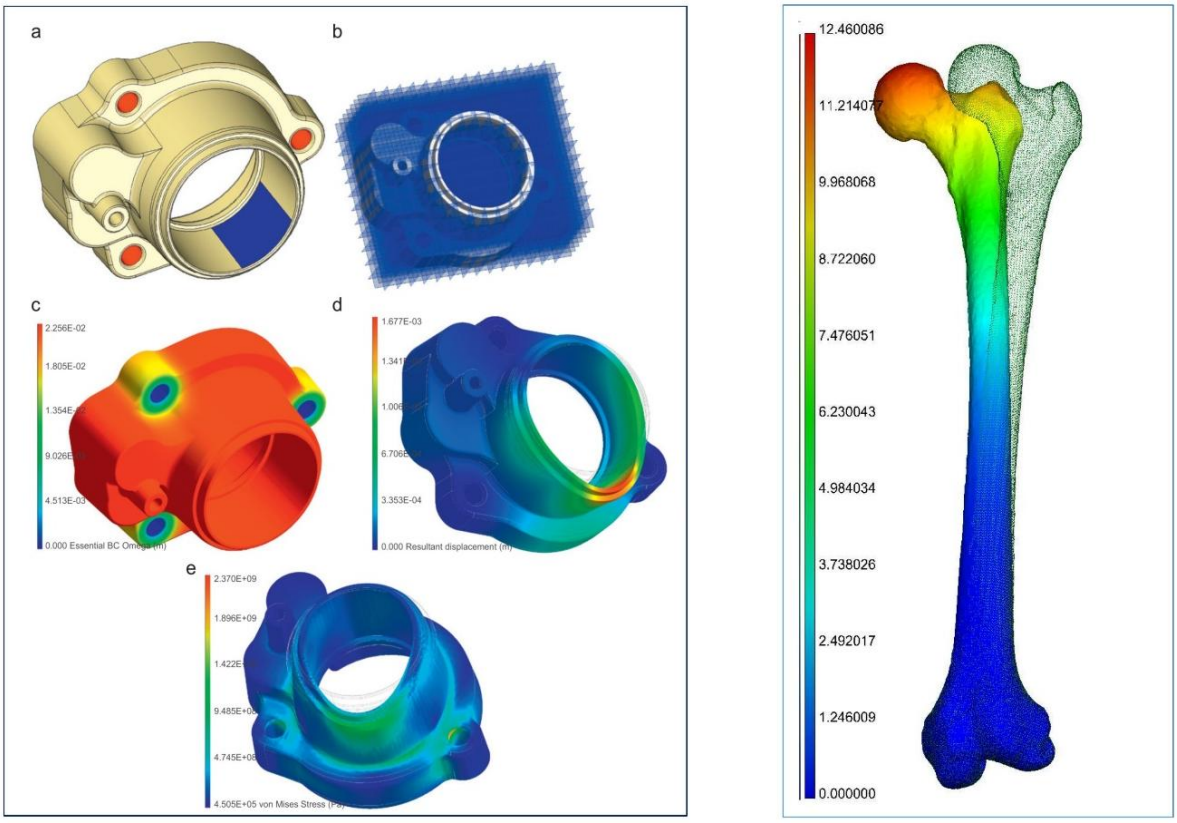

Figure 2.14 1) a) The solid boundary conditions red is fixed one and blue indicates load b) The body is divided into uniform grids with prescribed resolution c, d) The displacement values e) The von-Mises stress value. 2) Scaled deflection of solid bone computed with scan and solve [70]

2.14 Motivation

- Based on the literature survey, it is evident that less quantity of work is done on modelling techniques to handle various cranial defects and cranial implant embedded with scaffold structure and sustain at intracranial pressure with optimum number of fixation points (anatomical locations).
- Thus there is a scope for study on modelling techniques to handle large cranial defects, which is greater than 100 cm^2 (i.e. beyond midline deformities). However, the cranial implant is completely solid one, which cannot promote the tissue growth. Here, the challenge is involved to design an appropriate cranial implant, which promote tissue growth and sustain under intracranial pressure.
- From the literature, it has been observed that
  - The optimum number of anatomical locations are not defined for an implant under intracranial pressure loading and to seizure the CSF leakage
  - Few researchers are proposed sandwich type of cranial implant, however, there is no FE analysis on scaffold based cranial implant.
- From the literature, the customized scaffold based cranial implants for craniofacial surgery is very rare. However, the need for efficient and accurate analysis data is required to manufacturing the customized cranial implants for surgery.

2.15 Research objectives

- The main objective of the present research work is to develop the customized cranial implant by considering intracranial pressure and anatomical locations.
- The objectives are:
  - To develop novel computer aided modelling techniques for large size cranial defects.
  - To model the cranial implant with optimum number of anatomical locations and seizure the cerebrospinal fluid leakage.
  - To develop an algorithm for unit cell scaffold structure and study the permeability of scaffolds.
  - Identify the deformation of cranial implant using finite element method and meshless approach.
  - To develop the customized cranial implant and minimize the cost.

2.16 Work plan

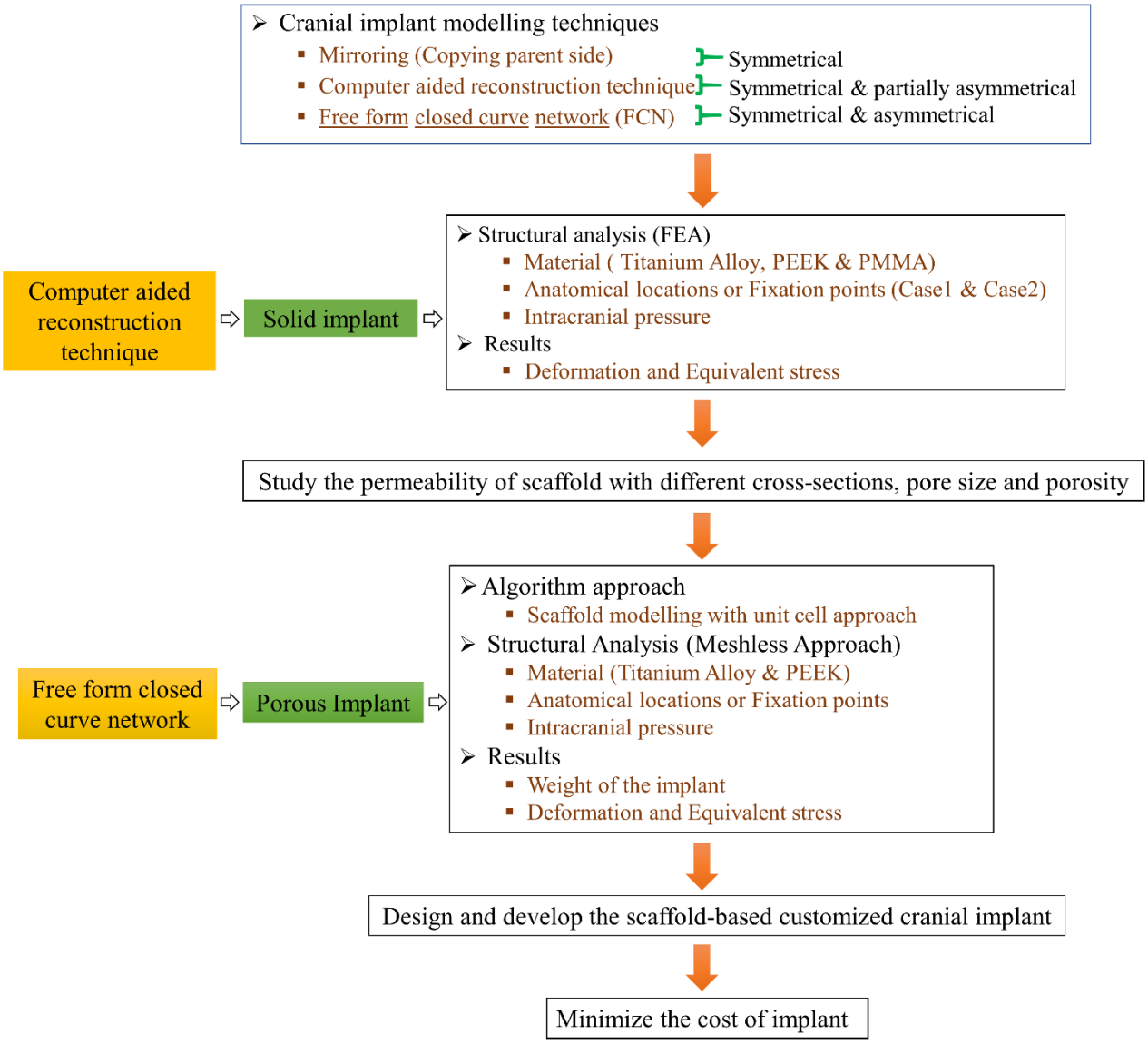

Figure 2.15 Flow chart of work plan

CHAPTER 3

3. 3D PRINTED, CUSTOMIZED CRANIAL IMPLANT FOR SURGICAL PLANNING

Main objective is to model cranial implant for skull injured person. The skull has been damaged in frontal, parietal and temporal regions and a small portion of frontal region damaged away from sagittal plane, complexity is to fill this frontal region with proper curvature. The Patient CT-data (Number of slices are 381 and thickness of each slice is 0.488 mm) was processed in mimics14.1 software, mimics file was sent to 3-matic software and calculated the skull thickness at different sections where cranial implant is needed then corrected the edges of cranial implant to overcome CSF (cerebrospinal fluid) leakage and proper fitting.

3.1 Introduction

The Cranioplasty is defined as a neurosurgical procedure to sheath an injured portion of the skull and these injuries are caused by accidents, tumours and congenital defects. The X-ray and 2D computed tomography are conventional methods for observing bone geometry. Therefore, these conventional methods are not much informative. Advances in imaging technology such as computed tomography (CT) and Magnetic resonance imaging (MRI) are playing a vital role to visualize and analyse patient data. The CT data is useful to manufacture the patient skull and customized implants with 3D printing technology [72]. The 3D models have been used to know the exact position of ablation tumours, plan surgery meticulously, and explain the problem clearly to the patients. These 3D models can improve psychological constancy of the patient [73]. However, the success of reconstructive skull surgery depends on consecutive operations.

While comparing the healthy portion of the skull with injured side, an accurate bone implant is required to replacement malformation area of the skull and the malformed bone is successfully planned with healthy portion. The malformed portion is effectively replace with healthy portion of the skull through mirroring technique. Before modelling the cranial implant, the STL data is exported to a computer aided design and computer aided manufacturing (CAD/CAM) systems for preoperative processes such as wrapping, fitting errors, and shape [73].

The integration of computer-aided design (CAD) and 3D Printing allows medical image systems to develop physical and real 3D hard copy [74]. The 3D printed models are beneficial to estimate

how much area of the bone is injured, pre-plan the surgery effectively with fixation screws. The prototypes are allows to assess the curvature of the implant, whether it replaces the original skull.

The cranial thickness is varying at different portions such as frontal, parietal, temporal, sphenoid and occipital. The skull thickness is depends on age and sex [75], [76].

The objective of present work is to model the precise cranial implant and pre-plan the surgery with successive operations [77]. Finally, these procedures are leads to considerable change in surgery time and overcome CSF leakage.

3.2 Materials and methods

3.2.1 Patient data collection

A CT-scan of 16 years old patient's fractured skull was collected from CT scan centre. Number of slices are 381 and thickness of each slice is 0.488 mm.

3.2.2 Observation of trauma case

The patient skull is sorely damaged at frontal, parietal and temporal regions as shown in Figure 3.1. At frontal region, the damage is crossed the mid line of the skull i.e. sagittal plane. The damaged portion of the skull is required suitable implant.

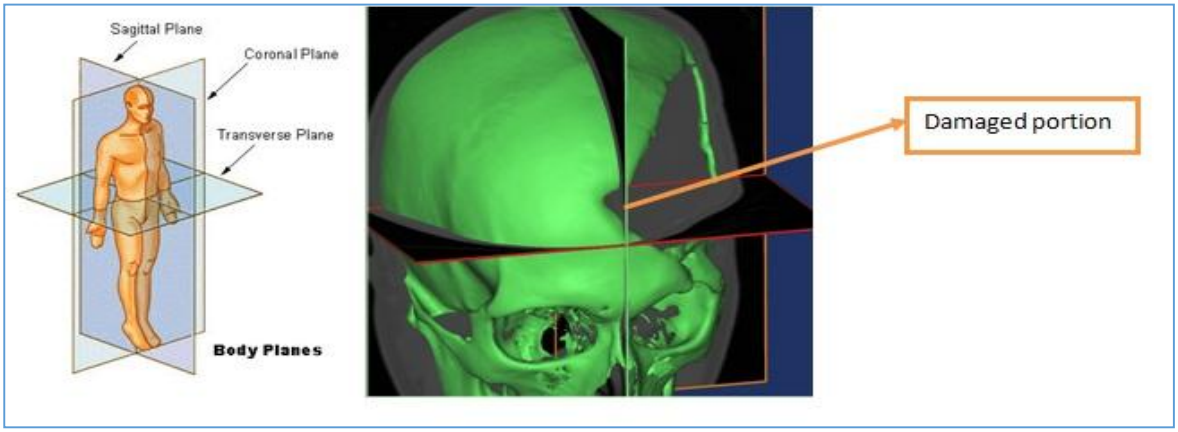

Figure 3.1 Damaged portion of skull with different planes

3.3 Methodology

3.3.1 3D Reconstruction of CT image data processing through MIMICS software

Advances in computer graphics such as image processing is revolutionized technology in medical imaging. The image processing is to convert the CT data to 3D Models, and they are clearly visualized at different views/orientations with varying colours, lighting and surface properties.

In this research, the medical imaging software MIMICS is used for processing CT scan images. The MIMICS software is capable of handling DICOM and other image formats, such as TIFF, JPEG, PNG, GIF, and BMP. The software is extensively capable of working with CT, MRI. The 3D image processing, image resizing, and image reslicing are most important features of this software. Other essential features such as thresholding / segmentation, region growing, rotation, scaling, reslicing, measurements, editing, examination of three dimensional volumetric data, assigning different object names for various tissues and capability of visualizing the objects either individually or together. The software has capabilities of exporting the 3D digital object in a compatible format i.e. STL format used to print prototype in 3D printing machines.

3.3.2 3D reconstruction of external geometry patient specific implants- MIMICS

The process of converting anatomical data from 2D CT images to 3D models is called segmentation. This segmentation consists

- Creation of an image data set
- Thresholding
- Region growing
- Calculate 3D or 3D reconstruction

3.3.3 Creation of image datasets

From the DICOM directory of files, a list is created with the relevant image slices pertaining to the pathology. Figure 3.2 shows the display of images in three orientations: axial, sagittal and coronal with a space to display the reconstructed 3D image. The images have a 512 X 512 pixel resolution.

3.3.4 Thresholding

For analysis of objects in an image, it is essential to distinguish between the objects of interest from "the rest." This latter group can also be referred to as the background. The techniques that are used to find the objects of interest are known as segmentation techniques - segmenting the foreground from background. Segmentation of CT 2D slice images is done by selecting specific image intensities (Hounsfield units) within the region of interest. The use of CT numbers, or Hounsfield units, provides an indication of the nature of the tissues being imaged.

Thresholding is done by selecting the upper and lower threshold values of image intensities. Specific tissues such as bone, skin, and muscles are identified by Hounsfield units (HU) is a system

to measure the attenuation coefficient of tissues in CT scan images. HU are also termed CT numbers. Bone has a higher Hounsfield value when compared to skin and soft tissues as it absorbs most of the radiation. The Hounsfield values are predefined scale (the range minimum -1023 to maximum 3071) in the Thresholding tool bar for observing bone, soft tissue, compact bone, spongy bone & fat tissue etc. for this work the threshold value started at 226 as Bone (CT) as shown in Figure 3.3a.

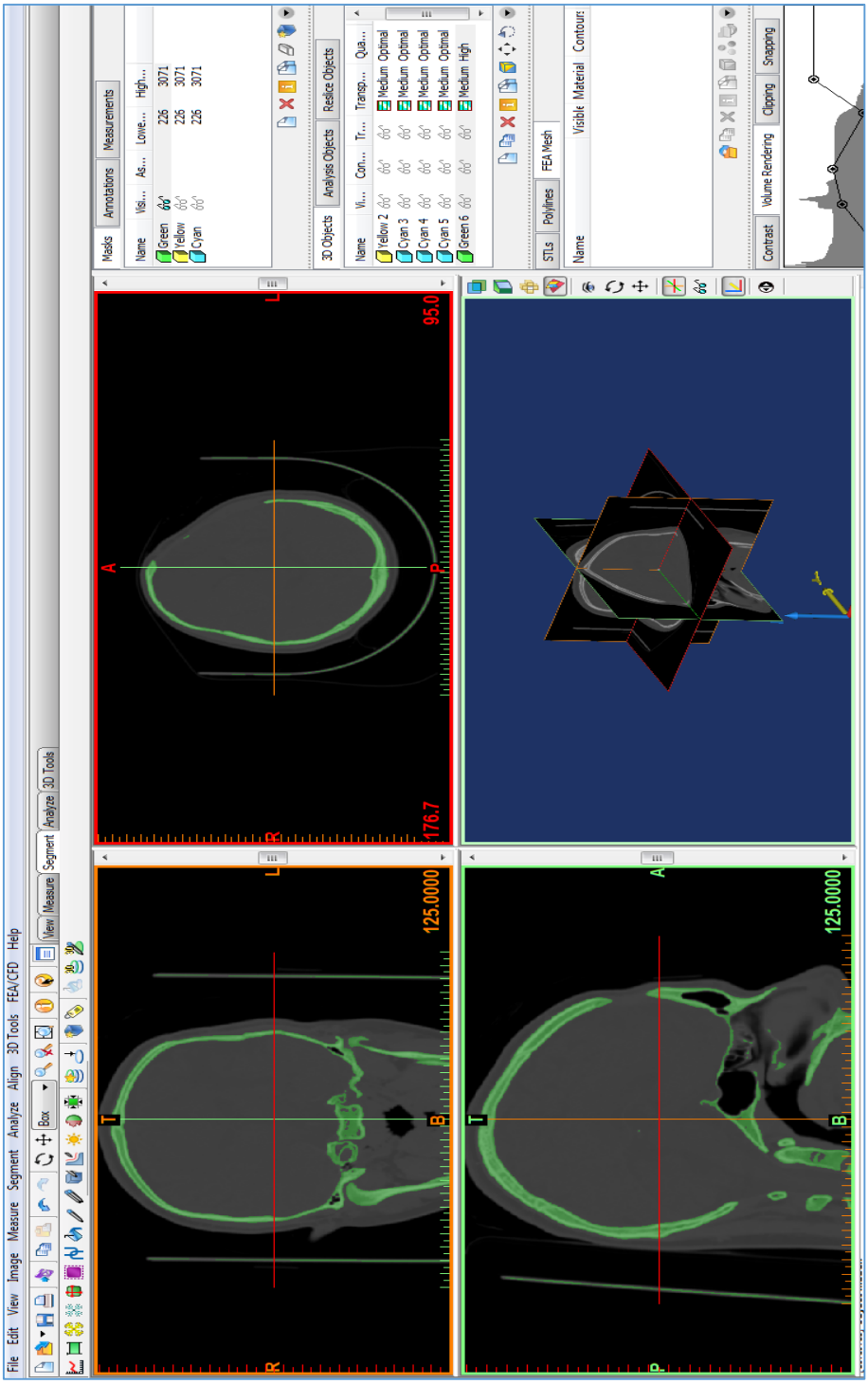

Figure 3.2 3D Reconstruction of external geometry

3.3.5 Region growing and 3D reconstruction

Region growing is used to separate masks into different parts and is the process by which noise is minimized. The remaining soft tissue structures presented in the CT images are eliminated, resulting in a set of pixels that are related to skull are considered at each layer of data.

Calculate 3D tool convert 2D CT image data to 3D model (Figure 3.3b), before completion of this work, broken bone particles were erased at different layers of CT images [7]. After successive erasing operations the 3D model is obtained. The process was carried out many times to get best output.

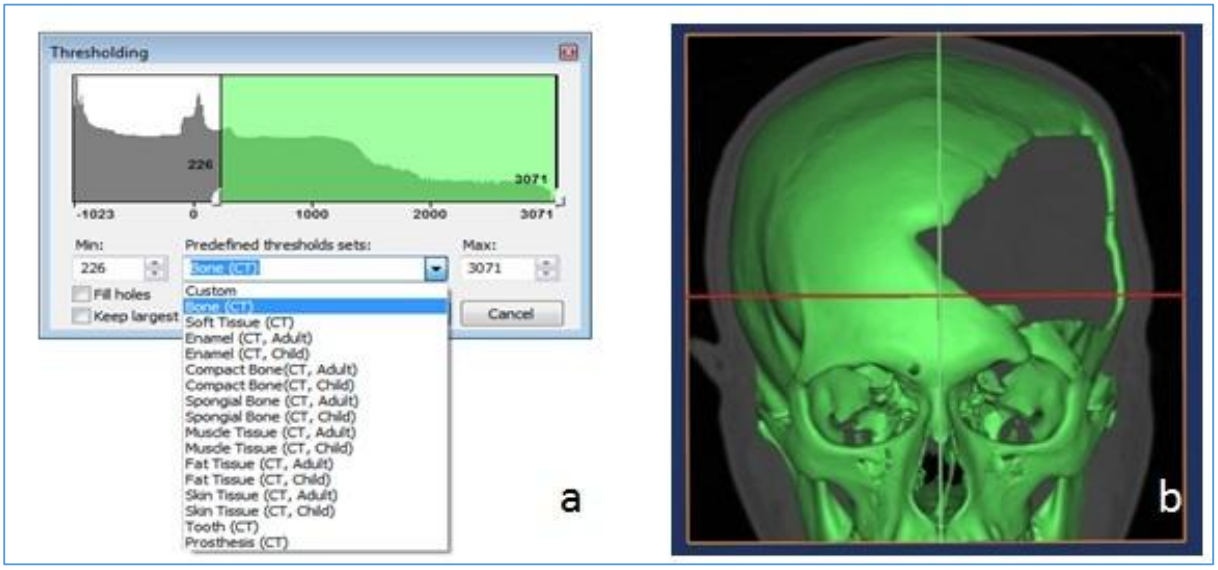

Figure 3.3 a) Thresholding tool bar for different biological materials b) Calculated 3D

3.4 Cranial implant modelling

The cranial implant is modelled with 3-matic software. Essentially, the modelling is involved with two stages such as pre-processing and post-processing

3.4.1 Pre-processing stage

The injured portion of the skull thickness is measured at various regions such as frontal, parietal and temporal regions. Thicknesses at lower and upper frontal bone (Figure 3.4a) are 3.78 mm, 6.74 mm, 6.18 mm, and 3.18 mm. In upper region of parietal bones (Figure 3.4b) are 3.82 mm, 3.99 mm, 3.74 mm, and 3.32 mm etc. In bottom region of parietal bone (Figure 3.4c) are 3.66 mm, 3.78 mm, and 3.67 mm. In bottom region of temporal bone (Figure 3.4d) are 2.87 mm and 2.67 mm. From above values, the average cranial implant thickness is decided as 2.5 mm and 3.5 mm.

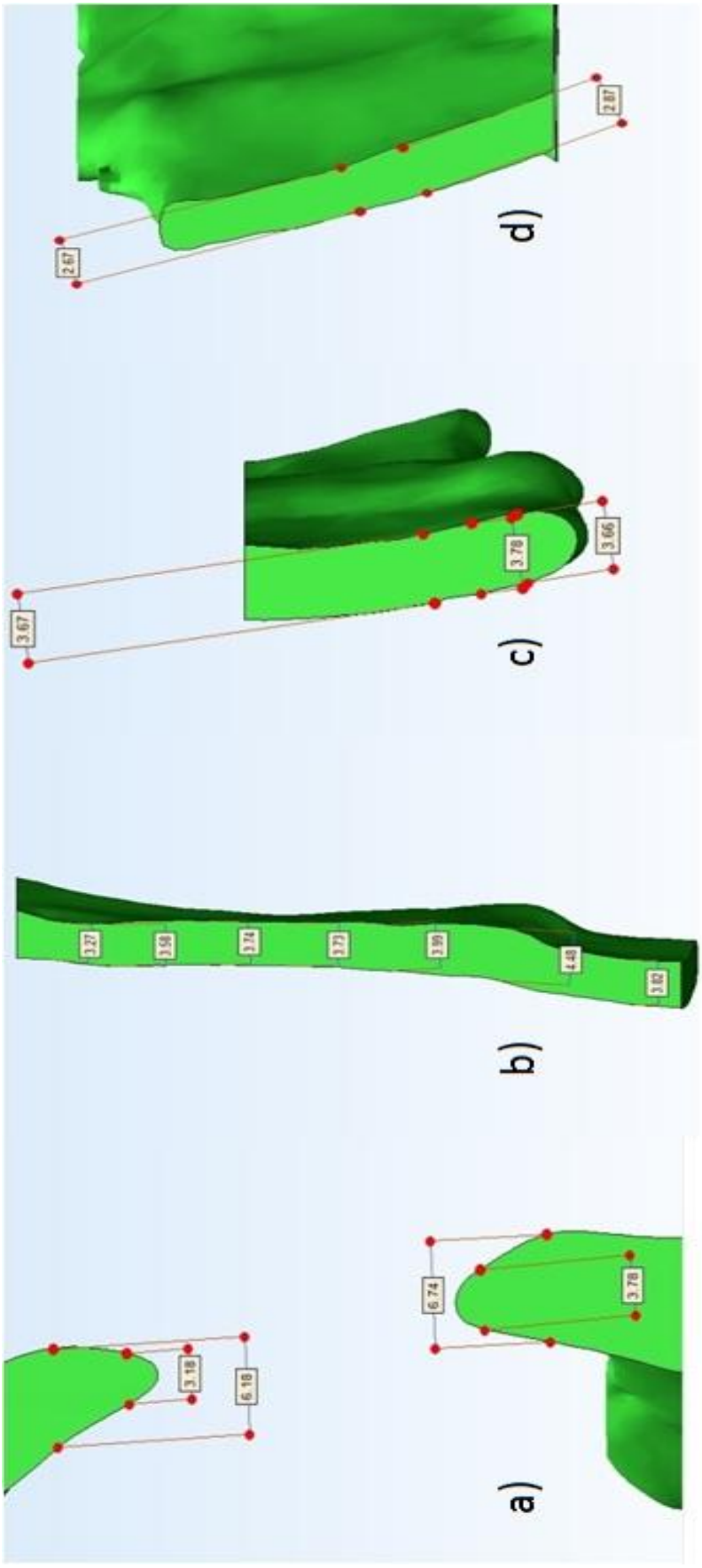

Figure 3.4 Thickness of damaged skull at different cross-sections a) Lower and upper thickness of frontal bone b) Upper thickness of parietal bone c) Bottom thickness of parietal bone d) Bottom thickness of Temporal bone

Then skull is positioned in sagittal plane with three landmark points and it is (Figure 3.5a) processed through various computer aided operations such as cropping and wrapping. The cropping (Figure 3.5b) and wrapping (Figure 3.5c) tools to make model easier. The guiding curve has been drawn (Figure 3.5c) and attached at ends [74].

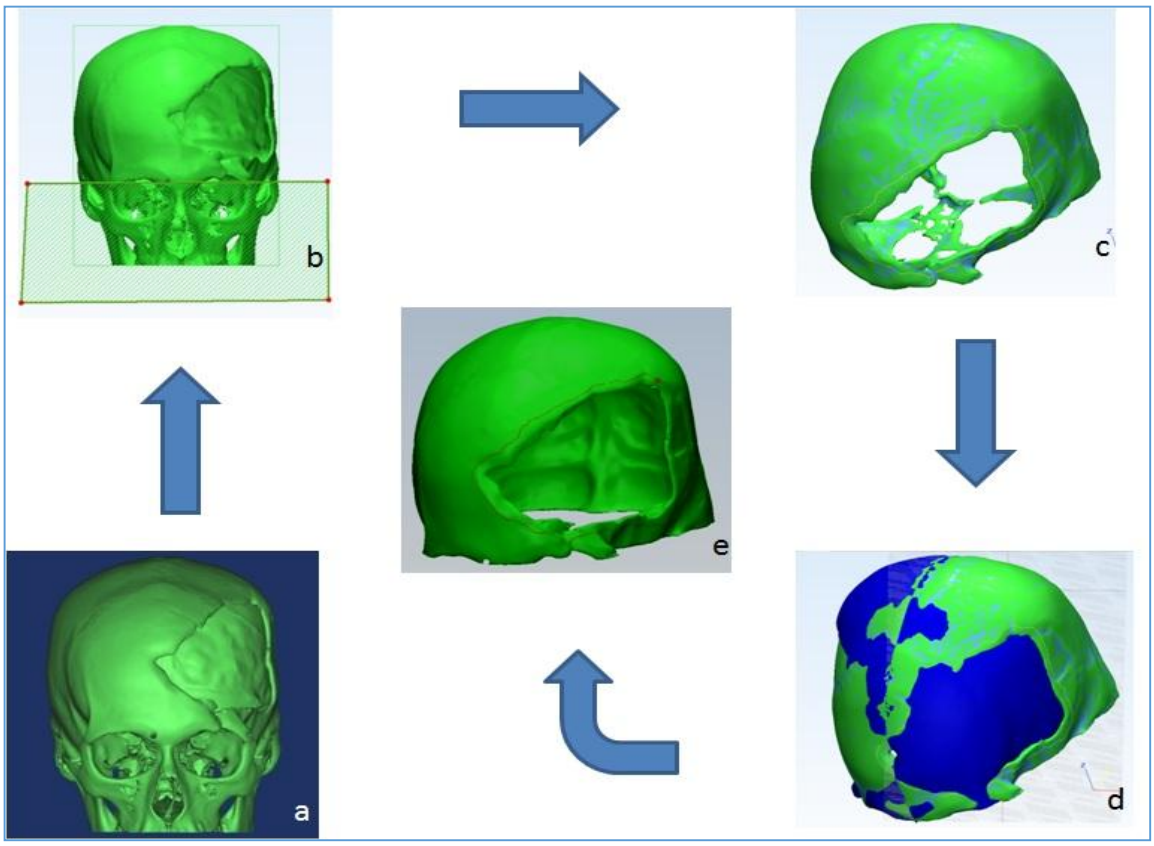

Figure 3.5 Guiding curve for implant a) Processes skull from MIMICS b) Cropped region of skull c) Wrapping of skull d) Mirroring the skull through sketch (from sagittal plane) e) Guide curve for prosthesis

The curvature of the cranial implant is controlled with spline curves and these splines are drawn at different regions to get optimum surface of the cranial implant. The first spline-curve drawn at frontal bone region (Figure 3.5a and 3.5b), second one drawn between lower to upper portion of parietal region (Figure 3.5c and 3.5d) and last one drawn between frontal region to parietal region (Figure 3.5e and 3.5f). These spline-curves are manually adjustable. Finally, the cranial implant is modelled (Figure 3.5f) with the use of guiding curves and splines.

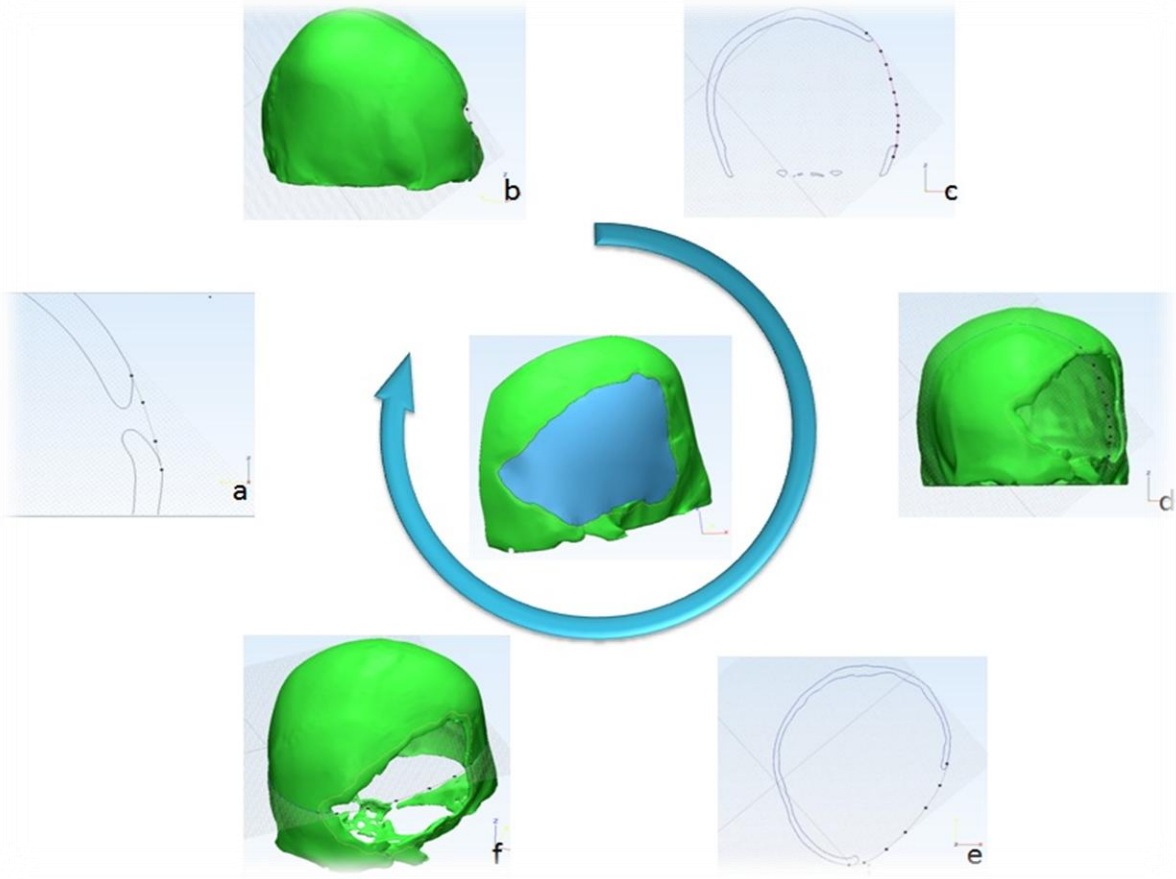

Figure 3.6 Spline curve based implant a,b) Frontal bone region c,d) Parietal bone region e,f) Temporal bone region

3.4.2 Post-processing

The implant fitting and curvature is improved subsequently with subsequent computer aided modelling operations.

The cranial implant is modelled with best thickness as 2.5 mm and 3.5 mm (Figure 3.6a). There was 1.4 mm extended portion is observed in 3.5 mm thickness implant (Figure 3.6b) to eliminate this extended portion 2.5 mm thickness implant is modelled.

The edges of the modelled implant are irregular which causes improper fitting to the host bone. To enhance the fitting with host bone, the edges of cranial implant (Figure 3.6c) was chamfered at an angle 25-30 degree, (Figure 3.6d). Finally, the perfect cranial implant is modelled (Figure 3.6e) [74] and appropriate fitting comprises overwhelmed CSF leakage.

3.5 Results & discussion

Both CT images and prototypes were supportive for preoperative evaluation of the custom implant design and planning of surgery. The 3D models and custom implants are beneficial for reducing the surgery time. The cranial implant is modelled successfully with above mentioned software's. However, the implant is showing clearance problem as show in Figure 3.7.

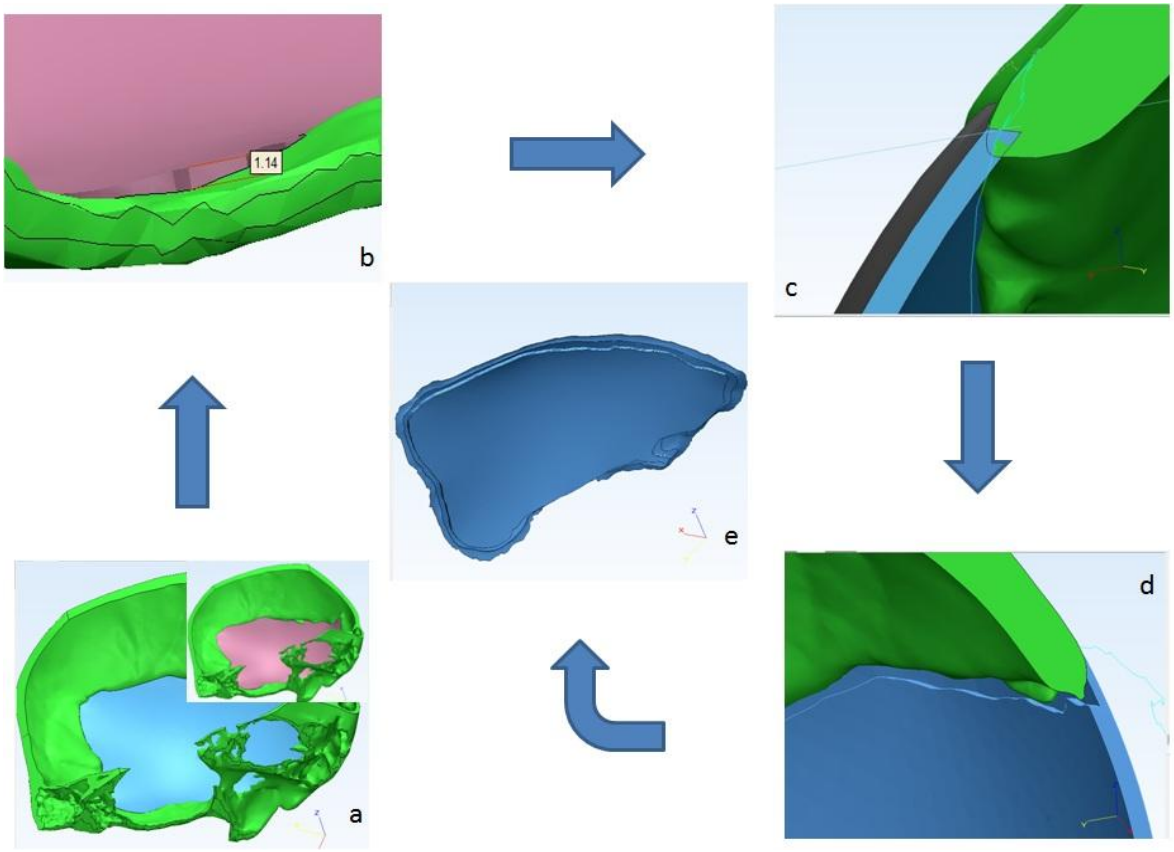

Figure 3.7 Final accurate implant a) 2.5mm thick verses 3.5mm thick implant b) Extended portion of 3.5mm thick c) Merged edges of implant in original bone d) Chamfered edges for fitting e) Final implant

The implants are modelled with maximum possible clearance and these are 3D printed with ABS plastic material. Among two configurations, the second one is showing best fitting compare to first one as shown in Figure 3.8. The first one is having problems with improper edges and clearance. The proper fitting is leads to decreases the CSF leakage.

Figure 3.8 Final product 1) Chamfered edges with max clearance 2) Modified chamfered edges with less clearance

3.6 Conclusion

The implant is successfully modelled with best fitting. The 3D printed models are valuable, accommodated the estimation of damaged skull for surgery planning. Especially, the surgeon can understand and estimate the injured portion of the skull. Precise fitting of the implant has been fabricated in order to re-establish of spline curves. In addition, the surgery time can be reduced considerably. A trivial clearance is observed between final implant and the skull. Therefore, this clearance problem can overcome thorough additional computer-aided modelling procedure. The entire work has done through high-end commercial software's which leads to increase in cost of the implant.

CHAPTER 4

4. MODELLING AND ANALYSIS OF CRANIAL IMPLANT: BEYOND MID-LINE DEFORMITIES

This computational study explores modelling and finite element study of the solid implant under Intracranial pressure (ICP) conditions with normal ICP range (7 to 15 mm of Hg) or increased ICP (>I5 mm of Hg). The implant is modelled through novel modelling approach is computer aided reconstructive technique with the help of Rhinoceros software. This modelling method is applicable for symmetrical defects and partially for asymmetrical defects such as beyond middle line deformities. The implant fixation points allows implant behaviour with respect to intracranial pressure conditions. However, increased fixation points leads to variation in deformation and equivalent stress. Consequently, the mechanical deformation and equivalent stress (von-Mises) are calculated in ANSYS 15 software with distinctive material properties such as titanium alloy (Ti6Al4V), polymethyl methacrylate (PMMA) and polyether-ether-ketone (PEEK). Finite element analysis is providing a valuable insight to know the deformation and equivalent stress.

4.1 Introduction

Cranioplasty [28] deals with treatment of skull injuries and defects with an established surgical procedures. The main aim of these procedures is to restore the protective function of the skull and cranial aesthetics. To date various materials have been used for the treatment of cranial defects – titanium alloy (Ti6Al4V), polymethyl methacrylate (PMMA) and polyether ether ketone (PEEK).

The medical imaging techniques, Computer Aided Design and Manufacturing techniques (CAD/CAM) offers new possibilities in fabrication of patient specific titanium and PMMA and PEEK implants with 3D printing technology. Most of the customized cranial implants fabricated based on patient specific data [30], [31], [78] this data is in Digital Imaging and Communications in Medicine (DICOM) format obtained from Computed Tomography (CT) [12], [28], [79] and Magnetic Resonance (MRI). A typical spatial resolution in microns with less slice thickness is required to get better solid model for hard tissues. This acquired image data sets are processed and subsequently converted into Standard Tessellation language (STL) file formats that are required for 3D printing [78].

The skull is symmetrical for many humans. The skull injuries were categorized in to symmetrical and asymmetrical defects [12]. In symmetrical defect, the malformation portion can be planned

with an ordinary side of the skull [12], [28], [78] through Computer Aided Modelling software (Rhinoceros). The asymmetrical defect was not full filled by mirroring technique. These asymmetrical defects and complex deformities which include multiple injuries deals with reverse engineering technique [12], [72], [80]. A slight modification of reverse engineering technique is required to model an implant for beyond midline defects.

PMMA, PEEK and titanium alloys are most commonly used materials [30], [78], [81]–[83] in the fabrication of customized patient specific implants [80], [83], [84]. However, these materials are substantially bio-compatible, successfully implanted for skull and femur bone injuries. The PEEK is successfully implanted in Mexico for an oncology patient [81]. Furthermore PEEK and PMMA materials are safe, lightweight and easy to use. These materials do not produce blemishes on computed tomography (CT), which makes easy to follow-up the oncology patient.

The pressure inside the cranial cavity is called intracranial pressure (ICP) [85], [86]. It varied with age, body position and affects the cranial implant after surgery. The normal range of ICP is 7-15 mm of Hg [2], [85] for an adult human being. An effective way of analysing implant design is by performing finite element (FE) based simulations[65], [67], [68], [72]. This methodology can be employed to assess the deformation and equivalent stress in the implant with respect to variables in the design.

The PEEK and titanium alloy implants are commonly produced and fabricated by 3D printing. Lack of standardized methodologies, potentially leads to unsuccessful treatment associated with clinical and financial implications. The aim of this study is to model the cranial implant for beyond mid-line defects and to investigate the mechanical behaviour of skull implant at various loading conditions with respect to fixation points.

4.2 Modelling of an implant: beyond mid-line defect

The DICOM (Digital Imaging and Communications in Medicine) images are processed in MIMICS software [64], [79] to get mesh file of the skull. The patient skull was assumed to be symmetrical along its mid-sagittal plane (Figure 4.1a), the replication of missing bone fragment (red colour skull) mirrored from original skull. However, frontal bone of skull is not filled properly as shown in Figure 4.1b. This case is comes under beyond mid-line defect.

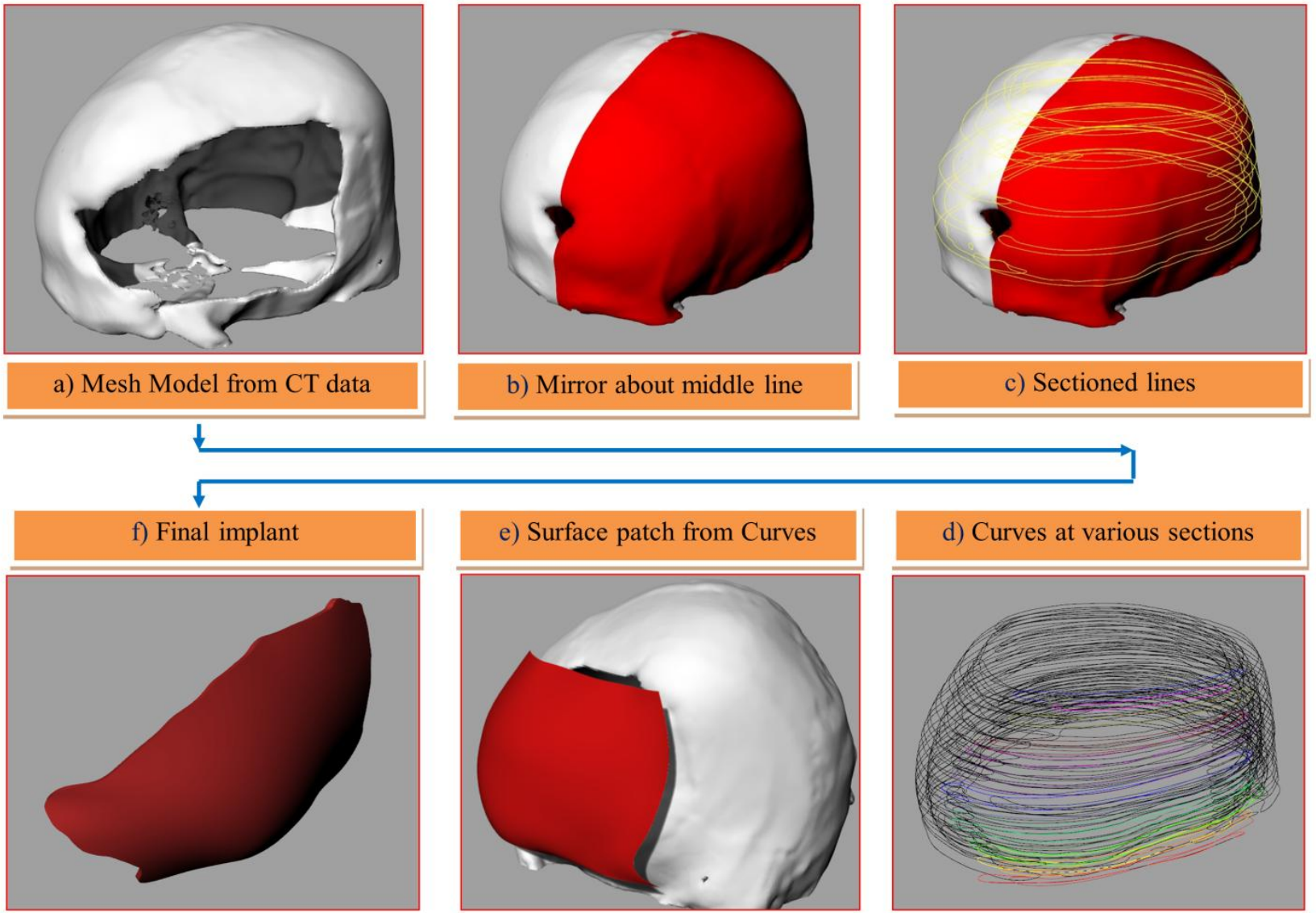

Figure 4.1 Flow chart for modelling of the skull implant

Contour profile of an implant is not obtained through the projection of mirrored data of skull. The computer-aided reconstruction engineering technique is (uses surface interpolation, such as a NURB (Non uniform rotational B-spline) surface [12], [82]) an approximation method to develop the surface for cranial hole with proper fitting.

This technique is applied to control the surface by using profile curves and to fill frontal portion of skull. Before modelling of an implant, skull is sectioned at various levels based on height (Figure 4.1c) and a total of 24 sections are considered as shown in Figure 4.1d. On each sectioned layer a profile curve is drawn and the shape of profile curve follows based on sectioned layers of mirrored skull. From Figure 4.1d, the black line indicates sectioned layer and colour line indicates profile curve.

The surface patch is generated with profile curves (Figure 4.1e) and a best-fitted surface is obtained through a trimming operation. The surface was extruded perpendicularly at a length of 4mm and chamfered the edges with 30-45 degrees as shown in Figure 4.1f. These chamfered edges are utilized to fit an implant appropriately with the skull [31], [84].

4.3 Material properties

The material properties assumed to be linearly elastic, homogeneous and isotropic. For this study titanium alloy (Ti6Al4V), polymethyl methacrylate (PMMA) and polyether ether ketone (PEEK) materials [68], [87] are considered for finite element analysis.

Table 4.1 Material properties for skull implant

Material properties for Structural analysis			
	Titanium alloy (Ti6Al4V)	**Polymethyl methacrylate (PMMA)**	**Polyetheretherketone (PEEK)**
Young's Modulus (MPa)	110000	3000	4000
Poisson's ratio	0.3	0.38	0.4
Ultimate tensile strength (MPa)	950	72	103
Yield Strength (MPa)	800	72	100
Density (Kg/mm^3)	4430e-9	1180e-9	1360e-9

When tetrahedral element size decreases, the accuracy of a component, file size and number of elements were increased. Therefore the element size is fixed at 0.5 mm in both the cases. However, the volume of model is compared before and after meshing and it is observed that only a difference of 2-3% with fine mesh.

Table 4.2 Mesh data for both cases a) 8 fixation points b) 10 fixation points

Implant data		
	Case1: 8 fixation points	**Case2: 10 fixation points**
Max element size (mm)	Edge length= 0.5	Edge length = 0.5
Nodes	437982	437225
Elements	2333003	2327897
Volume (mm^3)	20800	20782

Table 4.3 Implant Specifications

Thickness	4 mm
Chamfered angle	30-45 degrees
Fixation point area	Typically 3-4 mm^2
Surface area	Typically 12.5*6 cm^2

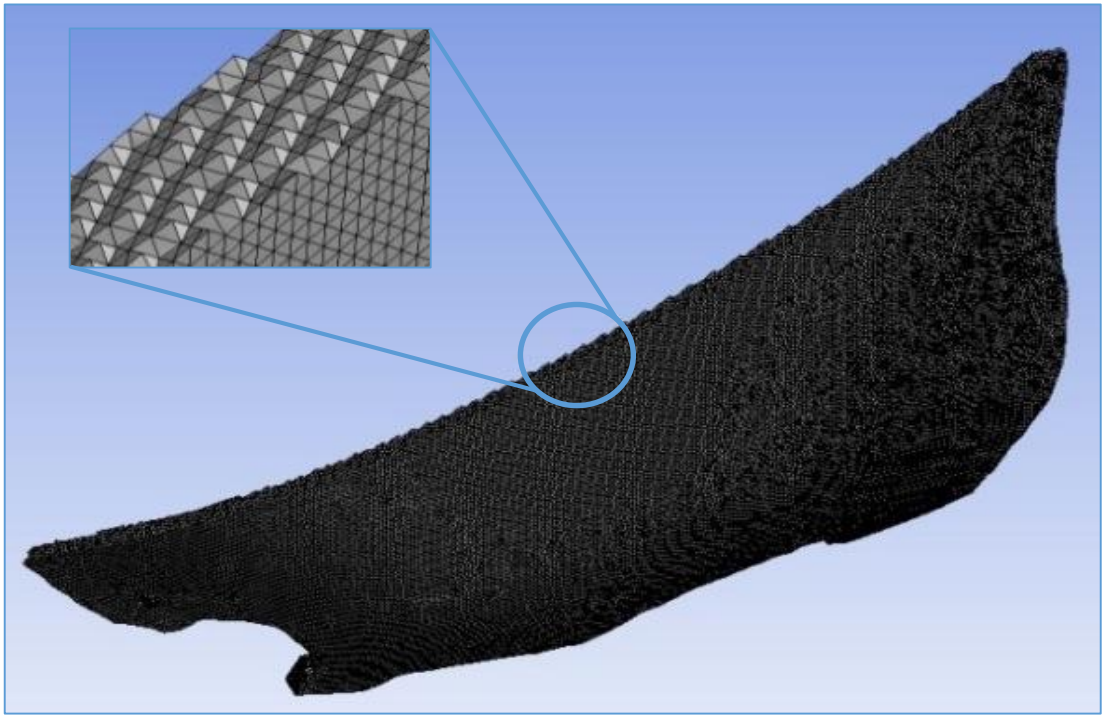

Figure 4.2 Cut section model with tetrahedral element size

4.4 Defining the fixation points

The fixations points are playing vital role which aid to arrest the CSF leak. There is no standard procedures are available to place the fixation points, however, these are randomly placed by the surgeon while doing surgery.

Firstly, the fixation points are selected at the corner of the implant because where ever the implant shape is changing respectively the stresses are concentrated at that point. With this procedure, the implant is modelled with three fixation points (Figure 4.3a) subsequently applied the intracranial pressure at inner surface. Due to the application of intracranial pressure and boundary conditions the maximum deformation was located top portion i.e. parietal bone and bottom portion i.e. temporal bone of the implant as shown in the Figure 4.3b. This maximum deformation causes CSF leak. According to this result three more fixation points are added. Among that two are at parietal bone region and one is at temporal bone region which denotes that the cranial implant is having six fixation points.

Subsequently, the implant is having six fixation points, simulated under above mentioned loading and boundary conditions. The implant showed maximum deformation at left edges i.e. frontal

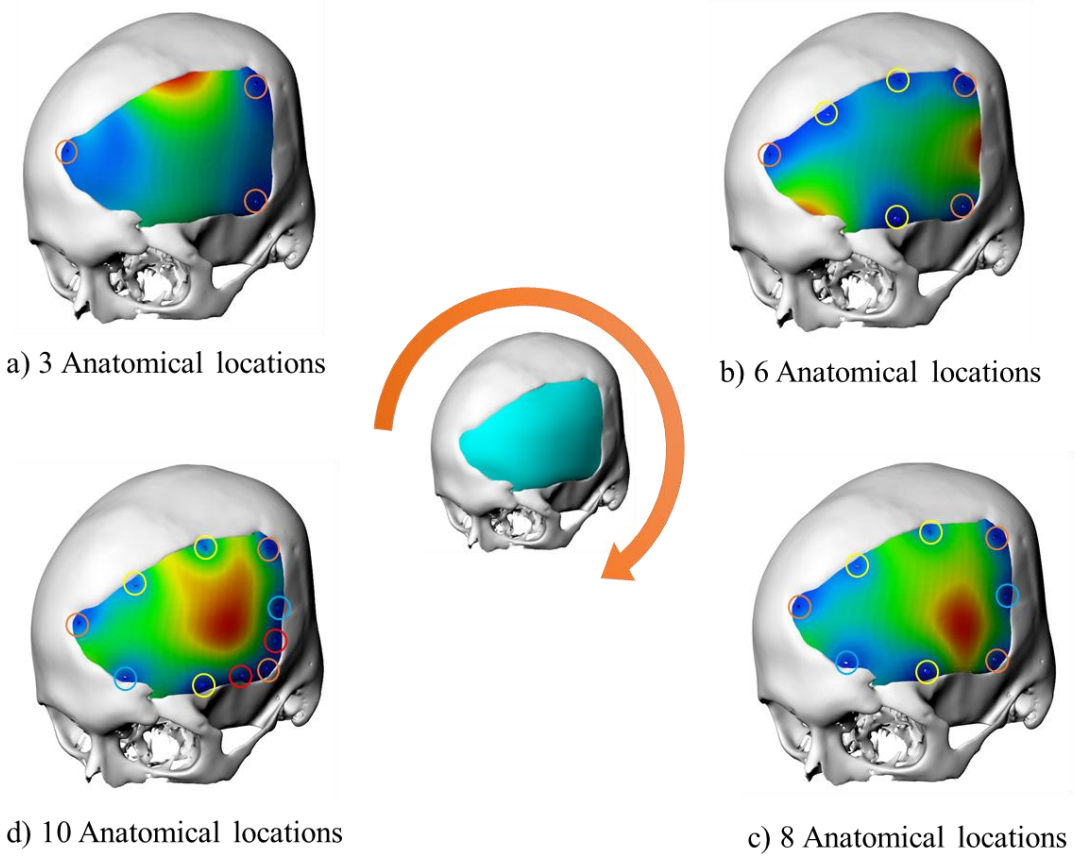

Figure 4.3 Configuration of fixation or anatomical locations

region which is near to orbital bone and topmost right i.e. near to junction of parietal and occipital bone. Correspondingly, two more fixation points are added and simulated as shown in the Figure 4.3c.

In the eight fixation point configuration, the deformation was propagated towards temporal region which can arrested by two more fixation points. Finally, the deformation is adjust and propagated towards centre of the implant as shown in the Figure 4.3d.

4.5 Loading conditions

A static pressure of 7 mm of Hg and 15 mm of Hg [85], [86] are considered based on intracranial pressure conditions Table 4.4. The pressure was applied on the inner surface and evenly distributed over an area of implant as shown in Figure 4.4 Fixation points a) Case1:8 fixation points b) Case2:10 fixation points. These implants were fixed at holes with two different cases of 8 number of fixation points (A, B, C….. G, H) and 10 number of fixation points (A, B, C….. G, H, I, J). These are categorized into case1 and case2.

Table 4.4 Loading data for finite element analysis

Loading data		
	Minimum Load	**Maximum Load**
Intracranial Pressure	7 mm of Hg (9.34e-4 MPa)	15 mm of Hg (2e-3 MPa)

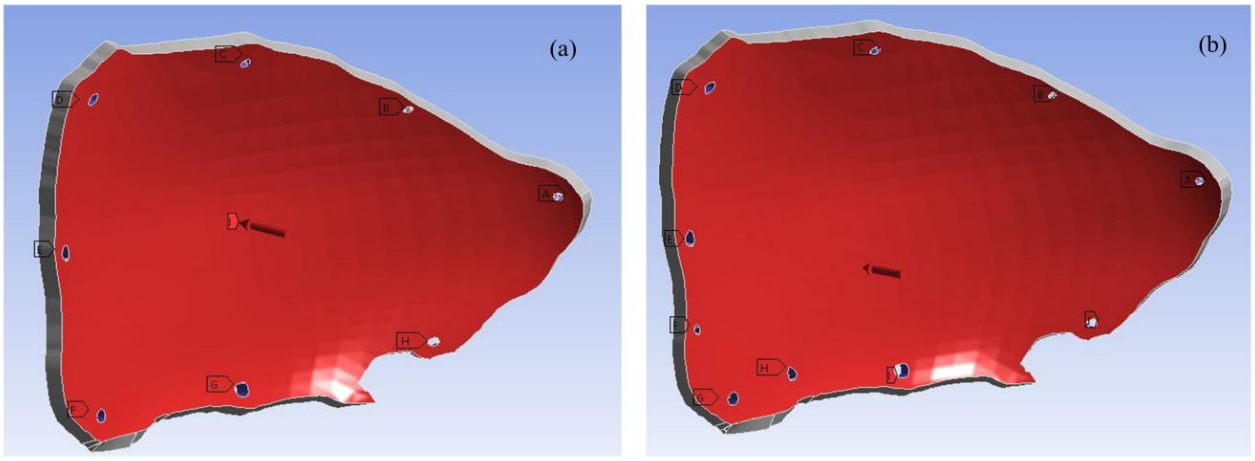

Figure 4.4 Fixation points a) Case1:8 fixation points b) Case2:10 fixation points

4.6 Meshing and validation

The STL file [72], [78] is discretized with tetrahedral elements [67], [68] using ANSYS 15 software. Element size allows you to specify the edge length for entire model (Figure 4.2). When tetrahedral element size decreases, the accuracy of a component, file size and number of elements were increased. Therefore the element size is fixed at 0.5 mm in both the cases. However, the volume of model is compared before and after meshing and it is observed that only a difference of 2-3% with fine mesh.

The validation of numerical analysis on bio-realisticity models is quite complex, when targeting a patient. The verification of theoretical model becomes the fundamental aspect [88] and many predictions come in to picture.

Convergence studies is conducted on model with different element sizes to get optimum mesh density in terms of processing time and accuracy to validate the grid dependency. The results of all models are almost same. However, the models of 2.333 million elements (case1) and 2.327 million elements (case2) converges faster (Table. 3) than the others due to mesh quality. Therefore the same method is applied for all other models. There is no appearance of hour glassing due to less complexity of an implant.

This implant is merely recommended for preoperative planning as this study was not yet recommended by clinicians with a guideline. The results are presented here for future perspective and it is fundamentally difficult to validate with numerical analysis [89].

4.7 Results

A total of 12 combinations are obtained in two cases with respect to type of implant materials and loading conditions. They are simulated and analysed to evaluate the total displacement and equivalent stress. The higher stress magnitudes were mainly concentrated at near to the centre of an implant.

4.7.1 Case1

It is observed that Ti6Al4V shows low deformation when compared with PEEK and PMMA. The deformation is 2.9068e-5 mm at minimum load and 6.2244e-5 mm at maximum load.

Table 4.5 Deformation and Equivalent stress analysis report for case1 (8 fixation points)

Structural analysis report	Case1					
	Titanium alloy (Ti6Al4V)		Polymethyl methacrylate (PMMA)		Polyetheretherketone (PEEK)	
	Min Load	Max Load	Min Load	Max Load	Min Load	Max Load
Deformation (mm)	2.91e-05	6.22e-05	1.03e-03	2.20e-03	7.62e-04	1.63e-03
Equivalent stress (von-Mises) MPa	0.22649	0.48499	0.21606	0.46265	0.21246	0.45494

It is observed that PEEK shows minimum equivalent stress when compared with Ti6Al4V and PMMA. The equivalent stress is 0.21246 MPa at minimum load and 0.45494 MPa at maximum load as shown in Table 4.5.

4.7.1.1 Titanium implant behaviour at minimum load

The implant behaviour is depends on boundary conditions such as fixations and intracranial pressure. The 8 fixation points are considered at minimum ICP, then the maximum deformation is identified at centre of the implant and minimum deformation at point “A” consequently, the maximum von-Mises stress at point “F” and minimum at point “A” as shown in Figure 4.5.

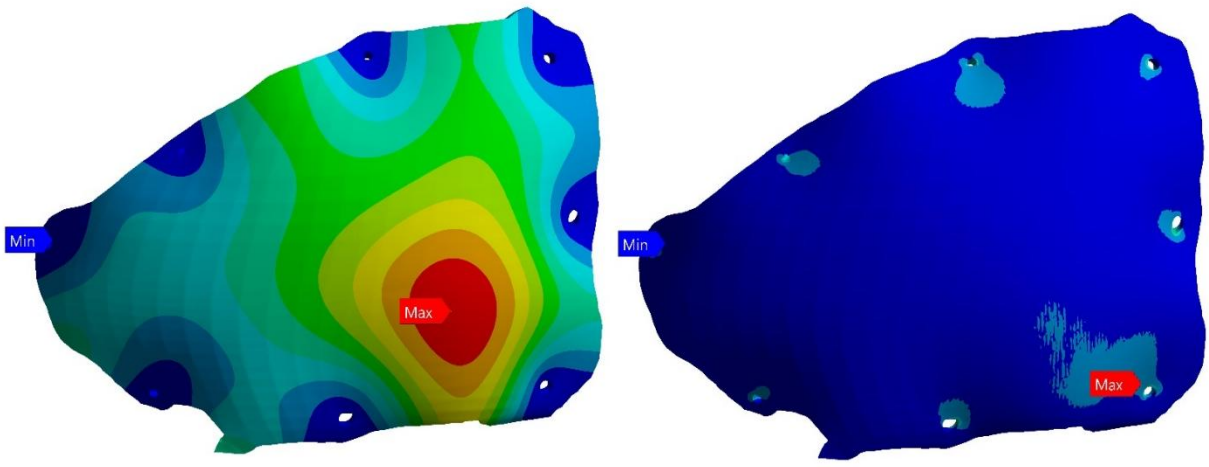

Figure 4.5 Titanium implant deformation and von-Mises stress at minimum load

4.7.1.2 Titanium implant behaviour at maximum load

The 8 fixation points are considered at maximum ICP, then the maximum deformation is identified at centre of the implant and minimum deformation at point "A" consequently, the maximum von-Mises stress at point "B" and minimum at edge of the implant as shown in the Figure 4.6.

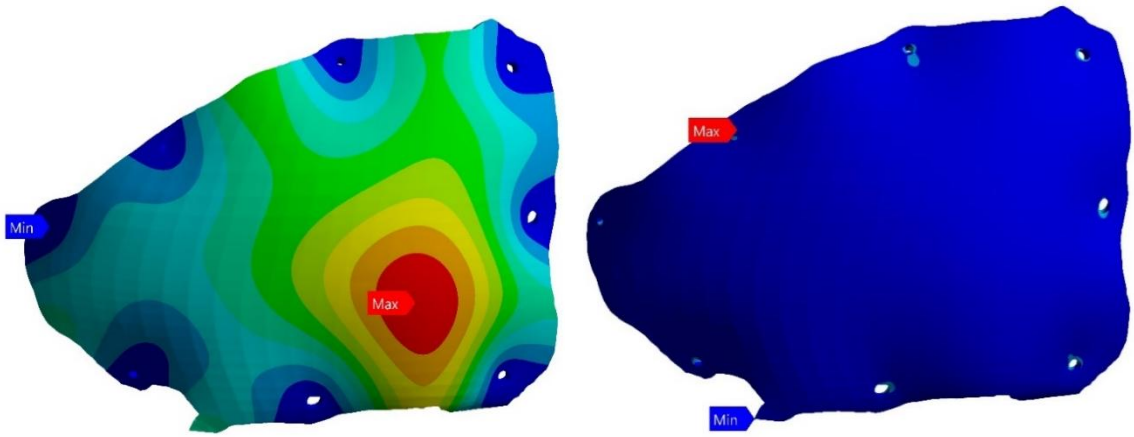

Figure 4.6 Titanium implant deformation and von-Mises stress at maximum load

4.7.1.3 PEEK implant behaviour at minimum load

The 8 fixation points are considered at minimum ICP, then the maximum deformation is identified at centre of the implant and minimum deformation at point "A" consequently, the maximum von-Mises stress at point "F" and minimum at point "A" as shown in Figure 4.7.

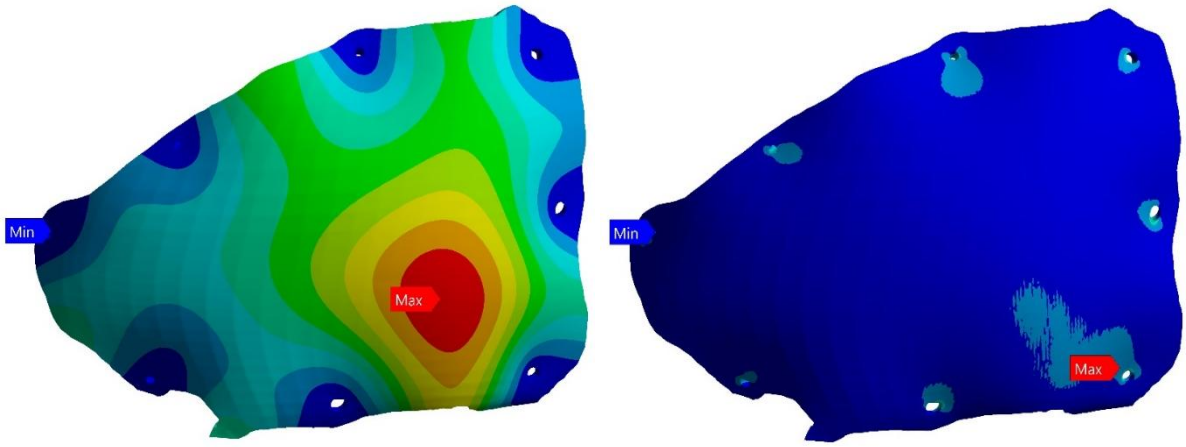

Figure 4.7 PEEK implant deformation and von-Mises stress at minimum load

4.7.1.4 PEEK implant behaviour at maximum load

The 8 fixation points are considered at maximum ICP, the maximum deformation is identified at centre of the implant and minimum deformation at point “A” consequently, the maximum von-Mises stress at point “B” and minimum at edge of the implant as shown in the Figure 4.8.

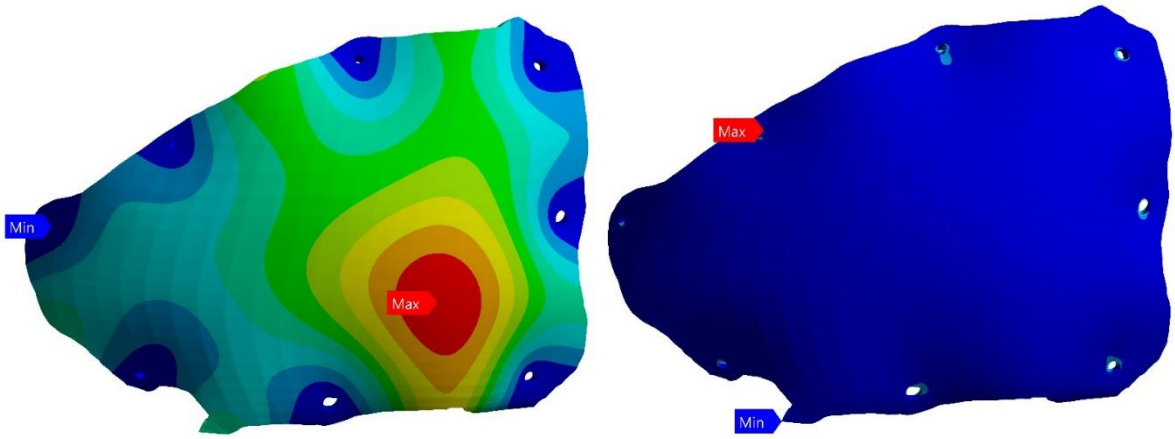

Figure 4.8 PEEK implant deformation and von-Mises stress at maximum load

4.7.1.5 PMMA implant behaviour at minimum load

The 8 fixation points are considered at minimum ICP, then the maximum deformation is identified at centre of the implant and minimum deformation at point “A” consequently, the maximum von-Mises stress at point “F” and minimum at point “A” as shown in Figure 4.9.

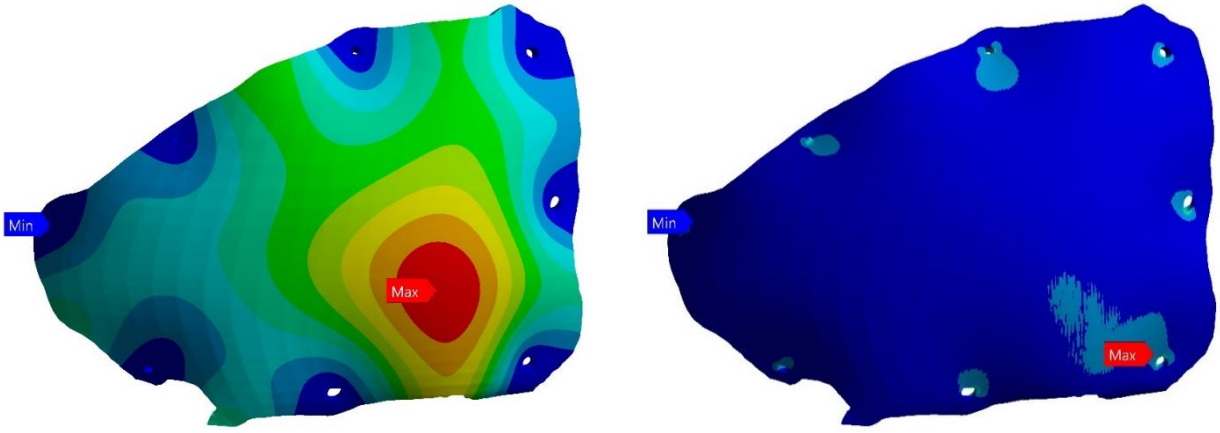

Figure 4.9 PMMA implant deformation and von-Mises stress at minimum load

4.7.1.6 PMMA implant behaviour at maximum load

The 8 fixation points are considered at maximum ICP, the maximum deformation is identified at centre of the implant and minimum deformation at point "A" consequently, the maximum von-Mises stress at point "F" and minimum at point "A" as shown in Figure 4.10.

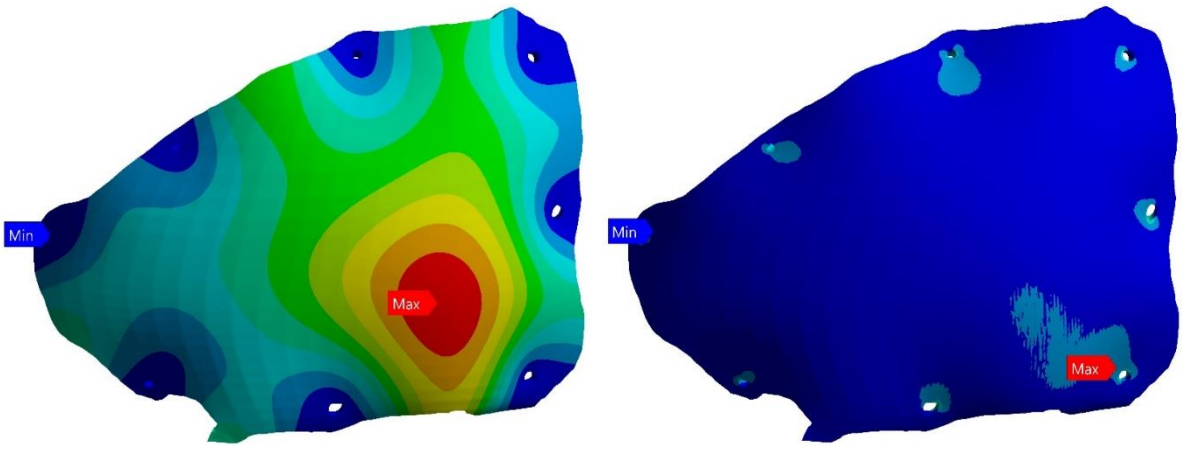

Figure 4.10 PMMA implant deformation and von-Mises stress at maximum load

4.7.2 Case2

It is observed that Ti6Al4V shows low deformation when compared with PEEK and PMMA. The deformation is 2.0499e-5 mm at minimum load and 4.3616e-5 mm at maximum load.

It is observed that PEEK shows minimum equivalent stress when compared with Ti6Al4V and PMMA. The equivalent stress is 0.1801 MPa at minimum load and 0.38319 MPa at maximum load as shown in Table 4.6.

Table 4.6 Deformation and Equivalent stress analysis report for case2 (10 fixation points)

Structural analysis report	**Case2**					
	Titanium alloy (Ti6Al4V)		**Polymethyl methacrylate (PMMA)**		**Polyetheretherketone (PEEK)**	
	Min Load	**Max Load**	**Min Load**	**Max Load**	**Min Load**	**Max Load**
Deformation (mm)	2.05e-05	4.36e-05	7.21e-04	1.53e-03	5.34e-04	1.14e-03
Equivalent stress (von-Mises) MPa	0.19258	0.40974	0.18302	0.38941	0.1801	0.38319

4.7.2.1 Titanium implant behaviour at minimum load

The implant behaviour is depends on boundary conditions such as fixations and intracranial pressure. The 10 fixation points are considered at minimum ICP, then the maximum deformation is identified at centre of the implant and minimum deformation at underneath to the centre of implant consequently, the maximum von-Mises stress at point "B" and minimum at point "A" as shown in Figure 4.11.

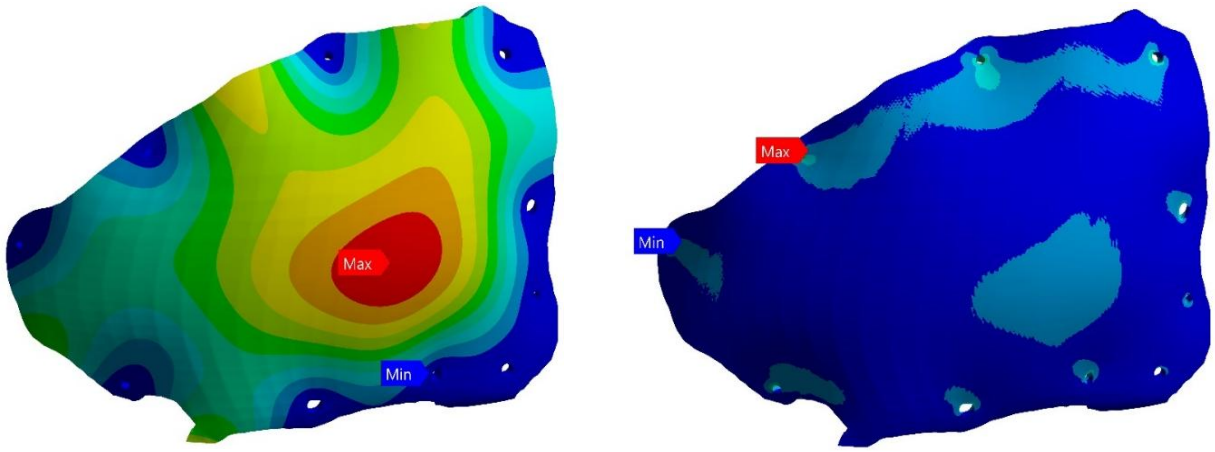

Figure 4.11 Titanium implant deformation and von-Mises stress at minimum load

4.7.2.2 Titanium implant behaviour at maximum load

The 10 fixation points are considered at maximum ICP, then the maximum deformation is identified at centre of the implant and minimum deformation at underneath to the centre of implant consequently, the maximum von-Mises stress at point "B" and minimum at point "A" as shown in Figure 4.12.

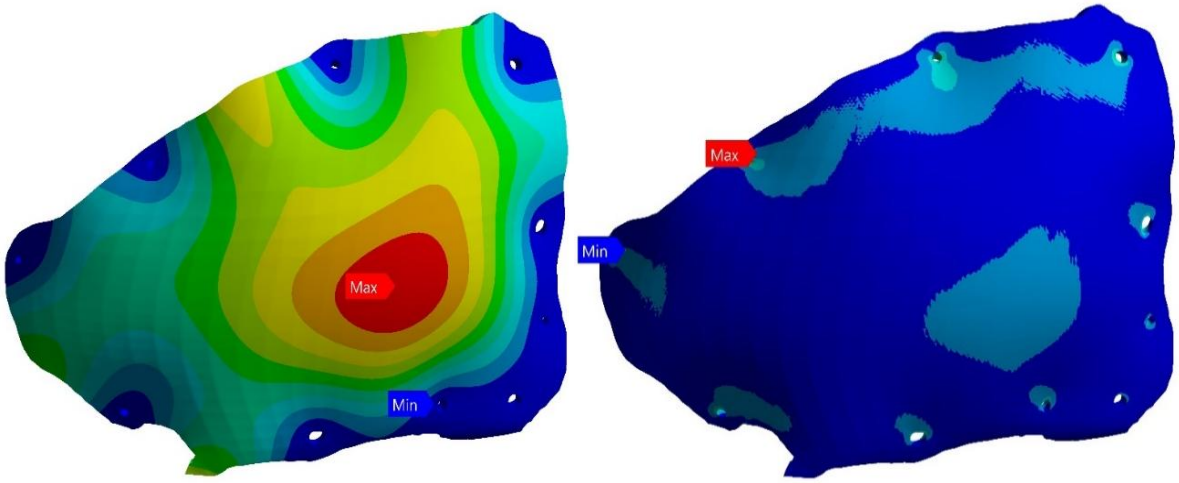

Figure 4.12 Titanium implant deformation and von-Mises stress at maximum load

4.7.2.3 PEEK implant behaviour at minimum load

The 10 fixation points are considered at minimum ICP, then the maximum deformation is identified at centre of the implant and minimum deformation at underneath to the centre of implant consequently, the maximum von-Mises stress at point “C” and minimum at point “A” as shown in Figure 4.13.

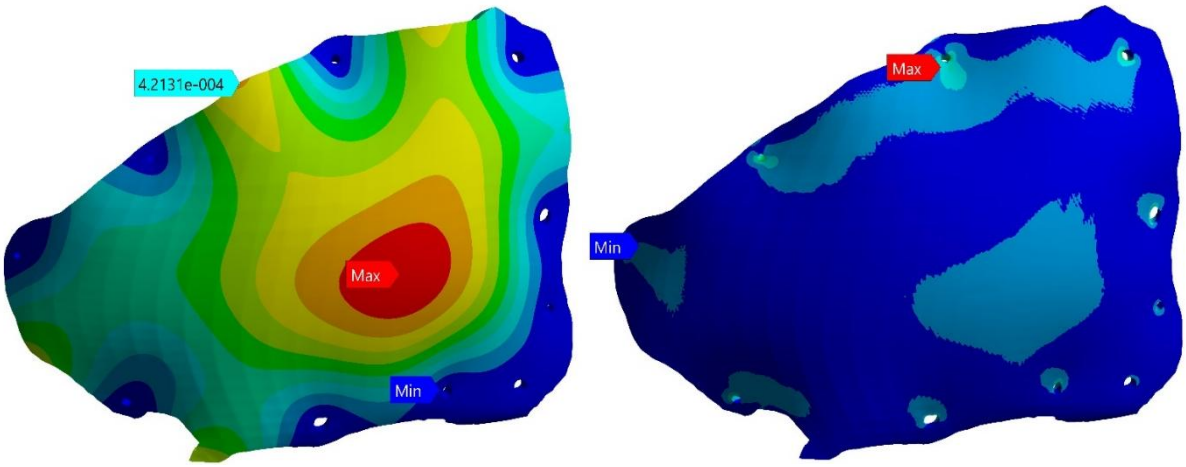

Figure 4.13 PEEK implant deformation and von-Mises stress at minimum load

4.7.2.4 PEEK implant behaviour at maximum load

The 10 fixation points are considered at maximum ICP, then the maximum deformation is identified at centre of the implant and minimum deformation at underneath to the centre of implant consequently, the maximum von-Mises stress at point “C” and minimum at point “A” as shown in Figure 4.14.

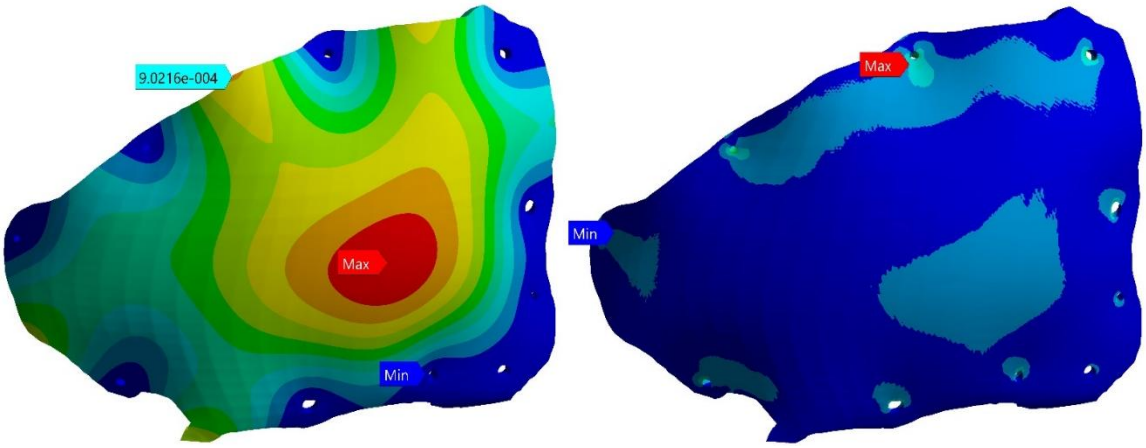

Figure 4.14 PEEK implant deformation and von-Mises stress at maximum load

4.7.2.5 PMMA implant behaviour at minimum load

The 10 fixation points are considered at minimum ICP, then the maximum deformation is identified at centre of the implant and minimum deformation at underneath to the centre of implant consequently, the maximum von-Mises stress at point “B” and minimum at point “A” as shown in Figure 4.15.

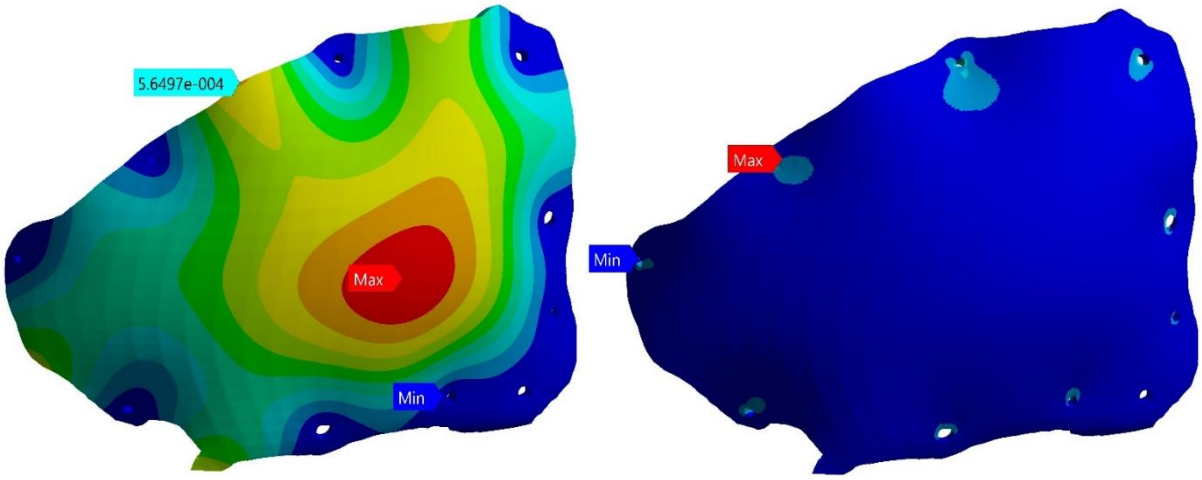

Figure 4.15 PMMA implant deformation and von-Mises stress at minimum load

4.7.2.6 PMMA implant behaviour at maximum load

The 10 fixation points are considered at maximum ICP, then the maximum deformation is identified at centre of the implant and minimum deformation at underneath to the centre of implant consequently, the maximum von-Mises stress at point “C” and minimum at point “A” as shown in Figure 4.16.

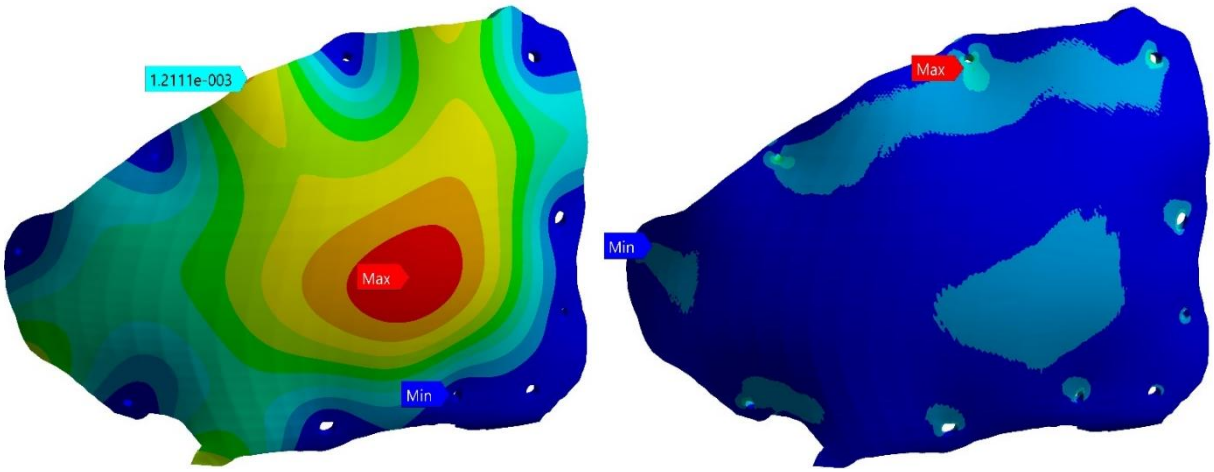

Figure 4.16 PMMA implant deformation and von-Mises stress at maximum load

From Figure 4.17, it is observed that, in both cases the deformation and equivalent stress is increases with increase of intracranial pressure and decreases with increase of fixation points.

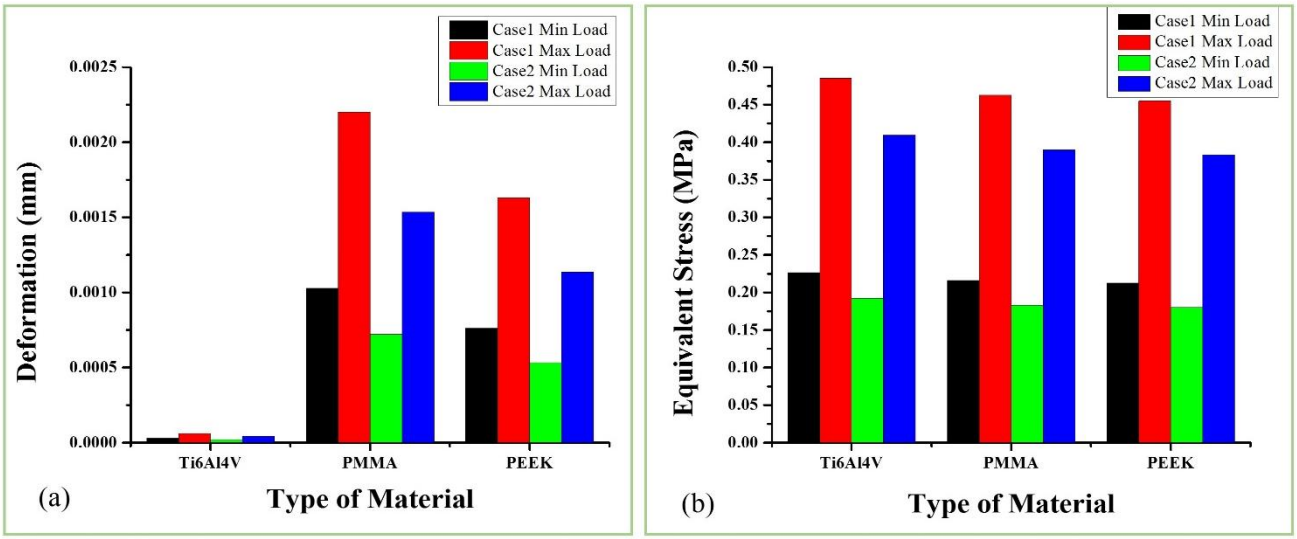

Figure 4.17 a) Deformation values for both cases at maximum and minimum load conditions b) Equivalent stress values for both cases

4.7.3 Observation of polyether ether ketone (PEEK) material at maximum load

Considering case1 at maximum load, the maximum deformation shows in between “E”, “F”, “G” points and stresses were developed near to “A”, “F” points as shown in Figure 4.18.

Considering case2 at maximum load, due to adding of “I” and “J” points, the deformation move towards “B”, “C”, “D” points from “E”, “F”, “G” points and stresses were developed near to “A” and “C” points as shown in Figure 4.18.

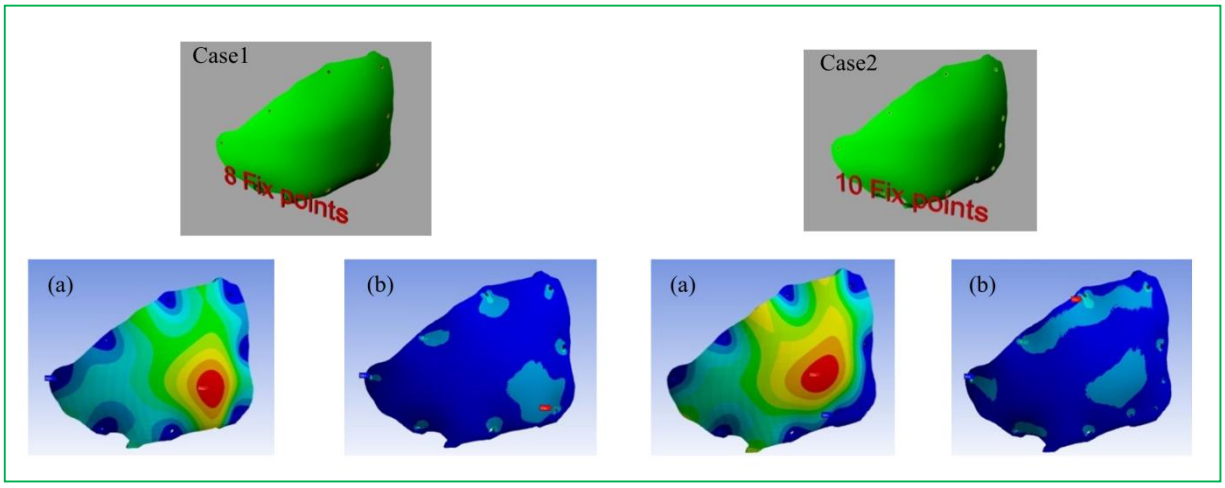

Figure 4.18 Case1 and Case2: a) Deformation at maximum load b) Equivalent stress at maximum load

4.8 Discussion

The finite element study explored the specific role of cranial implant at intracranial pressure conditions through computational simulations. The deformation and equivalent stress are induced in customized PEEK, PMMA and Ti6Al4V implants with respect to ICP and fixation points. A total of 12 fine mesh models were simulated and analysed. The effect of intracranial pressure on the implant at various conditions were studied and fixed at different points to attain stability with respect to skull.

The tetrahedral mesh is generated for STL file with the help of ANSYS 15 software [68], this is used for faster computation, ensures refinement of the mesh wherever necessary and maintain element size wherever possible. The volumetrical change of an implant is observed nearly 3-6% in coarse mesh and it leads to results accuracy, due to this reason fine mesh is selected.

The deformation and stresses are changed with change in ICP and fixation points as shown in Figure 4.23 Case1 and Case2: a) Deformation at maximum load b) Equivalent stress at maximum load. From results, titanium alloy (Ti6Al4V) and polyether ether ketone (PEEK) implants are showing better results. In comparison of both cases, low deformation observed in PEEK material implant and low equivalent stress observed in Ti6Al4V material implant [Table 4.5 & Table 4.6]. PMMA stress values are near to PEEK material.

The stress distribution patterns in the implant with respect to different materials and various pressure conditions are comparable. Higher equivalent stress magnitudes are mainly concentrated at fixation points and deformation magnitudes are concentrated at the centre of PEEK implant as shown in Figure 4.23 Case1 and Case2: a) Deformation at maximum load b) Equivalent stress at maximum load. Considering fixation points, the equivalent stress and deformation magnitudes changing with respect to intracranial pressure.

The reverse engineering technique is used to model the surface body from 3D scanned or STL file, this method is modified and applied to model the implant for beyond mid-line defects with respect to patient specific data. Through this work, the implant cost will be reduce due to Rhinoceros software.

4.9 Conclusion

The modelling of an implant is done in Rhinoceros software with computer-aided reconstruction engineering technique for beyond mid-line deformity and structural analysis was performed

through ANSYS 15 software for Ti6Al4V, PMMA and PEEK materials at minimum and maximum load conditions.

It was observed from the results, the Ti6Al4V shows low deformation and PEEK shows low equivalent stress. However, PEEK ensures better results in all aspects. A much better results can be achieved with implementation of realistic 3D printed model in future.

CHAPTER 5

5. DESIGN AND ANALYSIS OF VARIOUS HOMOGENEOUS INTERCONNECTED SCAFFOLD STRUCTURES FOR TRABECULAR BONE

The main objective of Tissue Engineering is to develop biological substitutes that restore, maintain and improve tissue function. Injure of tissue is occurred due to trauma and congenital diseases, which has to regenerate or replace with suitable tissues or implants. Conventional treatment techniques such as autograft and allograft procedures, which are expensive, complicated and infectious. Therefore, to overwhelm these complications with 3D Printed scaffolds. These scaffolds provide temporary and permanent structural support for cell attachment and tissue regeneration. In this work, homogeneous interconnected scaffold structures were modelled by varying pore-size, porosity, strut cross-section and keeping the same unit cell size. Computational fluid dynamics (CFD) analysis was done for different scaffold structures by considering Darcy's equation to know the permeability of the scaffold with blood properties. Studies were carried out to find out the impact of the design parameters such as porosity, strut cross section, and size on the scaffold functional factor like permeability. Through the ANSYS software, analysis is done to calculate the nature and properties of fluid flow through the scaffold structure. Permeability is calculated using Darcy's permeability equation for incompressible laminar flow equation and was found to be in the range of $4.8\times10^{-9} - 2.3\times10^{-8}$ m^2 for strut cross section of 300 –500 μm. Results showed that strut cross section and porosity were the influencing parameters and play an important role in the scaffold design.

5.1 Introduction

Cancellous bone is also known as spongy or trabecular bone, is one of the two types of bone tissue found in the human body. The trabecular structure is found at the ends of long bones as well as in the pelvic bones, ribs, skull, and the vertebrae in the spinal column. It is very porous and contains red bone marrow, where blood cells are made. It is weaker and easier to fracture than the cortical bone, which makes up the shafts of long bones. Conventional treatment techniques such as autograft (a patient's own tissue) and allograft (tissue from another person) that are used to repair or restore damaged tissues are expensive, complicated and infectious. To overcome these problems 3D Printed scaffolds are developed. Advances in fabrication technologies now enable the strategic design of scaffolds with complex, biomimetic structures and properties. Tissue engineering

scaffold assists as a medium to facilitate cell adhesion and proliferation providing temporary mechanical support to newly grown tissue.

Tissue engineering aims to produce patient-specific biological substitutes to overcome the limitations of conventional clinical therapies. Fabrication of scaffolds using additive manufacturing techniques has more popular advantages like control over the pore size, establishment of homogeneous structures and interconnected pores. Custom-made scaffolds could be developed by appropriate incorporation of a computational model and rapid prototyping (RP) technology. The microstructure of the scaffold determines cell adhesion and tissue vascularization. Properties such as compressive strength (to ensure the mechanical stability of the scaffold structure) and permeability (to ensure the required transportation of nutrients, gases and allow cell proliferation) of scaffolds are considered for successful design of scaffolds. The permeability values of various scaffolds are shown in the Table 5.1.

Table 5.1. Permeability studies from several authors, using different biomaterials, pore sizes and porosities

Authors	**Materials**	**Pore size (avg. µm)**	**Porosity (%)**	**Permeability (m^2)**
Li et al. (2003) [47]	Z-BCP (Biphasic calcium Phosphate)	565	75	0.018×10^{-9}
	D-BCP	300	78	0.10×10^{-9}
	I-BCP	528	60	0.35×10^{-9}
	HA-60	450	60	0.37×10^{-9}
	HA-50 (Hydroxyapatite)	250	50	0.075×10^{-9}
Lee et al. (2006) [48]	PPF: Poly(propylene fumarate)	300	21-26	0.02×10^{-9}-0.09×10^{-9}
		600	38-50	0.55×10^{-9}-1.50×10^{-9}
		900	51-65	1.50×10^{-9}-2.3×10^{-9}
Sanz-herrera et al. (2009) [49]	Bio glass-based foams	510–720	90-95	1.96×10^{-9}
Jeong et al. (2011) [50]	POC : poly(1,8-octanediol–co-citrate)	900	50	0.351×10^{-8}
		900	60	4.74×10^{-8}
Truscello et al (2012) [51]	Titanium alloy (Ti6Al4V)	750	56.7	$0.52\times10^{-9} \pm 3.9\times10^{-12}$
		800	70.5	$1.69\times10^{-9} \pm 1.78\times10^{-10}$
		900	79.6	$3.61\times10^{-9} \pm 8.5\times10^{-10}$

Santamaría et al. (2013) [90]	PLLA scaffold (porogen spheres) weight % is 1-10, 1-15, and 1-18.	Porogen sphere diameter is 100-144	70-94	2.65×10^{-10}- 4.10×10^{-10} 5.29×10^{-10} - 3.25×10^{-10}

Recently computation fluid dynamics was introduced to find the permeability of trabecular bone specimen, the CFD is helps to calculate the flow characteristics along the length of specimen. The CFD helps to eliminate the bench-top testing equipment to know the permeability of specimen and it helps to observe the behaviour of fluid at particular location in specimen [52].

Jeremy et al. 2012 developed a model with appropriate boundary conditions are assigned in CFD software to mimic the experimental setup and testing conditions, the trabecular bone is meshed with the tetrahedral elements convert to solid model [53]. The solid model was imported to Ansys CFX software and defined the boundary conditions as per Darcy's equation. The main boundary conditions are the inlet velocity of fluid i.e. water in m/s and assumed no-slip condition at boundary walls [53].

The present work is addressing the permeability of scaffold structures with various cross-sections such as circular, hexagon and square through CFD analysis. This analysis help to replace the trabecular bone in customized implants.

5.2 Materials and methods

The important or influencing parameters which needs to be considered while designing scaffolds for any bio-medical application which in turn controls important factors like bio-compatibility, bio-degradability, mechanical properties, manufacturing technology and etc. are discussed below.

5.2.1 Pore cross-section

To study the effect of cross-section on permeability with different strut cross-sections such as circular, hexagonal and square.

5.2.2 Pore-size

Scaffolds with a smaller pore size or a higher pore density degraded slower than the scaffolds with a larger pore size or lower pore density (controls the degradation rate) [91]. Temenoff et al. (2000) used pore size in the range 300–500 μm.

5.2.3 Porosity

The complex structure of the pores assists in guiding and promoting new tissue formation. Materials with high porosity [92] enable effective release of biofactors such as proteins, genes, or cells and provide good substrates for nutrient exchange [93].

$$Porosity = 1 - \frac{V_{scaffold}}{V_{Total}} \qquad (1)$$

5.2.4 Unit cell size

Unit cell size of all models was kept uniform to have homogeneity in the dimension.

5.2.5 Surface area to volume ratio

Ratio defines the effectiveness of cell attachment and proliferation. Higher ratio is effective because the surface area available for the cell culture is more.

Table 5.2. Geometrical features of scaffolds chosen for modelling

Strut cross-section	Strut size (mm)	Total unit cell volume (mm^3)	Scaffold volume (mm^3)	Porosity (100%)	Surface area (m^2)
Circular (cir)	0.3	1	0.1738	0.826	2.4878
	0.4	1	0.2865	0.714	3.1662
	0.5	1	0.4122	0.587	3.7692
Hexagonal (hex)	0.3	1	0.1466	0.853	2.3869
	0.4	1	0.2436	0.756	3.0433
	0.5	1	0.3541	0.646	3.6302
Square (squ)	0.3	1	0.2160	0.784	3.0600
	0.4	1	0.3520	0.648	3.8400
	0.5	1	0.5014	0.498	4.5054

5.3 Modelling of scaffolds

The CAD modelling softwares are playing a vital role to develop homogenous scaffold structures with uniform or varibale cross-sections such as circular, pentagon, hexagonal and square etc. In this work, three cross-sections are considered as shown in the Figure 5.1. While considering the hexagon and square the inscribe circle is considered as pore size. The porosity of the scaffold

structure is depends on pore size or strut size (Figure 5.2) of the unit cell. While increasing the pore size the corresponding porosity is decrease as shown in the Table 5.2.

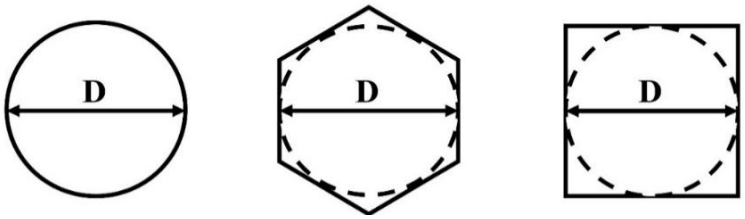

Figure 5.1 Strut cross sections/dimensions

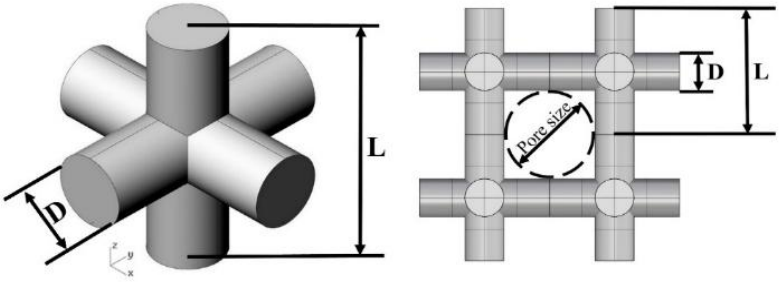

Figure 5.2 Unit cell dimensions

The 3D scaffold structures are developed through repeating the unit cells in x, y, z directions. These repetitive unit cells are unioned to get the required 3D scaffold structures with variable dimensions and cross-sections as shown in Figure 5.2 and Figure 5.3.

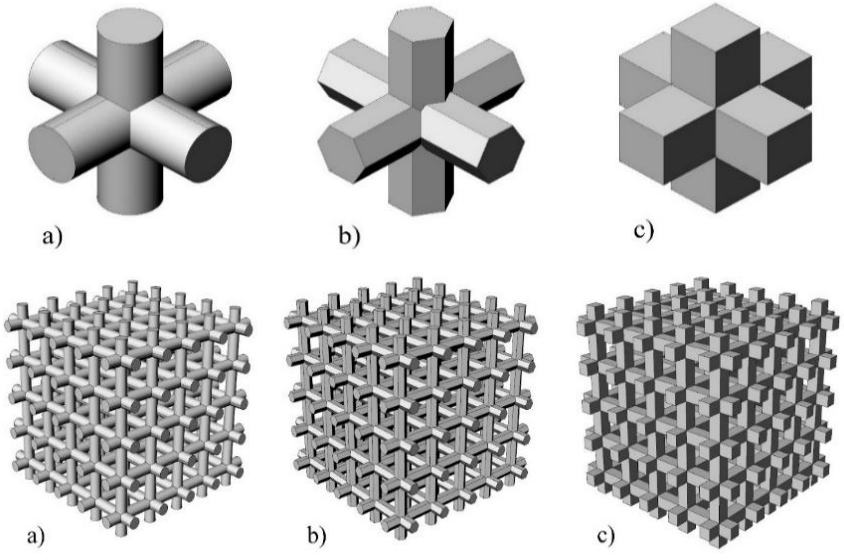

Figure 5.3 Scaffolds a) Circular, b) Hexagonal, c) Square respectively with dimensions 10*10*10 mm^3

5.4 Analysis

The computational methodology helps to find the permeability of various scaffolds structures. The simulation is performed with variable design inputs and analysed the influenced parameters such as porosity, pore size and velocity of the inlet fluid.

5.4.1 Setup

The complete setup for fluid flow analysis with boundary conditions are shown in Figure 5.4. This setup is used to analyse the permeability of scaffold structure. The setup includes inlet, an outlet, a wall and a fluid section. The fluid domain is modelled in CAD software with the dimensions of 40*10*10 mm^3 [90], [94] as shown in the Figure 5.4. The scaffold structure has been subtracted from the domain to get the complete setup for fluent analysis.

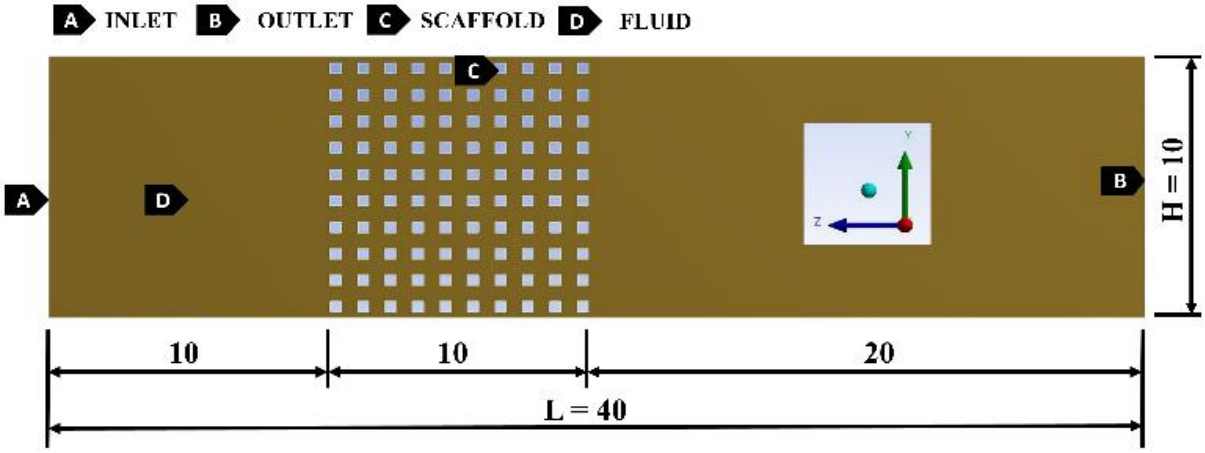

Figure 5.4 Complete setup for fluid flow analysis with boundaries

5.4.2 Computational fluid dynamics (CFD) analysis

Computational fluid dynamics is one of the prominent approach to find the permeability of scaffold. The CFD is depends on finite volume discretization (FVM) approach and it is well known module as ANSYS Fluent. The finite volume discretization is depends on steady sate Navier-stokes equation for incompressible laminar flow, mass and momentum conservation equations. These governing equations are utilized to solve CFD problems, which applies the FVM across the computational domain and discretize the conservation equations. In this study, the convergence criterions is used at 1×10^{-9} for all scaffold structures. This convergence is applied to reduce the initial mass flow residual during the simulation progress [90], [95]. The properties of the fluid considered were similar to that of blood, that is, viscosity of blood is 0.0035 Pa-s and density of blood is 1080 kg/m^3 [96].

The boundary conditions are defined as per literature such as, initial blood velocity at inlet is 0.1 m/s and the zero pressure gauge is considered at the end of scaffold. The channel is in stationary condition, boundary walls are rigid, and No-slip condition is defined between scaffold surface and channel surface. The pressure drop across the scaffold was computed by means of the commercial software package for all models and calculated the permeability.

Darcy equation:

Permeability is a measure of the ability of a fluid medium to flow through it [46].

$$K = \frac{Q\mu L}{A(P_{inlet} - P_{outlet})} \qquad q = \frac{K}{\mu}\nabla P \ \ldots\ldots\ldots\ldots\ldots\ldots (2)$$

q = Q/A = Discharge per unit area, with units of length per time (m/s)

$\nabla P = (Pinlet - Poutlet)$ / L = Pressure gradient vector (Pa/s)

Q is the volumetric flow rate (m^3/s), ΔP is the pressure drop, A and L are the cross-sectional area (m^2) and the length of the porous material (m), respectively, and μ is the dynamic viscosity of the fluid (Pa-s or N-s/m^2) [94].

5.5 Results

The streamline velocity profiles of fluid particles flowing through the scaffold along with the inlet, outlet, and fluid wall is shown in Figure 5.5. Here, fluid is assumed to undergo a laminar steady flow and is incompressible. The variation of pressure or pressure gradient generated due to the abstraction in flow medium can be observed from Figure 5.6. This is due to the introduction of

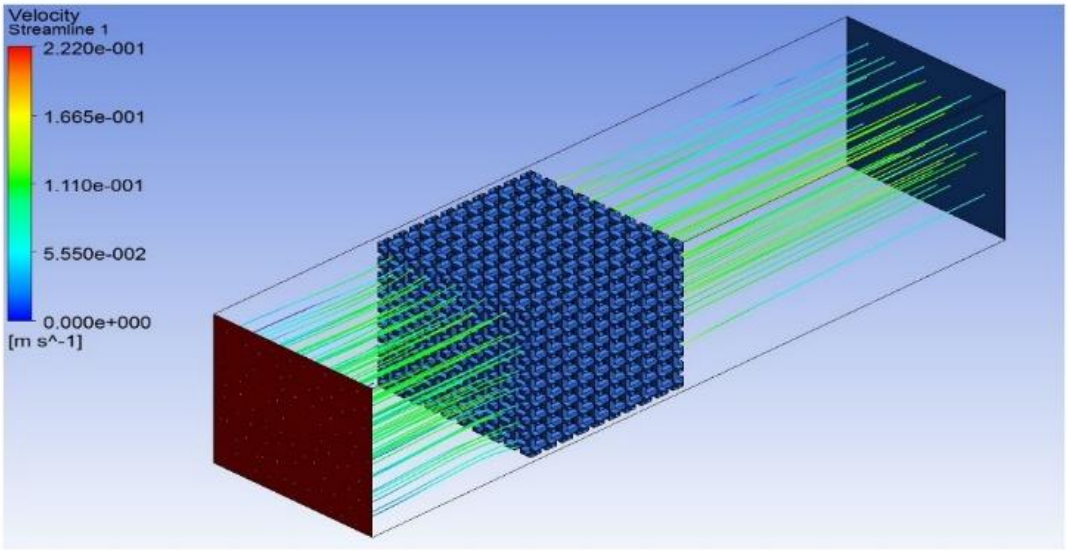

Figure 5.5 Variation of streamline velocity along scaffold

scaffold in the fluid medium to find out its permeability by measuring the pressure gradient across it.

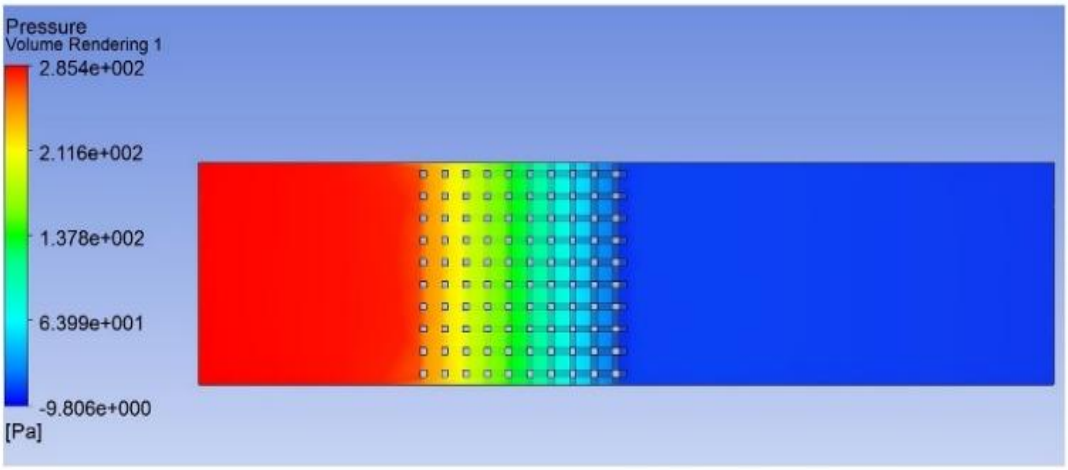

Figure 5.6 Variation of pressure of fluid flowing through scaffold

Darcy's equation is used to calculate the permeability of the scaffold. The process of measuring the pressure gradient repeated for various specimens and results is plotted for the pressure gradient versus the strut size which is reported in Figure 5.7.

Permeability of the scaffold depends on the size, shape, architecture and porosity of the medium in which the fluid is flowing. In our analysis, size and shape of the strut has been varied to study the intrinsic permeability of the scaffold structure. Results showed that as we increase the strut size of the scaffolds, the intrinsic permeability of the scaffolds has decreased which is shown in Figure 5.8. Since size of the scaffold structure is kept constant, increase in the strut size leads to decrease of the pore size. This shows that as we increase the pore size, porosity of the structure

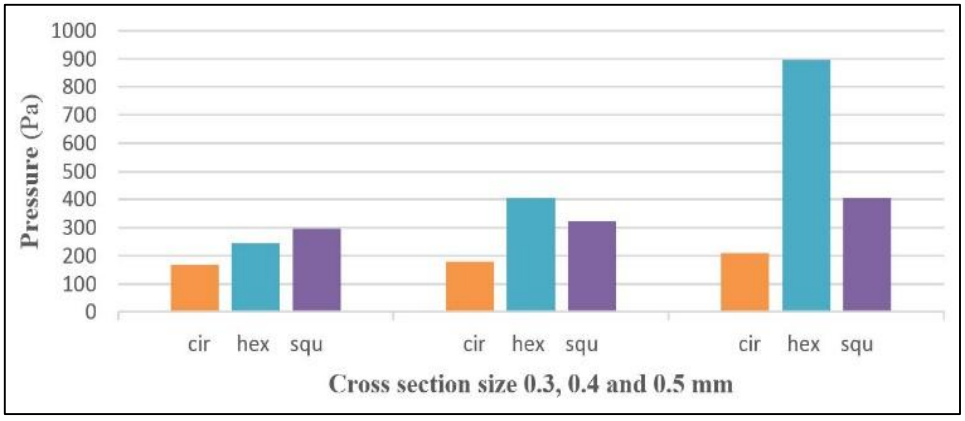

Figure 5.7 Graph showing pressure difference for scaffold structure with different cross-section

increases. This leads to the increase in intrinsic permeability of the scaffold which is shown in Figures 5.8 and 5.9.

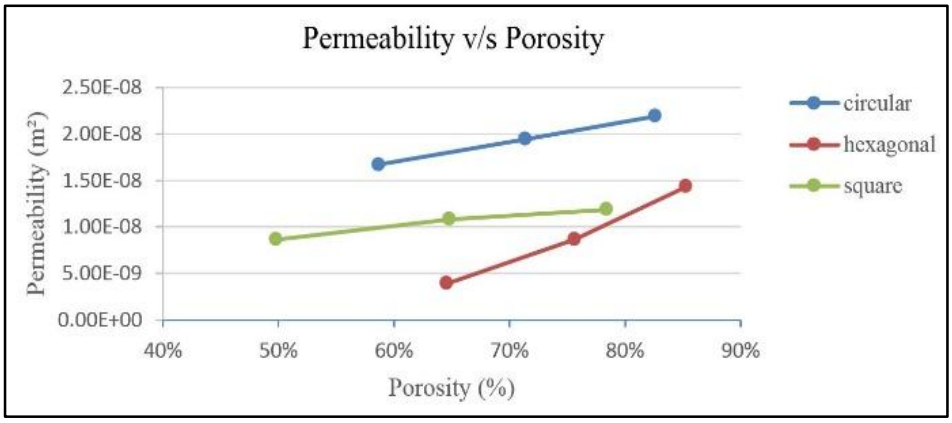

Figure 5.8 Graph showing effect of porosity on permeability

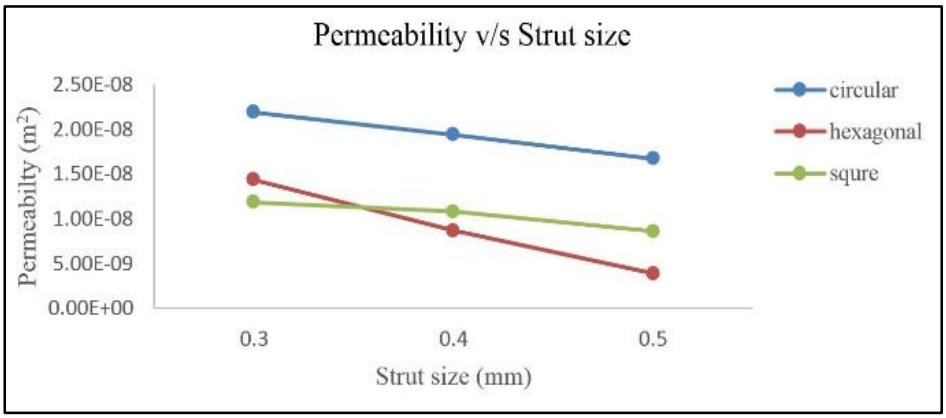

Figure 5.9 Graph showing variation of permeability vs strut size

5.6 Discussion

The design of the scaffold for tissue engineering applications, essentially for the trabecular bone is a complex problem that depends on many parameters and constraints. In this paper, scaffold structures were designed by considering parameters such as porosity, strut cross section, strut size which controls the pore size and by maintaining the same domain for all the designs. The main objective of the research work was to have homogeneous interconnected pores. This was achieved using modelling of scaffold structure by a unit cell-based approach. Here, parameters such as strut size and strut cross section were varied keeping the unit cell size same.

A total of nine variant specimens were modelled by changing the cross sections (circular, hexagonal, and cubic), strut size (0.3, 0.4, and 0.5 mm), and keeping the unit cell dimensions

constant for all models. The computational studies were carried out using a software tool to find out the mechanical stability and permeability of the specimens designed.

Permeability of the designed scaffolds was found to be in the range of 4.8×10^{-9} m^2 – 2.3×10^{-8} m^2 for circular, cubic, and hexagonal cross sections, where the hexagonal cross section shows comparatively less permeability and the circular one shows high permeability, and the cubical cross section has intermediate permeability. The obtained results were matched with the available resources [95].

5.7 Conclusion

In this paper, the design of a homogeneous interconnected scaffold structure for cancellous bone is carried out. The geometry of the scaffold structure is simplified using regular and homogeneous distribution of pores. The effect of the strut cross-section, pore size on the pressure variation, and the magnitude of velocity is studied. From the literature, the trabecular (cancellous) bone pore size ranges from 300 to 500 µm, so the strut size is maintained to be in this range which directly controls the pore size.

Computational fluid dynamical analysis shows the effect of porosity, pore size, cross section, and other geometrical parameters which are not considered in this study on the pressure in the scaffold, velocity, and shear stress. Permeability is the important design parameter to consider because it determines many functions of scaffolds like the transportation of gas, nutrients, and fluids. Designing a scaffold, keeping permeability as a design factor, will also encompass the effect of pore size and distribution. Cross section of the pore also affects the permeability of the scaffold structure. Results show that scaffolds with circular cross sections have higher permeability of 4.8×10^{-9} – 2.3×10^{-8} m^2 for the pore size of 300 – 500 µm, respectively. Whereas, scaffolds with hexagonal cross sections have comparatively less permeability and cubical cross-sections have the permeability intermediate between circular and cubical cross sections. The results obtained are acceptable, since they match with the permeability obtained through computational and experimental analysis in the literature [96]. This approach is based on Darcy's law and this study gives importance to geometric parameters on the permeability and other parameters where it eliminates the use of time-consuming experiments. This justifies that the method followed is valid and the designs can be used for further stages like in vitro and in vivo studies, implantation, and so forth.

CHAPTER 6

6. HOMOGENOUS SCAFFOLD BASED CRANIAL IMPLANT MODELLING AND ANALYSIS – UNIT CELL ALGORITHM – MESHLESS APPROACH

This computational study explores, a unique modelling approach of the cranial implant, homogenous scaffold algorithm, and meshless method respectively. This modelling methodology is the easiest one and addressing both the symmetrical and asymmetrical defects. The implant is embedded in a unit cell based porous structure with the help of an algorithm, and this algorithm is simple to manage the consistency in porosity and pore size of the scaffold. Totally six types of implants are modelled with variation in porosity and replicate the original cranial bone. Among six implants, Type 2 (porosity 82.62%) and Type 5 (porosity 45.73%) implants are analysed with the meshless approach under ICP. The Total deformation and Equivalent stress (von-Mises stress) of porous implants are compared with the solid implant under same ICP conditions. Consequently, distinctive materials are used for structural analysis such as titanium alloy (Ti6Al4V) and polyether ether ketone (PEEK) respectively.

6.1 Introduction

Cranial implants have experienced a significant evolution in the last decade in different aspects such as the type of materials and method of manufacture. Besides, the patient-specific cranial implants have been recently developed. Cranioplasty deals [12] with the treatment of skull injuries and defects with an established surgical procedures. The main aim of these procedures is to restore the protective function of the skull and cranial aesthetics. To date various materials have been used for the treatment of cranial defects such as titanium alloy (Ti6Al4V) and polyether ether ketone (PEEK) [30], [68]. However, these materials are biocompatible, successfully implanted for skull and femur bone injuries. The PEEK is successfully implanted in Mexico for an oncology patient [81].

Most of the customized cranial implants are fabricated based on patient specific data, and this data is in Digital Imaging and Communications in Medicine (DICOM) format obtained from Computed Tomography (CT) and Magnetic Resonance (MRI) [12], [82]. The acquired image data sets are processed and subsequently converted into Standard Tessellation Language (STL) file formats which are required for 3D printing. The medical imaging techniques, with the help of Computer

Aided Design and Manufacturing technologies (CAD/CAM) offers new possibilities for fabrication of patient-specific (titanium and PEEK) implants with 3D printing technology [67], [78].

Anatomically the skull is the symmetrical part for many humans. The skull injuries are categorized into symmetrical and asymmetrical defects. In symmetrical defect, the malformation portion can be planned with contralateral side of the skull through Computer Aided Modelling software [12]. Modelling of an implant for asymmetrical defects is quite challenging because mirroring of contralateral side of the skull cannot be possible. These defects deals with multi-point deformities and beyond midline deformities [97].

The complexity of reconstruction of these defects mainly depends on the distorted area of the skull in cm^2 and where the defect crosses the midline of the skull (i.e. sagittal plane). If these defects are less than 5 cm^2 almost flat surface, therefore, they are considered as small defects, whereas large defects require a more curved implant [33].

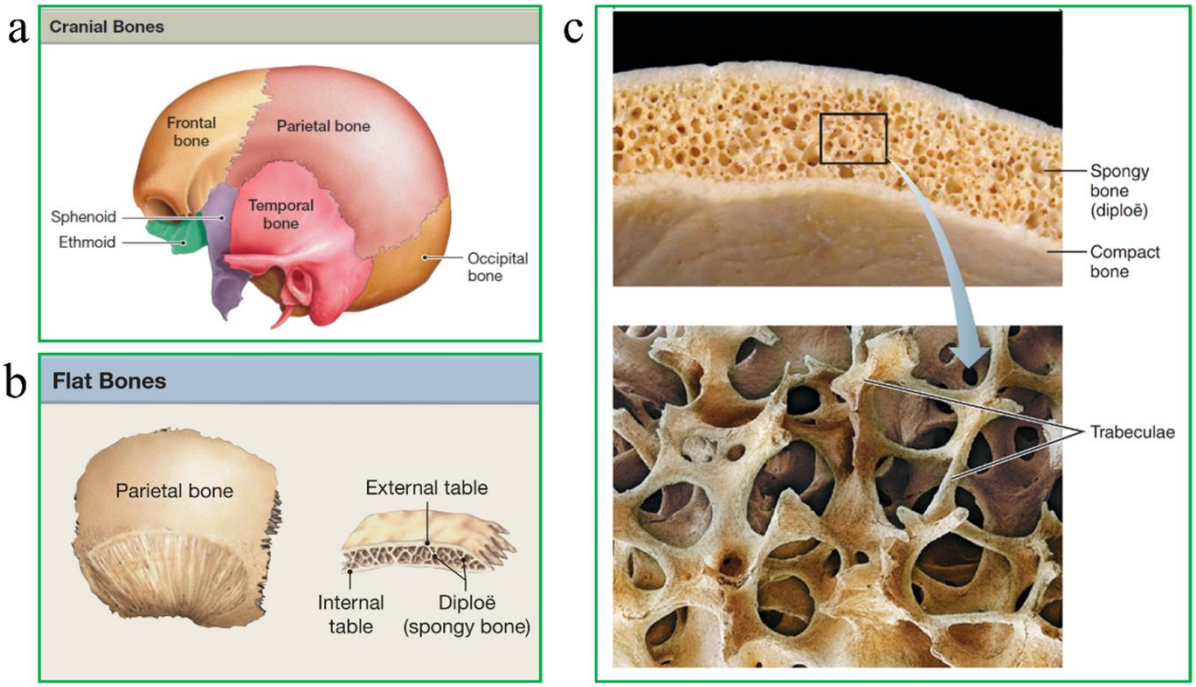

Figure 6.1 a) Cranial bones of the skull b) The flat bones composed of cortical bones and spongy/trabecular bone c) Microscopic view of dipole

The skull contains cranial and facial bones [1], [37]. The cranium surrounds and protects the brain. It consists of the occipital, parietal, frontal, temporal, etc. (Figure 6.1a and 6.1b). Among these parietal, frontal and occipital are flat bones. A flat bone replicates a reinforced sandwich structure.

However, this flat bone having thick layers of compact bone are called the internal and external tables or cortical bones, and spongy bone between the tables is known as the dipole (Figure 6.1c). This spongy bone also called trabecular bone (scaffold structure), and the open spaces between trabecular bones are filled with red or yellow bone marrow.

The human parietal bone is observed in micro-CT and defined the data of inner cortical bone thickness, outer cortical bone thickness, dipole thickness and porosities are 0.35 mm, 0.76 mm, 5.08 mm and 39% to 42% [39], [98], . Respectively, the dipole thickness and porosities are varied with patient age and sex [75], [76].

In Tissue Engineering (TE), the 1) optimum porosity 2) high pore interconnectivity 3) pore size distribution 4) permeability 5) biocompatibility 4) mechanical properties defines the quality of scaffold and replicates the connective tissue [93], [99]. Among these, the porosity and pore size are the key components in bone regeneration.

The computer aided modelling and 3D printing techniques plays a vital role to fabricate the scaffold with highly interconnected pore structure (Homogenous and Non-Homogeneous architectures). While the cranial implants are successfully implanted in rabbit and mouse [100]–[102] with 100 μm to 600 μm pore size and 40% to 90% porosity. The optimum pore size and porosity for bone ingrowth cannot be definitively specified at present, and it's still varying. While increase in the pore size and porosity, the bone ingrowth also increases, however mechanical strength is varied with internal scaffold structure. Recently unit cell approach has proven best alternative to model scaffold structures.

The pressure inside the cranial cavity is called intracranial pressure (ICP). It varies with age, body position and affects the cranial implant after surgery. The standard range of ICP is 7-15 mm of Hg for an adult human being [2], [85]. The cranial implant supported by the surrounding skull with fixation points. These fixation points are selected randomly by the surgeon observing implant shape and damaged portion of the skull.

Recently, the meshless methodologies are playing a vital role to simulate the human bones (CT scanned parts) without using traditional finite element meshing. This method can be employed to assess the Total deformation and Equivalent stress of the implant under ICP loading conditions. This meshless approach is a Solution Structure Method (SSM) [69]–[71], and recently implemented in Rhinoceros software as Scan & Solve plugin [103], [104].

The aim of this study is to model homogenous scaffold based cranial implant for both symmetrical and asymmetrical defects through unit cell algorithm and FCN technique. Finally, the meshless method is used to investigate the Total deformation and Equivalent stress (von-Mises stress) of the implant at various ICP conditions with respect to fixation points.

6.2 Computer aided modelling method

Most frequently used cranial implants are solid type. The evolution of these implants have been done in many directions, mainly such as 1) Type of material of an implant 2) Scaffold/porous implants leads to Osseo integration 3) 3D printing techniques are used to print the implant. The complete modelling of an implant is presented in this paper followed by four aspects such as Firstly, the novel methodology was developed to model an implant for both symmetrical and asymmetrical defects. Secondly, introducing unit cell based scaffold structure for an implant by the algorithmic approach, which mimicking the original skull structure (dipole) and to help for Osseo integration. Thirdly, analysing the implant structurally under intracranial pressure conditions to determine the Total deformation and Equivalent stress with the help of meshless method.

6.2.1 Modelling of an implant

The DICOM images are processed in MIMICS software to get mesh model of the skull in Stereolithography format (STL) and data is imported to Rhinoceros software. This software has many advantages to model complicated designs like automobile components, jewellery design and handle the STL file with different CAD operations such as Boolean and trim, etc. From STL file observation, the skull is damaged at the parietal bone and frontal portion. The parietal bone portion can be treated as the symmetrical defect and frontal bone portion treated as the asymmetrical defect. The symmetrical defects implant is modelled by mirroring the contralateral side portion of the skull. However, this mirroring technique partially deals with asymmetrical defect.

6.2.2 Free form closed curve network (FCN)

This novel methodology is used to model an implant for both symmetrical and asymmetrical defects. The procedure follows as a free form closed curve network is drawn on the skull surface, and it covers the entire damage portion (yellow colour line). With this curve network, a Non-Uniform Rotational B-spline (NURBS) surface patch [12], [82] (Figure 6.2a and 6.22b) is generated by defining the control points in U, V directions. While increasing the controlling points, the degree of controllability of surface patch is also increased. Respectively adjusting these

controlling points is quite complex. The symmetrical defect (i.e. parietal bone) surface patch is modelled by 8 control points (Figure 6.2c (i)) and asymmetrical defect (i.e. frontal bone) is modelled by 13 control points in U and V directions (Figure 6.2c (ii)). Defining number of control points are purely based on the complexity of defect and the designer. However, the modelled NURBS patch should replicate the original skull surface.

This surface patch is subtracted from the skull by using Boolean operation and trimming the edges (Figure 6.2a (iii) and 6.2b (iii)) for proper fitting concerning damaged portion. The final patch is extruded longitudinally at a length of 6 mm. While to increase the accuracy of fitting, the implant

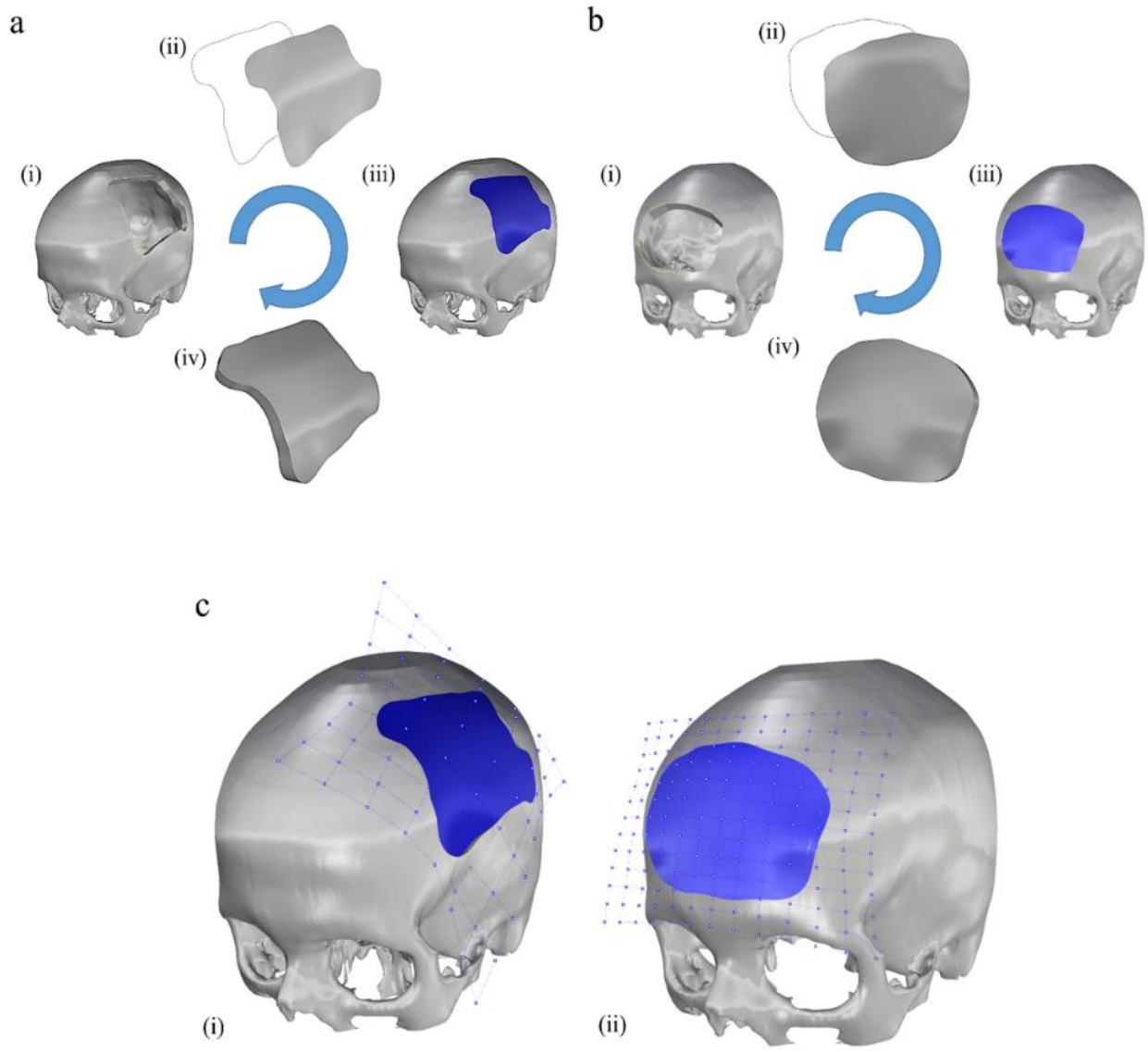

Figure 6.2 a) Modelling of an implant for symmetrical defect (parietal bone) b) Modelling of an implant for asymmetrical defect (frontal bone) c) Adjusting U, V points on NURBS surface

edges are chamfered at 30-35 degrees (Figure 6.2a (iv) and 6.2b (iv)). Finally, the solid implant model was developed and it needs to be embedded with scaffold/porous structure.

6.3 Introducing homogenous scaffold for the implant

6.3.1 Unit cell

CAD software is utilized to model 3D scaffold geometries with variable pore size (Figure 6.3a) [56] and porosity by using different unit cell topologies such as Grid or cubic, X, Star, Octet, BCC, FCC, etc. The porosity defines the relationship between the volume of scaffold and the apparent volume (Bounding volume of the scaffold). However, the porosity is influenced by varying the strut diameter [105].

The porosity is varying from "0" to "100%". The nearly "0" value refers scaffold is denser (solid) whereas almost "100%" indicates highly porous in nature. In this paper, totally six type of scaffolds are designed (Figure 6.3b) considering total volume of unit cell as 1 mm^3 and strut diameter varying from 200 µm (0.2 mm) to 700 µm (0.7 mm) (Table 1).

D = strut diameter in µm or mm, L = strut length in mm

Table 6.1 The pore size and porosity of various scaffold structures

S. No	Scaffold type	D = Strut diameter (mm)	Pore size (µm)	V_{Bone} = Bone volume of unit cell (mm^3)	V_{Total} = Total volume of unit cell (mm^3)	Porosity
1	Type 1	0.2	800	0.0829	1.00	91.71
2	**Type 2**	0.3	700	0.1738	1.00	**82.62**
3	Type 3	0.4	600	0.2864	1.00	71.36
4	Type 4	0.5	500	0.4122	1.00	58.78
5	**Type 5**	0.6	400	0.5427	1.00	**45.73**
6	Type 6	0.7	300	0.6694	1.00	33.06

For CAD models, porosity can be calculated as [105]

$$Porosity(\phi) = \left[1 - \frac{V_{Bone}}{V_{Total}}\right] \times 100\% \qquad (3)$$

Therefore V_{Bone}= Volume of scaffold and V_{Total} = Total or bounding volume of the unit cell (i.e. apparent volume of unit cell).

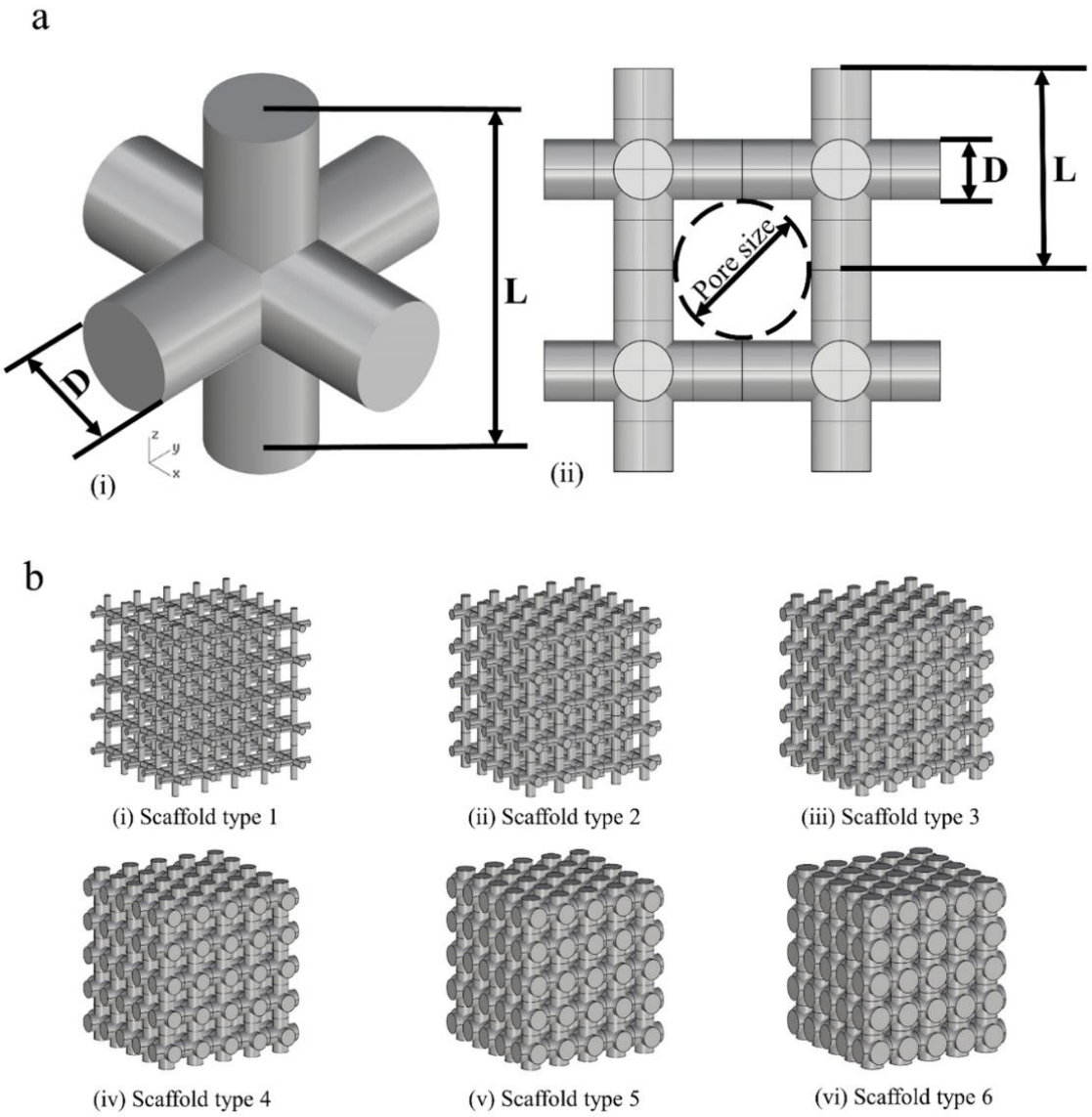

Figure 6.3 a) Unit cell details b) Various scaffold structures based on porosity and pore size

6.3.2 Algorithm

The Rhinoceros software is associated with grasshopper plugin, which is an algorithmic based approach used to facilitate computer aided geometries such as homogenous/heterogeneous scaffold structures with controlled or variable pore size and porosity.

The FCC (face centred cubic) structure have six face atoms (orange colour) and six corner atoms (blue colour) (Figure 6.4). The face atoms are considered to construct the unit cell, which are

connected by lines. These lines are used to model the strut with variable diameters, while varying the strut diameter leads to change in porosity of the unit cell. The advantage of the simple cubic unit cell, strut area cannot share with neighbour unit cells, and typically single unit cell porosity resembles total body porosity.

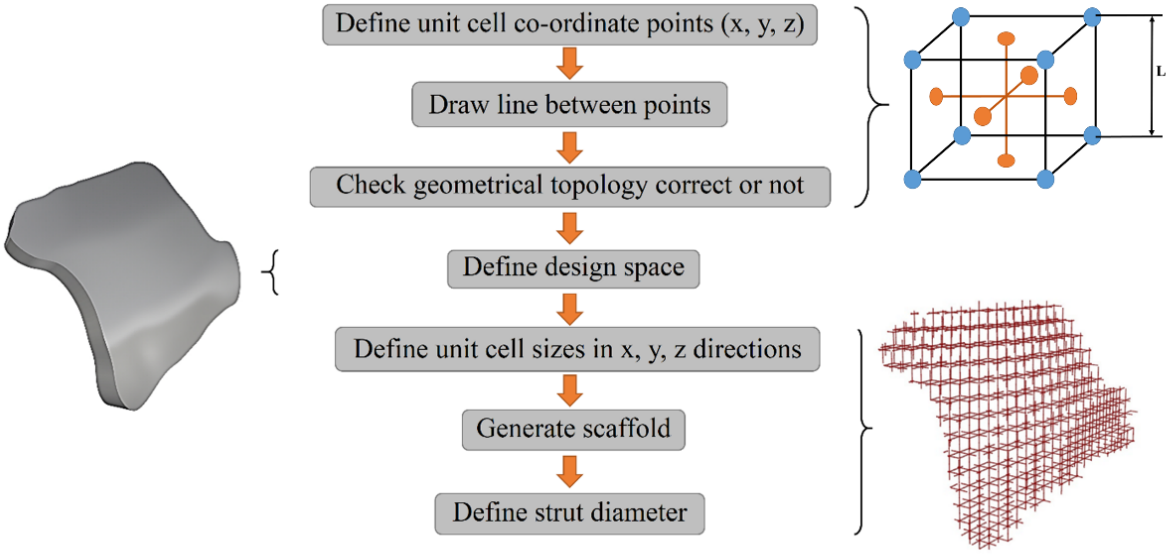

Figure 6.4 Algorithm for modelling of an implant with variable porosity

The modelled unit cell geometrical topology [3] should be correct enough to connect with respective unit cells to generate the scaffold structure as per design space. These unit cell sizes can be varied about X, Y, Z directions and can be manually controlled. In this work, the unit cell size volume (L*L*L in mm) is fixed in all directions (as 1 mm^3).

After defining cell size, six types of scaffold structures are modelled by varying strut diameters such as 0.2 mm, 0.3 mm, 0.4 mm, 0.5 mm and 0.6 mm correspondingly the porosity decreased as 91.71%, 82.62%, 71.36%, 58.78% and 45.73% as shown in Table 6.1.

6.3.2.1 Steps involved in algorithm

6.3.2.1.1 FCC unit cell

The Face centred cube is having 6 faces such as ABCD, HEFG, CDFG, BEHA, BEFD and AHGC. The face atoms are I, J, Q, P, N, and M and the corner atoms are A, B, C, D, E, F, G and H. From the centre point “o”, the line is connected to face atoms to get required skeleton of unit cell as shown in Figure 6.5.

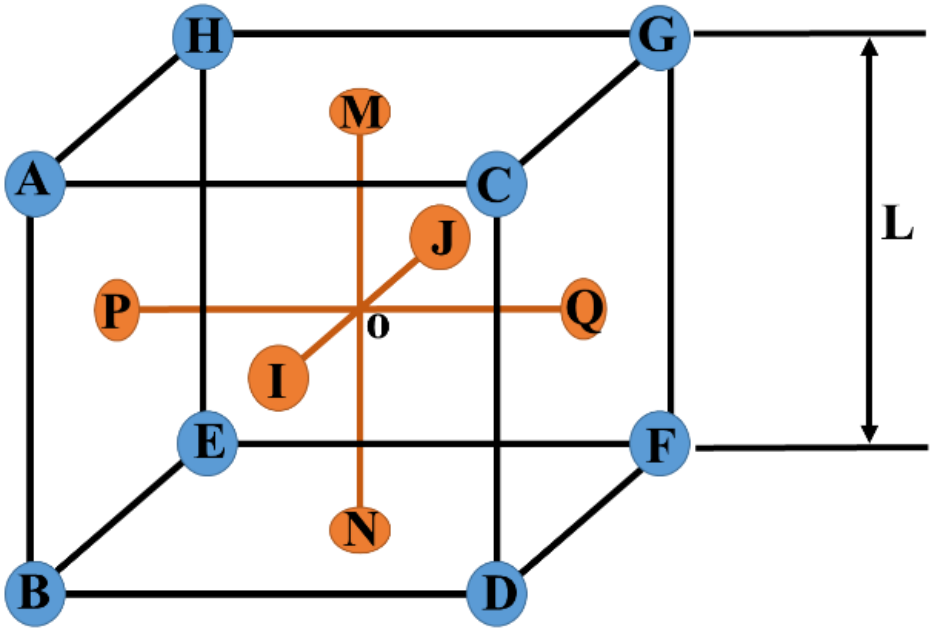

Figure 6.5 Unit cell skeleton

6.3.2.1.2 Unit cell coordinates

The unit cell coordinates are through six face points such as

I = (0.5, 0, 0.5), J = (0.5, 1, 0.5)

Q = (1, 0.5, 0.5), P = (0, 0.5, 0.5)

N = (0.5, 0.5, 0), M = (0.5, 0.5, 1) all are in mm

The six face points are opposite to each other and these are connected by lines from I to J, Q to P and N to M. These lines are combined to form a single unit cell as show in Figure 6.6.

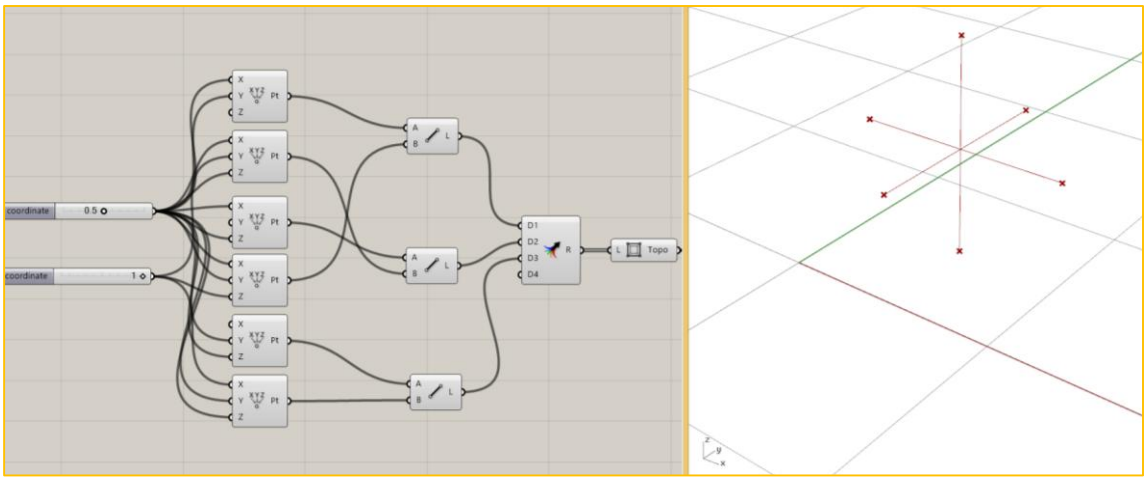

Figure 6.6 Modelling of FCC unit cell skeleton

6.3.2.1.3 Various unit cell configurations

Various type of unit cell configurations were developed from FCC unit cell points such as X-type, Grid or Cubic type etc. The X-type unit cell is designed through connecting the corner points of the cube AF, HD, GB, and CE and these lines are intersect at origin "o". The Grid or Cubic type unit cell is designed through connecting the edges of cube AH, AB, HG, HE, GC, GF, CA, CD and BE, EF, FD, DB. The combination of cubic and X type unit cells form new type of unit cell (Figure 6.7).

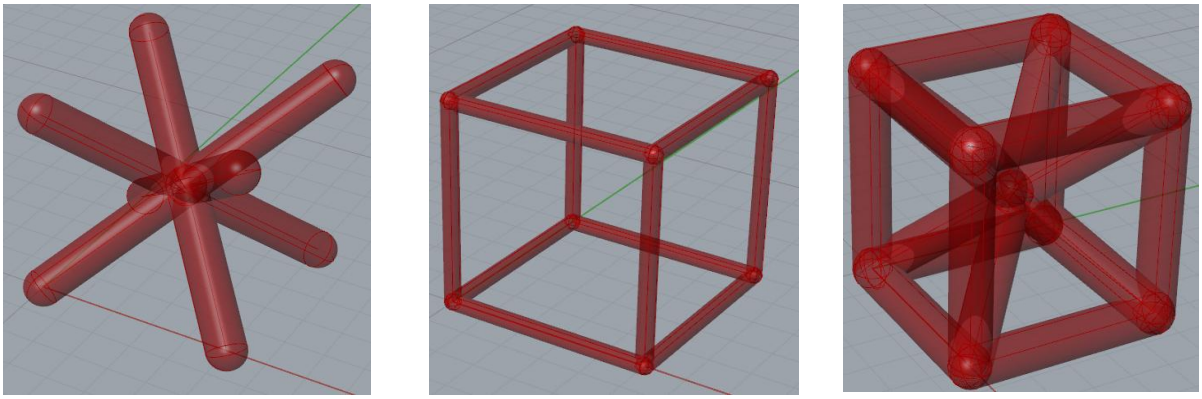

Figure 6.7 Various unit cell confirmations a) X-type b) Grid c) Combination of X and Grid

6.3.2.1.4 Geometric topology and design space

In mathematics, geometric topology is the study of manifolds and maps between them, particularly embedding of one manifold into another. The scaffold is embedding of unit cells in X, Y and Z directions. The topology is playing key role in the scaffold structures, whenever this topology is not correct the corresponding scaffold is generated with unequal dimensions.

The design space is the required space to fill with unit cells, which has taken place in different ways such as

1) Method I: Perform the Boolean operation between design space and scaffold.
2) Method II: Divide the surface in U, V directions and fill with the unit cells at each point.
3) Method III: Sectioned the implant in particular axis and fill the unit cell at each sectioned surface.

Method I: Boolean operation

Create the unit cell scaffold through array operation i.e. fill the single unit cell in X, Y, Z directions with defined number. The design space is enclosed with scaffold and done the Boolean operation

i.e. intersection operation was used to produce common area of design space and scaffold as shown in Figure 6.8. This is easiest method to model scaffold with specified shape or region.

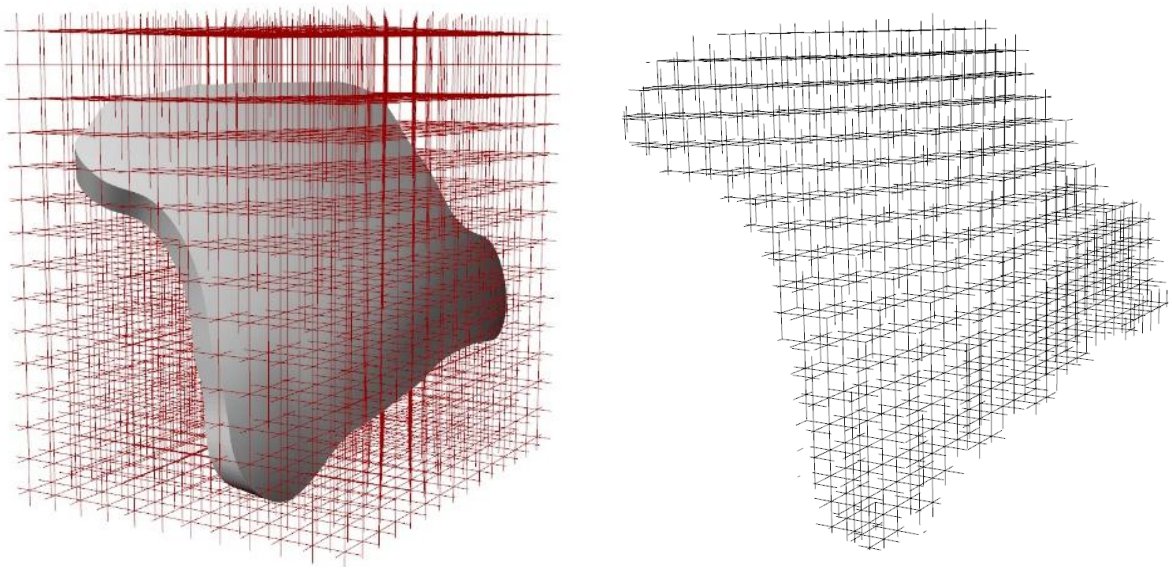

Figure 6.8 Generating scaffold through boolean operation

Method II: Divide the surface in U, V directions

The surface was divided in U, V directions and defined the custom points which depends up on user. Subsequently, few more points were added in between the surface through offset operation as shown in Figure 6.9. The each and every point has considered as origin of the unit cell and

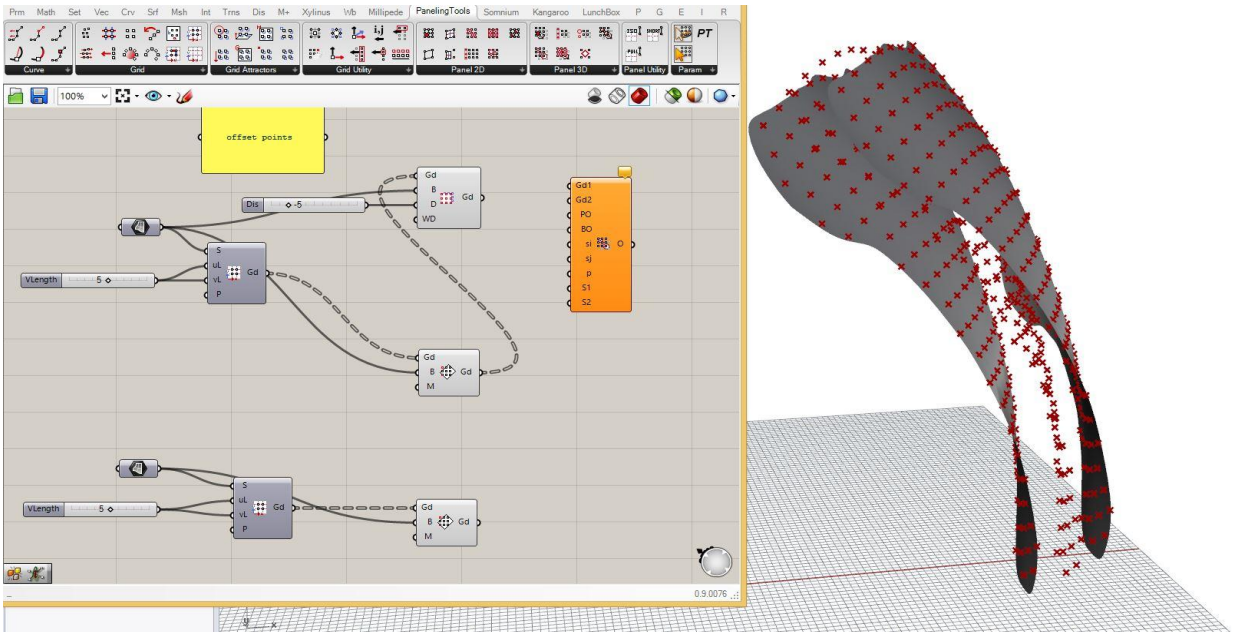

Figure 6.9 Generating scaffold through surface points

developed the required scaffold. Whenever, the distance between the points is not mentioned properly the Boolean of the unit cells is difficult and unable to model the required porous implant.

Method III

The design space was sectioned layer by layer in z-axis. This sectioned layer was displayed as black colour as shown in Figure 6.10. The each sectioned layer was filled with points in uniform spacing in x, y directions. The each point was considered as origin of unit cell and modelled the final scaffold.

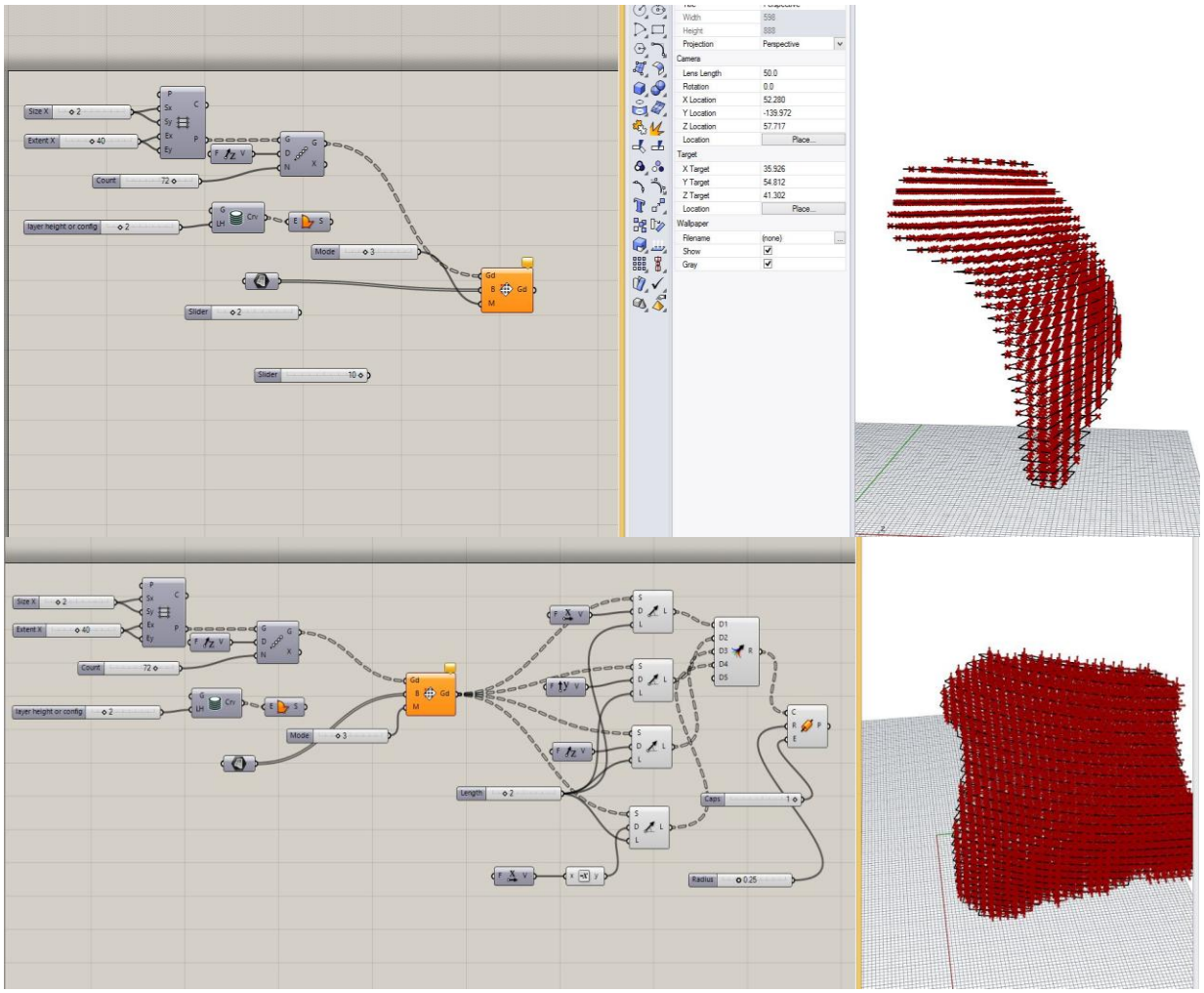

Figure 6.10 Generating scaffold through points at each section in Z-axis direction

6.3.3 Final implant

The design space is converted into scaffold structure with the help of algorithm. Two surfaces are extracted from the design space and are extruded longitudinally at a distance of 0.76 mm for outer surface and 0.35 mm for inner surface. These extruded surfaces replicates the outer cortical and inner cortical bones. Finally, the scaffold structure and extruded surfaces are union by Boolean

operation as shown in Figure 6.11a. The developed model has mimicked the original skull (i.e. parietal bone), and also reduced the weight of the implant. Totally, six combinations are modelled with varying pore sizes and porosity (Figure 6.11b). The final implant specifications are shown in Table 6.2.

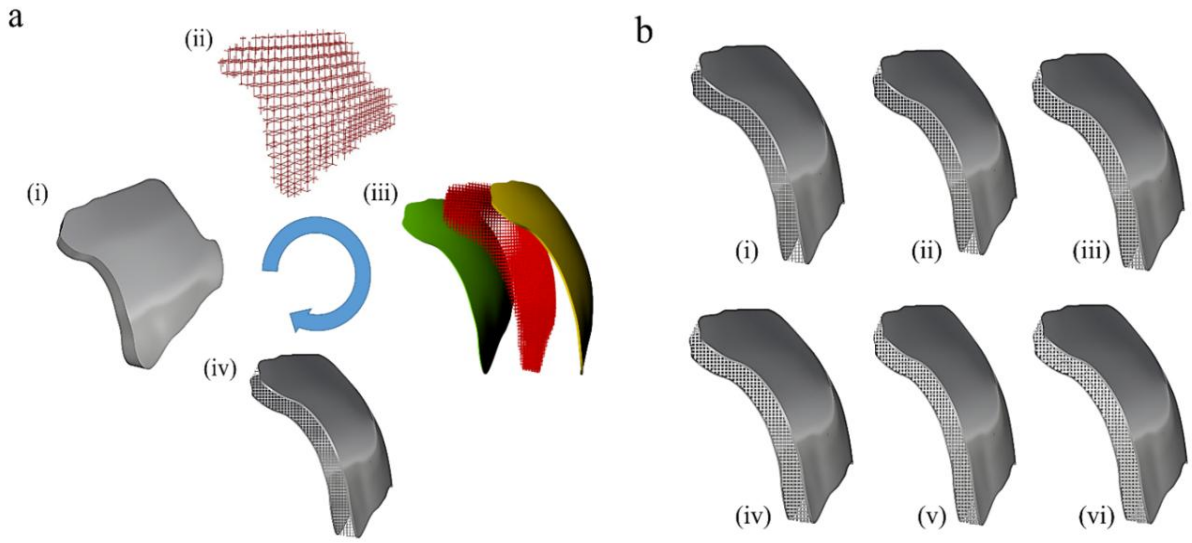

Figure 6.11 a) Modelling of a final implant with Boolean operation b) Final implant models with variable porosity

6.4 Material properties

The present implant replicates the sandwich structure, although the young's modulus is varied along the thickness. For this study, titanium alloy (Ti6Al4V) and polyether ether ketone (PEEK) materials [68], [97] are considered for structural analysis under ICP conditions (Table 6.3). These materials are frequently used for implantation and approved by FDA.

Table 6.2 Implant specifications

Thickness (mm)	6
Outer table (mm)	0.76
Inner table (mm)	0.35
Chamfered angle	30-35 degrees
Fixation point area (mm^2)	Typically 5-6
Surface area (cm^2)	Typically 10*10

Table 6.3 Material properties for structural analysis

	Titanium alloy (Ti6Al4V)	**Polyether-ether-ketone (PEEK)**
Young's modulus (MPa)	110000	4000
Poisson's ratio	0.3	0.4
Ultimate tensile strength (MPa)	950	103
Yield strength (MPa)	800	100
Density (kg/mm^3)	4430e-9	1360e-9

6.5 Boundary conditions

Three models are considered for structural analysis, such as solid implant, Type 2 implant (porosity of 82.62%) and Type 5 implant (porosity of 45.73%). The ICP is varied between 7-15 mm of Hg [2], [85], which are considered to be minimum and maximum conditions as shown in Table 6.4.

The fixation points are used to hold the implant about surrounded skull. Total of eight fixation points (a, b, c, d, e, f, and g, h) are selected randomly for three models, and the ICP is applied normal to the inner cortical surface (Figure 6.12). These fixation points are considered as fixed

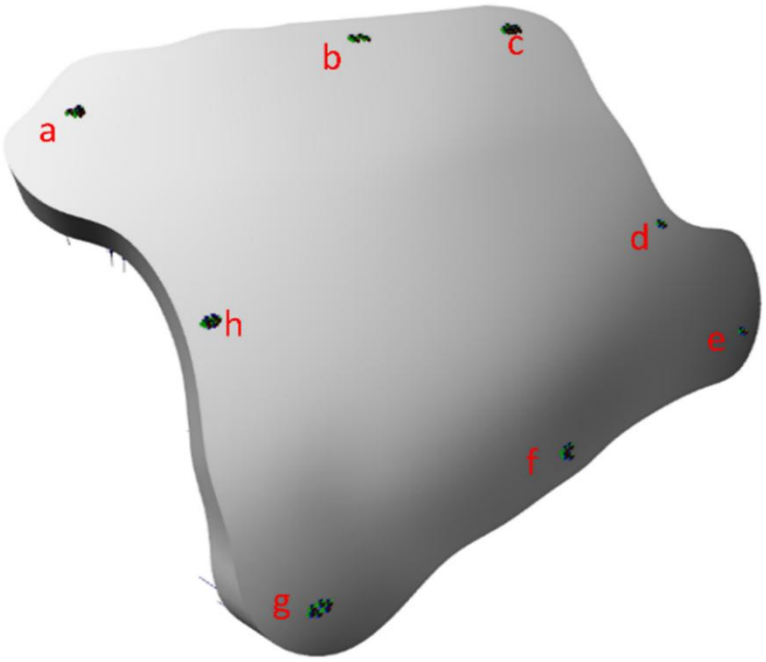

Figure 6.12 Fixation points for simulation

support (i.e. arrested in x, y and z directions). A total of 12 combinations are obtained based on the type of implant, material type and ICP conditions.

Table 6.4 Loading data for structural analysis

	Minimum Load	**Maximum Load**
Intracranial pressure	7 mm of Hg (9.34e-4 MPa)	15 mm of Hg (2e-3 MPa)

6.6 Computational models

Three computational models are selected for structural analysis. In that, two models consist of scaffold structure such as Type 2 and Type 5, and third model is the complete solid body.

6.6.1 Validation of analysis

The meshless methodology (i.e. solution structure method) divided the STL file into a number of elements (i.e. resolution) and simulated the model under minimum and maximum ICP conditions. While increasing the number of elements, the solving time automatically increases. For above three models, file sizes are varied from 350MB to 420MB. To validate the analysis, model was converged at <1% (Table 6.5). The detailed convergence data is in appendix.

Table 6.5 Total deformation and Equivalent stress analysis report

Structural analysis data			**Total deformation (mm)**			**Equivalent stress (MPa)**		
Type of Implant			**Solid**	**Type 2**	**Type 5**	**Solid**	**Type 2**	**Type 5**
Material Type and Loading Conditions	**Ti6Al4V**	**Min Load**	6.9843e-06	2.16732e-05	7.59672e-06	0.263131	0.416292	0. 298595
		Max Load	1.49557e-05	4.64109e-05	1.62671e-05	0.563450	0.891409	0.639389
	PEEK	**Min Load**	1.7478e-04	5.5566e-04	1.9696e-04	0.208271	0.369801	0.258797
		Max Load	3.7426e-04	11.7891e-04	4.2176e-04	0.445976	0.790378	0.554169

6.7 Results

The 12 combinations are simulated under minimum and maximum loading conditions and observed the Total deformation and Equivalent stress. The higher stress magnitudes are mainly concentrated at the centre of an implant and varied with the type of an implant.

6.7.1 Weight of the implant

The weight of the implant is a predominant factor (Figure 6.13), here all the implants results are compared.

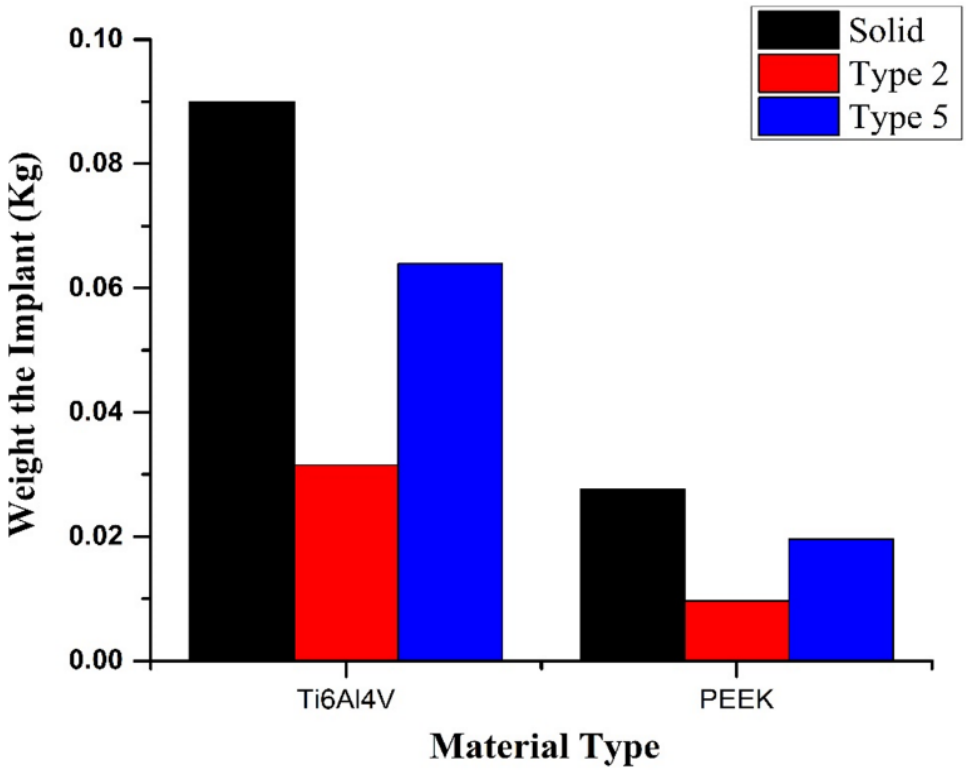

Figure 6.13 Weight of the implant with various materials

6.7.1.1 Solid implant

It is observed that the weight of Ti6Al4V and PEEK material implants are 9.0007e-2 kg and 2.7632e-2 Kg respectively. Noticeably, this implant has higher weight compared to respective geometries.

6.7.1.2 Type 2 Implant

It is observed that the weight of Ti6Al4V and PEEK material implants are 3.1545e-2 Kg and 9.6845e-3 Kg respectively. Due to higher porosity, this implant weight is less compared to respective implants.

6.7.1.3 Type 5 Implant

It is observed that the weight of Ti6Al4V and PEEK material implants are 6.3911e-2 Kg and 1.9620e-2 Kg respectively. Typically the weight of implant is the average of other two implants.

6.7.2 Influence of minimum and maximum load: Total deformation

While considering three computational models, the Total deformation values are low for solid implant. However, Type 5 implant has shown best results towards weight. In material aspects Ti6Al4V is best compared to PEEK material while considering the Total deformation result. With increase in load, correspondingly the Total deformation values are increased irrespective of implant type (Figure 6.14, 6.15, 6.16 and 6.17).

6.7.3 Influence of minimum and maximum load: Equivalent stress

While considering three computational models, the Equivalent stress values are low for solid implant. However, Type 5 implant has shown best results towards weight. In material aspects Ti6Al4V is best compared to PEEK material while considering the Equivalent stress result. With increase in load, correspondingly the Equivalent stress values are quantitatively increased for PEEK Material (Figure 6.14, 6.15, 6.16 and 6.17).

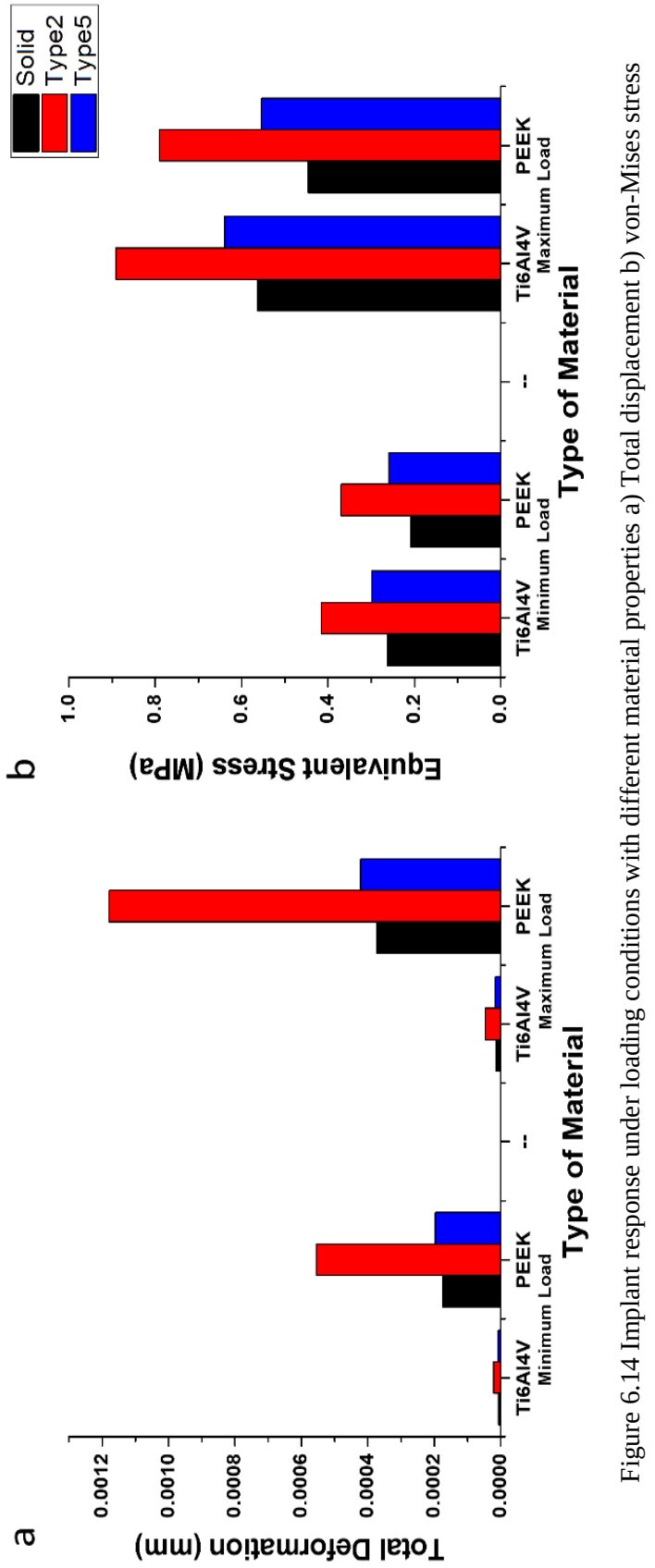

Figure 6.14 Implant response under loading conditions with different material properties a) Total displacement b) von-Mises stress

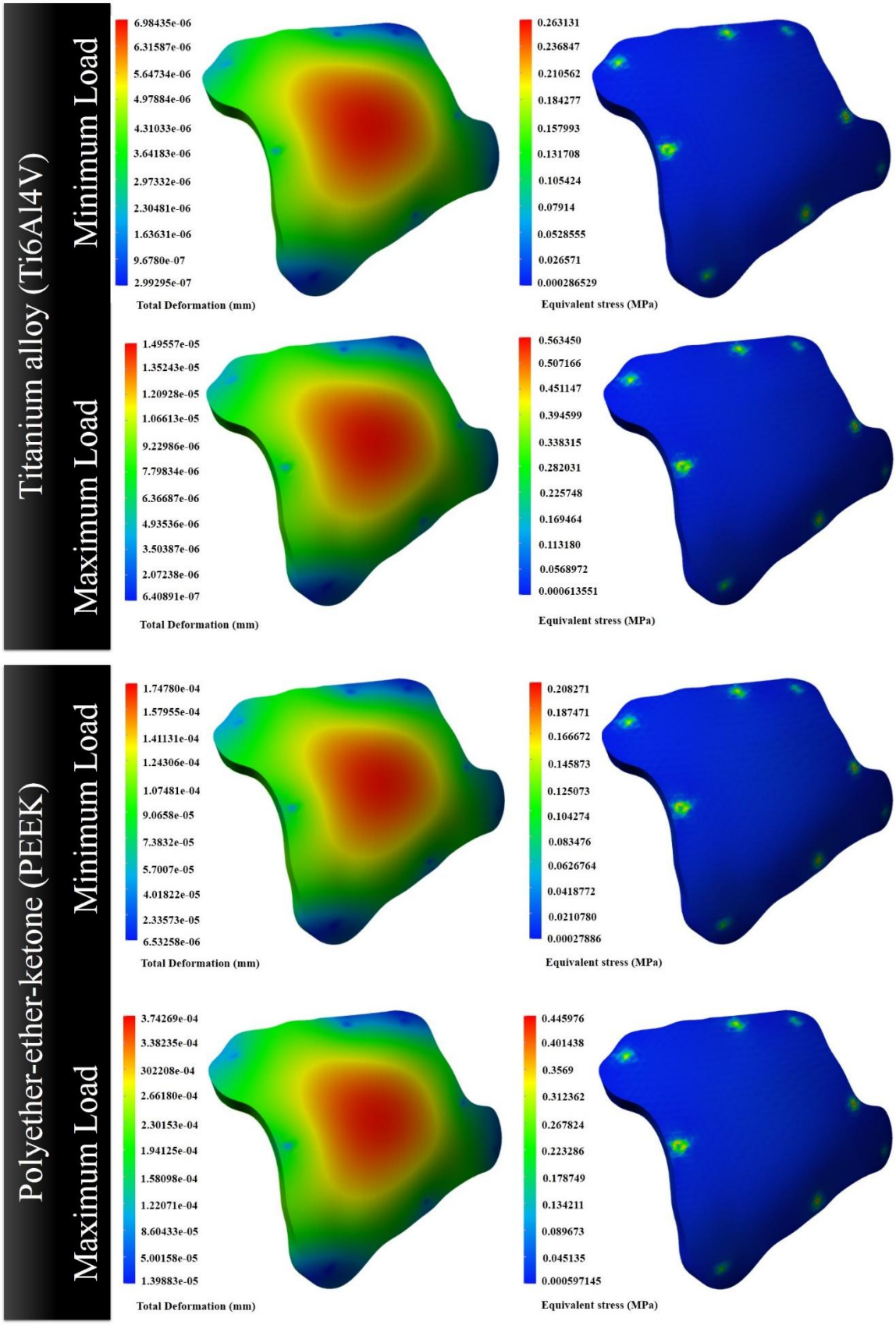

Figure 6.15 Total Deformation (left) and Equivalent stress (right) values of Solid implant under various loading conditions with different material properties

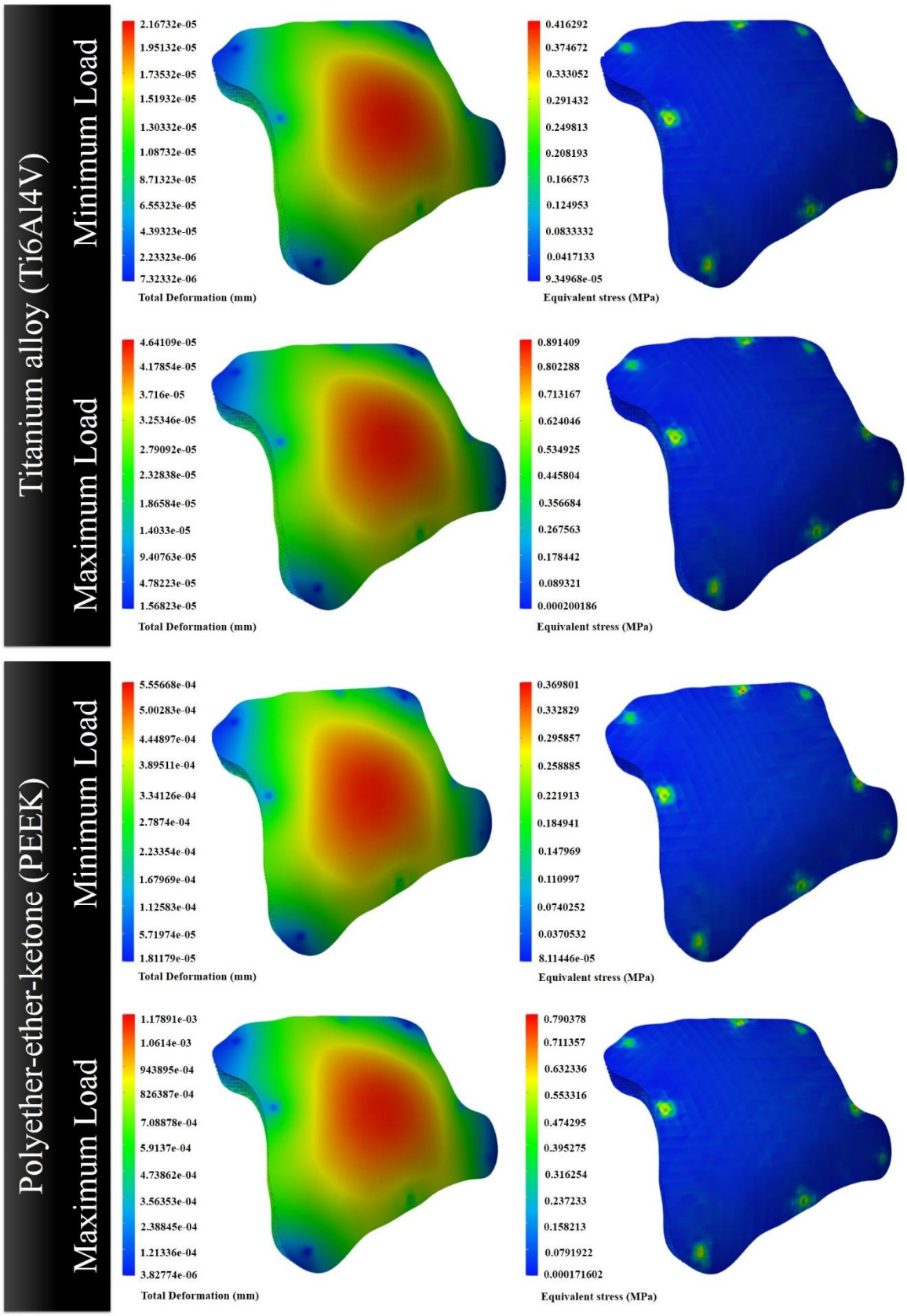

Figure 6.16 Total Deformation (left) and Equivalent stress (right) values of Type 2 implant under various loading conditions with different material properties

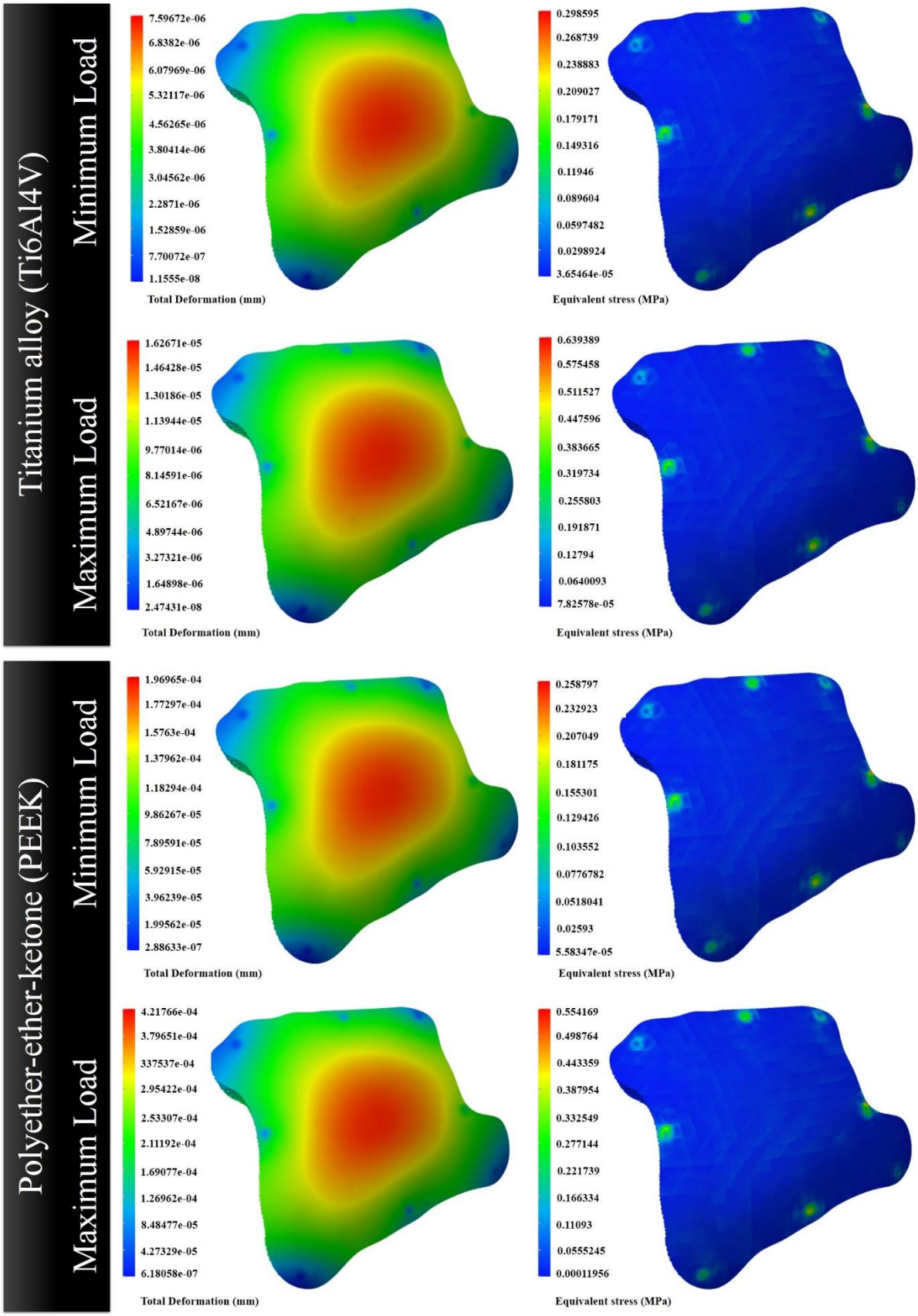

Figure 6.17 Total Deformation (left) and Equivalent stress (right) values of Type 5 implant under various loading conditions with different material properties

6.8 Discussion

The present work facilitated to design customized cranial implant for symmetrical and asymmetrical defects. These implants are embedded with homogenous scaffolds to favour Osseo integration, reduce the weight of the implant and sustain intracranial pressure. The entire work is done utilizing Rhinoceros software, and this will lead to decrease the cost of the implant for the patient.

Free form closed curve network (FCN) technique is easiest one and successfully designed the implant for both symmetrical and asymmetrical defect in few steps. Modelling the implant (Figure 6.1) to replace frontal bone is quite challenging because maintaining the surface curvature about the sagittal plane is difficult. The final implant is under the category of large defect because outer cortical surface area is greater than or equal to 100 cm^2.

An algorithm is developed to design the controlled unit cell scaffold structures and this scaffold is embedded with solid implant to promote weight reduction as well as Osseo intergration. The unit cell size is fixed as 1 mm in X, Y and Z axes direction, due to this the Osseo integration [67] is possible in the lateral direction of the implant. The biological coating needs to promote the tissue growth, which is not discussed in this paper.

The six implants are designed with variable porosity and pore size using modelling software and algorithm. These implants are mimicked the original parietal bone of the skull, however, the Type 5 implant was technically mimicked the parietal bone as per microCT data. Among all models, the solid, Type 2 and Type 5 implants are selected for structural analysis through meshless method. Type 2 implant has chosen to be best based on Osseo integration and less weight aspects. The present paper has not discussed the Osseo integration.

Type 2 and Type 5 implants replicated the sandwich structures, the material property like young's modulus varies with thickness. However, the modelled implant directly simulated through software, so defining material's porosity is not required. Whereas in analytical approach, defining material's porosity is necessary because the porosity of implant directly effects the young's modulus of the scaffold.

Type 2 and Type 5 implants are analysed under ICP conditions and compared with the solid implant. The meshless methods are developed to simulate the body under various loads without using traditional FEA especially data from scanned, digitized and medical CT scans (i.e. the physical analysis of cadaver bones is expensive and impractical on a large scale). In this

connection, the Scan & Solve plugin was recently implemented in Rhinoceros modelling software. The performance of this plugin is compared with commercial FEA software, and solved the models containing small errors and noise boundaries [70].

Figure 6.18 Final 3D printed component

The mesh less approach requires input data to address the model under loading condition. Among all input data, the element size is crucial one to solve the problem. If the element size decreases, the solving time automatically increases. For Type 2 and Type 5 implants, the element size is maintained nearly twice the size of the lattice cell to one fifth of it and are converged at 0.38 mm and 0.44 mm respectively.

These computational models are merely recommended for preoperative planning as this study was not yet recommended by clinicians. The results presented here are for future perspective, and it is fundamentally difficult to validate with numerical analysis [88], [89]because the skull thickness and porosity are varied by age and sex.

Recently, the cranial implants have been replaced by polyether ether ketone (PEEK) and titanium alloy (Ti6Al4V) materials. The implants are fixed at eight points for simulating under ICP conditions. With the help of loading data and type of material, the Total deformation and Equivalent stress results are observed. Among three computational models, the solid implant showed effective results compared to other implants, however failed in the direction of weight and Osseo integration. Type 5 showed best results among all implants. However, the Osseo integration

is poor compared to Type 2 Implant. The Type 5 implant was printed in the 3D printer for visualization purpose with the polymer material as shown in the Figure 6.18. Lastly, the Ti6Al4V is the best material to fulfil all the aspects while cost a clever bit high compared to PEEK material.

6.9 Conclusion

The modelling of Homogenous scaffold based cranial implant is done with FCN technique for both symmetrical and asymmetrical defects. Most notably, this is the study to our knowledge to investigate the effectiveness of unit cell algorithm intervention in the implant. The structural analysis is performed through the meshless method with Ti6Al4V and PEEK materials at ICP loading conditions. It was observed that, the titanium based solid implant is the best one in all aspects. While considering weight, cost and Osseo integration, PEEK based Type 5 implant is the best one.

However, some limitations are worth. Although, our hypotheses were supported for the future scope. The FCN technique has few limitations such, controlling surface curvature and trimming surface edges is quite challenging. The unit cell algorithm dealt with closed surface bodies only and needed to remove the extended lines of unit cells. The future scope deals with Osseo integration through biological coatings and to model gradient/variable porous implant with different unit cell configurations.

CHAPTER 7
7. CONCLUSION AND FUTURE SCOPE

The present research work has made an attempt to develop innovative possibilities in cranial implant modelling techniques, which can handle symmetrical and asymmetrical defects and modelled the cranial implant with optimum number of fixation points which help to arrest the cerebrospinal fluid (CSF) leak. Finally, a homogenous scaffold-based cranial implant is developed, which mimics cranial bone in order to enhance tissue regeneration.

In this thesis, at the start modelling of the cranial implant is done through mirroring technique at a thickness of 2.5 mm and the edges of the implant are corrected to arrest the CSF leak. This implant is developed to cover frontal, parietal and temporal regions. However, the challenge is to maintain the curvature and constrained implant thickness. To overcome these limitations a computer-aided reconstruction technique is developed.

The implant is modelled with computer-aided reconstruction technique at 4 mm of thickness and the above-mentioned limitations are overcome. Additionally, the finite element analysis is conducted on the cranial implant under intracranial pressure (ICP) with a minimum number of anatomical locations. However, increased anatomical locations lead to decrease in deformation and equivalent stress is observed. Consequently, the mechanical deformation and equivalent stress (von Mises) are calculated in ANSYS 15 software with different materials such as titanium alloy (Ti6Al4V), polymethyl methacrylate (PMMA) and polyether ether ketone (PEEK). It is observed that Ti6Al4V shows low deformation and PEEK shows less equivalent stress. However, this implant is completely solid one and cannot promote the required tissue regeneration. To overcome this, the implant is embed with optimum permeable scaffold structures.

The scaffold structures are developed to enhance tissue regeneration. In this research work, homogeneous interconnected scaffold structures are modelled with variable pore-size, porosity, and various strut cross-section such as circular, square and hexagon. The CFD analysis has been done in ANSYS 15 software to know the permeability of scaffold with blood properties as a fluid. The Permeability is found to be in the range of 4.8×10^{-9} m^2 – 2.3×10^{-8} m^2 for strut cross-section 300 to 500 µm. Finally, the circular cross-section is showed effective permeability compare to hexagon and square cross-sections. From these results, the solid implant is embedded with unit cell based scaffold structures to mimic the original cranial bone.

The final part of the research is discussed with a novel free-form closed curve network (FCN) technique, which is successfully addressing both the symmetrical and asymmetrical defects. The implant is embedded in a unit cell based porous structure. Totally six types of implants are modelled with variation in porosity and replicate the original cranial bone. Among six implants, Type 2 (porosity 82.62%) and Type 5 (porosity 45.73%) implants are analysed with the meshless approach under ICP. The total deformation and equivalent stress (von Mises stress) of porous implants are compared with the solid implant under same ICP conditions.

While considering titanium alloy as a solid implant and Type 5 implant, the significant weight reduction is observed as 28.99%, the total deformation and equivalent stress results are increased 8.06% and 11.87% at minimum and maximum load conditions.

While considering PEEK material as a solid implant and Type 5 implant, the significant weight reduction is observed as 28.99%, the total deformation and equivalent stress results are increased 11.26% and 19.52% at minimum and maximum load conditions.

Finally comparing Type 5 implant as titanium alloy and PEEK materials

- The significant weight reduction in PEEK implant is observed as 69.3% while comparing with the titanium implant.
- The total deformation results are increased in PEEK implant significantly 24.9% at minimum and maximum load conditions.
- The equivalent stress results are decreased in PEEK implant significantly 13.33% at minimum and maximum load conditions.

From this research work, it was observed that the titanium implant is effective in deformation aspect. While considering weight and cost, the PEEK implant is showing significant results. The entire research work has been concluded that the PEEK is most effective material to replace cranial defects.

7.1 Future scope

The future scope deals with Osseo integration through biological coatings and to model gradient/variable porous implant with different unit cell configurations.

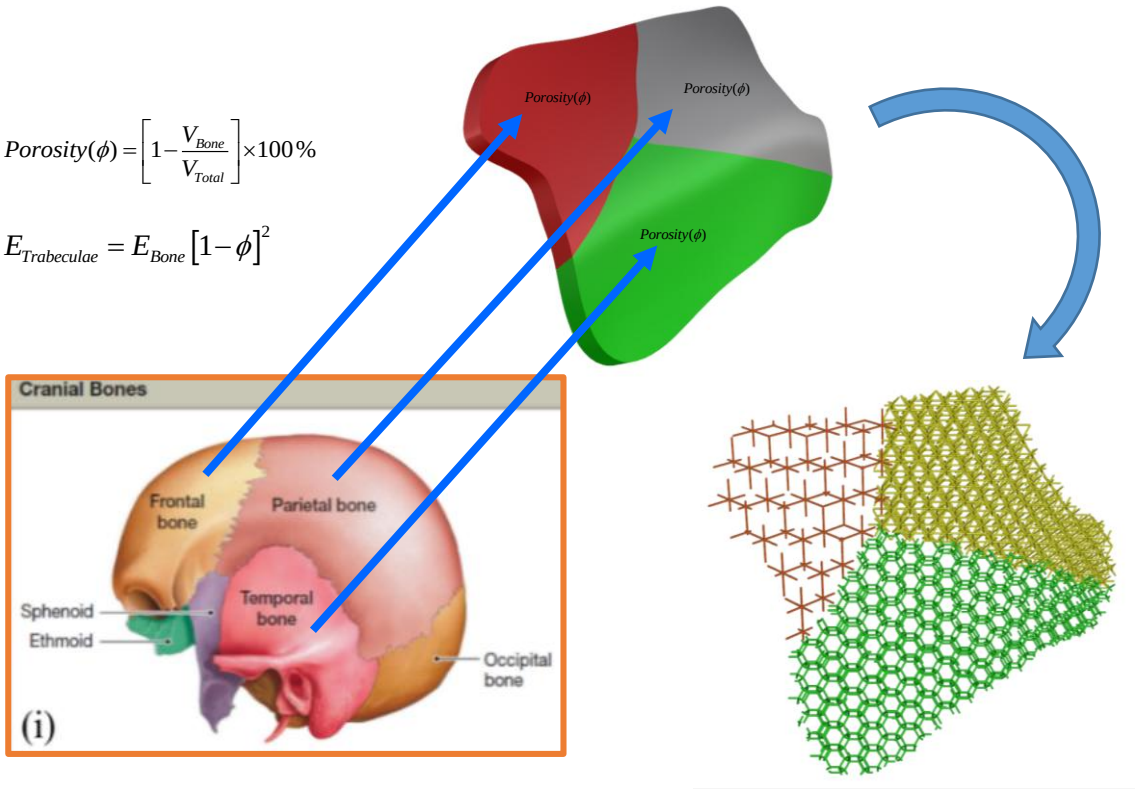

Figure 7.1 Cranial implant with variable porosity

The current research work discusses about FCC unitcell structure, however, the cranial bone porosities are varying with respect to age, sex and type of cranial bone. In this aspect, we are trying to develop cranial implant with various unitcell configurations to mimic individual cranial bones such as temporal, parietal and frontal bones.

The frontal, temporal and parietal bones are replaced with FCC, star and cubic unitcells as shown in the Figure 7.1. The selection of unitcell is depends on micro-CT data of various patients. Here, the challenge is involved in computer aided modelling of cranial implant with different unitcells and replicate the sutures of the cranial bones. The sutures are junction lines of the cranial bones.

Additionally, we are developing analytical relationship between young's modulus and porosity of cranial bone with the help of Gibson and Ashby equation.

8. BIBLIOGRAPHY

[1] E. N. Marieb, *Human Anatomy*, 6th ed. Pearson, 2012.

[2] L. A. Steiner and P. J. D. Andrews, "Monitoring the injured brain: ICP and CBF," *Br. J. Anaesth.*, vol. 97, no. 1, pp. 26–38, 2006.

[3] X. Wang, S. Xu, S. Zhou, W. Xu, M. Leary, P. Choong, M. Qian, M. Brandt, and Y. M. Xie, "Topological design and additive manufacturing of porous metals for bone scaffolds and orthopaedic implants: A review," *Biomaterials*, vol. 83, pp. 127–141, 2016.

[4] J. Y. Rhoa, "Mechanical properties and the hierarchical structure of bone," *Med. Eng. Phys.*, vol. 20, no. 2, pp. 92–102, 1998.

[5] U. G. K. Wegst, H. Bai, E. Saiz, A. P. Tomsia, and R. O. Ritchie, "Bioinspired structural materials," *Nat. Publ. Gr.*, vol. 14, no. 23–26, pp. 1–14, 2014.

[6] K. C. J. L. Kuhn, M. J. Ciarelli, and S. A. Goldstein, "The Elastic Moduli Of Human Subchondral , Trabecular , And Cortical Bone Tissue And The Size-Dependency Of Cortical Bone Modulus," *J. Biomech.*, vol. 23, no. 11, pp. 1103–1113, 1990.

[7] U. S. Depertment, "Get the Stats on Traumatic Brain Injury in the United States," 2006.

[8] Medical dictionary, "Head injury," *https://medical- dictionary.thefreedictionary.com/ head+injury*, 2018.

[9] Online, "Infant Skull Fracture : Causes , Signs & Treatment Call our experienced lawyers TODAY to get a free legal Skull Fractures In Babies : Types Call our experienced," *http://caringforspecialneedskids.com/infant-skull-fracture/*, 2018. .

[10] Johan Hopkisonmedicine., "Head Injury," *https://www.hopkinsmedicine.org/healthlibrary /conditions/nervous_system_disorders/head_injury_85,P00785*, 2018.

[11] Pocketdentistry, "Antomical planes," *Https://pocketdentistry.com/4-anatomy-and-physiology /*, 2018.

[12] L. C. Hieu, E. Bohez, J. Vander Sloten, H. N. Phien, E. Vatcharaporn, P. H. Binh, P. V. An, and P. Oris, "Design for medical rapid prototyping of cranioplasty implants," *Rapid Prototyp. J.*, vol. 9, no. 3, pp. 175–186, 2003.

[13] F. C. Grant, "Repair of cranial defects by cranioplasty," *Ann. Surg.*, vol. 110, no. 4, pp. 488–

512, 1933.

[14] Dragoslav Stula, *Cranioplasty Indications, Techniques, and Results*, 1st ed. Springer-Verlag Wien New York, 1984.

[15] M. Tadros and P. D. Costantino, "Advances in Cranioplasty : A Simplified Algorithm to Guide Cranial Reconstruction of Acquired Defects," *Facial Platics Surg.*, vol. 1, no. 212, pp. 135–145, 2008.

[16] H. N. Chia and B. M. Wu, "Recent advances in 3D printing of biomaterials," *J. Biol. Eng.*, vol. 9, no. 4, pp. 1–14, 2015.

[17] C. Unterhofer, C. Wipplinger, M. Verius, W. Recheis, C. Thomé, and M. Ortler, "ScienceDirect Reconstruction of large cranial defects with poly-methyl-methacrylate (PMMA) using a rapid prototyping model and a new technique for intraoperative implant modeling," *J. Dermatol. Sci.*, pp. 1–7, 2017.

[18] M. Fisher and M. Lim, "Multidisciplinary Approach for Improved Outcomes in Secondary Cranial Reconstruction: Introducing the Pericranial-Onlay Cranioplasty Technique," *Oper. Neurosurg.*, vol. 10, no. 2, pp. 179–190, 2014.

[19] G. Clovis, D. Costa, M. A. Aras, and P. Chalakkal, "A Unique Flask Design for Processing Cranial Prosthesis Using Heat Cured Acrylic - A Case Report," *J. Clin. Diagnostic Res.*, vol. 10, no. 9, pp. 14–16, 2016.

[20] S. Aatman M, "Materials used in cranioplasty: a history and analysis," *neurosurg Focus*, vol. 36, no. April, pp. 1–7, 2014.

[21] J. Kwarcinski, P. Boughton, A. Ruys, A. Doolan, and J. Van Gelder, "Cranioplasty and Craniofacial Reconstruction : A Review of Implant Material , Manufacturing Method and Infection Risk," *Appl. Sci.*, vol. 7, no. 276, pp. 1–17, 2017.

[22] J. Brie, T. Chartier, C. Chaput, C. Delage, B. Pradeau, F. Caire, M. Boncoeur, and J. Moreau, "A new custom made bioceramic implant for the repair of large and complex craniofacial bone defects," *J. Cranio-Maxillofacial Surg.*, pp. 1–5, 2012.

[23] H. Ono, T. Sase, Y. Tanaka, and H. Takasuna, "Histological assessment of porous custom ‐ made hydroxyapatite implants 6 months and 2.5 years after cranioplasty," *Surg. Neurol. Int.*, vol. 8, pp. 1–6, 2017.

[24] S. Manjila, "Prevention of postoperative cerebrospinal fluid leaks with multilayered reconstruction using titanium mesh–hydroxyapatite cement cranioplasty after translabyrinthine resection of acoustic neuroma," *J. Neurosurg.*, vol. 119, pp. 113–120, 2013.

[25] S. Fusetti, "Cranial Vault & Skull Base - Reduction & Fixation - Special considerations - AO Surgery Reference," *https://www2.aofoundation.org/wps/portal/surgery?showPage=redfix&bone=CMF&segment=Cranium&classification=93-=&method=Special%20considerations&implantstype=hidden&approach=&redfix_url=1289999576062&Language=en*, 2018.

[26] S. Berretta, K. Evans, and O. Ghita, "Additive manufacture of PEEK cranial implants : Manufacturing considerations versus accuracy and mechanical performance," *Mater. Des.*, vol. 139, pp. 141–152, 2018.

[27] J. Parthasarathy, "3D modeling , custom implants and its future perspectives in craniofacial surgery," *Ann. Maxillofac. Surg.*, vol. 4, no. 1, pp. 9–18, 2014.

[28] S. Gopakumar, "RP in medicine: a case study in cranial reconstructive surgery," *Rapid Prototyp. J.*, vol. 10, no. 3, pp. 207–211, 2004.

[29] E. Heissler, F. Fischer, S. B. T. Lehmann, W. Mathar, A. Gebhardt, E. Hehmler, R. Fischer, S. Boloud, and T. Lehmann, "Custom-made cast titanium implants produced with CAD / CAM for the reconstruction of cranium defects," *Int. J. Oral Maxillofac. Surg.*, vol. 27, pp. 334–338, 1998.

[30] E. B. O'Reilly, S. Barnett, C. Madden, B. Welch, B. Mickey, and S. Rozen, "Computed-tomography modeled polyether ether ketone (PEEK) implants in revision cranioplasty," *J. Plast. Reconstr. Aesthetic Surg.*, vol. 68, no. 3, pp. 329–338, 2015.

[31] D. J. Bonda, S. Manjila, W. R. Selman, and D. Dean, "The Recent Revolution in the Design and Manufacture of Cranial Implants: Modern Advancements and Future Directions," *Neurosurgery*, vol. 77, no. 5, pp. 814–824, 2015.

[32] E. Nout and M. Y. Mommaerts, "Considerations in computer-aided design for inlay cranioplasty : technical note," *Oral Maxillofac. Surg.*, vol. 22, no. 1, pp. 65–69, 2018.

[33] J. Poukens, P. Laeven, M. Beerens, G. Nijenhuis, P. Stoelinga, and P. Kessler, "A classification of cranial implants based on the degree of difficulty in computer design and

manufacture," no. November 2007, pp. 46–50, 2008.

[34] N. K. Sahoo, Ã. M. R. N, K. Tomar, and S. Bhat, "Classification of the Residual Cranial Defects and Selection of Reconstruction Materials," *J. Craniofac. Surg.*, vol. 7, no. 0, pp. 1694–1701, 2017.

[35] L. R. Williams, K. F. Fan, and R. P. B. Custom-made, "Custom-made titanium cranioplasty : early and late complications of 151 cranioplasties and review of the literature," *Int. J. Oral Maxillofac. Surg.*, vol. 44, no. 5, pp. 599–608, 2015.

[36] N. J. Mokal and M. F. Desai, "Calvarial reconstruction using high-density porous polyethylene cranial hemispheres," *Indian J. Plast. Surg.*, vol. 44, no. 3, pp. 422–431, 2011.

[37] M. Martin, FH. Timmons, *Human anatomy*, Second. Pearson, 2012.

[38] P. Motherway, Julie A.; Verschueren, "Provided by the author(s) and University College Dublin Library in accordance with publisher policies. Please cite the published version when available.," *J. Biomech.*, vol. 42, no. 13, pp. 2129–2135, 2009.

[39] S. Boruah, K. Henderson, D. Subit, R. S. Salzar, B. S. Shender, and G. Paskoff, "IRC-13-54 IRCOBI Conference 2013," *ircobi Conf.*, pp. 497–508, 2013.

[40] S. Torimitsu, Y. Nishida, T. Takano, D. Yajima, and G. Inokuchi, "Differences in biomechanical properties and thickness among frontal and parietal bones in a Japanese sample," *Forensic Sci. Int.*, vol. 252, p. 190.e1-190.e6, 2015.

[41] J. A. Motherway, P. Verschueren, G. Van Der Perre, J. Vander, and D. Gilchrist, "The mechanical properties of cranial bone : The effect of loading rate and cranial sampling position," *J. Biomech.*, vol. 42, pp. 2129–2135, 2009.

[42] A. Auperrin, R. Delille, D. Lesueur, K. Bruyère, C. Masson, P. Drazétic, F.- Marseille, and F.- Marseille, "Geometrical and material parameters to assess the macroscopic mechanical behaviour of fresh cranial bone samples," *J. Biomech.*, vol. 47, pp. 1180–1185, 2014.

[43] D. Singh, D. Singh, and S. S. Han, "3D Printing of Scaffold for Cells Delivery : Advances in Skin Tissue Engineering," *Polymers*, vol. 8, no. 1, pp. 1–19, 2016.

[44] S. Giannitelli, "Current trends in the design of scaffolds for computer-aided tissue engineering," *Acta Biomater.*, vol. 10, pp. 580–594, 2014.

[45] B. Sébastien B G, "Surface curvature in triply-periodic minimal surface architectures as a

distinct design parameter in preparing advanced tissue engineering scaffolds," *Biofabrication*, vol. 9, pp. 1–12, 2017.

[46] J. Grimm and J. L. Williams, "Measurements of permeability in human calcaneal trabecular bone," *j biomech.*, vol. 30, no. 1, pp. 743–745, 1997.

[47] S. Li, J. R. D. E. Wijn, J. Li, P. Layrolle, and K. D. E. Groot, "Macroporous Biphasic Calcium Phosphate Scaffold with High Permeability / Porosity Ratio," *tissue Eng.*, vol. 9, no. 3, pp. 535–548, 2003.

[48] K. Lee and S. Wang, "Fabrication and Characterization of Poly(Propylene Fumarate) Scaffolds with Controlled Pore Structures Using 3-Dimensional Printing and Injection Molding," *tissue Eng.*, vol. 12, no. 10, pp. 2801–2811, 2006.

[49] A. Sanz-herrera, M. Garcı, M. Doblare, I. Ochoa, D. M. Yunos, and A. R. Boccaccini, "Permeability evaluation of 45S5 Bioglass s -based scaffolds for bone tissue engineering," *J. Biomech.*, vol. 42, pp. 257–260, 2009.

[50] C. G. Jeong, H. Zhang, and S. J. Hollister, "Permeability effects on sub-cutaneous in vivo chondrogenesis using primary chondrocytes," *Acta Biomater.*, vol. 7, no. 2, pp. 505–514, 2011.

[51] S. Truscello, G. Kerckhofs, S. Van Bael, G. Pyka, J. Schrooten, and H. Van Oosterwyck, "Prediction of permeability of regular scaffolds for skeletal tissue engineering: A combined computational and experimental study," *Acta Biomater.*, vol. 8, no. 4, pp. 1648–1658, 2012.

[52] P. F. Egan, V. C. Gonella, M. Engensperger, S. J. Ferguson, and K. Shea, "Computationally designed lattices with tuned properties for tissue engineering using 3D printing," *PLoS One*, vol. 12, no. 8, p. e0182902, 2017.

[53] J. C. M. Teo and S. H. Teoh, "Permeability study of vertebral cancellous bone using micro-computational fluid dynamics," *Comput Methods in Biomech and Biomed Engin.*, vol. 15, no. 4, pp. 417–423, 2012.

[54] S. Lee, C. Wu, S. Lee, and P. Chen, "Cranioplasty using polymethyl methacrylate prostheses," *J. Clin. Neurosci.*, vol. 16, no. 1, pp. 56–63, 2009.

[55] B. Kim, K. Hong, D. Ph, K. Park, D. Ph, D. Park, D. Ph, Y. Chung, and D. Ph, "Customized Cranioplasty Implants Using Three-Dimensional Printers and Polymethyl-Methacrylate

Casting," *J Korean Neurosurg*, vol. 52, pp. 541–546, 2012.

[56] P. R. Monich, B. Henriques, A. P. Novaes, D. Oliveira, J. C. M. Souza, and M. C. Fredel, "Mechanical and biological behavior of biomedical PEEK matrix composites : A focused review," *Mater. Lett.*, vol. 185, pp. 593–597, 2016.

[57] P. Brandicourt, "Reconstruction of Cranial Vault Defect with Polyetheretherketone Implants," *World Neurosurg.*, vol. 105, pp. 783–789, 2017.

[58] J. Jonkergouw, S. E. C. M. Van De Vijfeijken, E. Nout, T. Theys, E. Van De Casteele, H. Folkersma, P. R. A. M. Depauw, and A. G. Becking, "Outcome in patient-speci fi c PEEK cranioplasty : A two-center cohort study of 40 implants," *J. Cranio-Maxillofacial Surg.*, vol. 44, no. 9, pp. 1266–72, 2016.

[59] L. Williams, K. Fan, and R. Bentley, "Titanium cranioplasty in children and adolescents," *J. Cranio-Maxillofacial Surg.*, vol. 44, no. 7, pp. 789–94, 2016.

[60] E. Park, Ã. J. Lim, I. Yun, and J. Kim, "Cranioplasty Enhanced by Three-Dimensional Printing : Custom-Made Three-Dimensional-Printed Titanium Implants for Skull Defects," *J. Craniofac. Surg.*, vol. 27, no. 4, pp. 943–949, 2016.

[61] S. H. Jeong, U. S. Wang, and S. W. Kim, "Symptomatic Epidural Fluid Collection Following Cranioplasty after Decompressive Craniectomy for Traumatic Brain Injury," *Korean J Neurotrauma*, vol. 12, no. 1, pp. 6–10, 2016.

[62] P. Maricevich, "Original Article Cranioplasties : surgical reconstruction strategies Cranioplastias : estratégias cirúrgicas de reconstrução," *Rev. Bras. Cir. Plást*, vol. 31, no. 1, pp. 32–42, 2016.

[63] K. Ashayeri, E. M. Jackson, and J. Huang, "Syndrome of the Trephined : A Systematic Review," *Neurosurgery*, vol. 79, no. 4, pp. 525–534, 2016.

[64] J. Skoworodko, K. Skalski, W. Cejmer, and K. Kwiatkowski, "Preoperative planning and post-operative estimation of vertebroplasty using CT/CAD/CAE systems," *Acta Bioeng. Biomech.*, vol. 10, no. 2, pp. 15–22, 2008.

[65] A. Tsouknidas, S. Maropoulos, S. Savvakis, and N. Michailidis, "FEM assisted evaluation of PMMA and Ti6Al4V as materials for cranioplasty resulting mechanical behaviour and the neurocranial protection," *Biomed. Mater. Eng.*, vol. 21, no. 3, pp. 139–147, 2011.

[66] D. Parle, "Patient Specific Design and Validation of Cranial Implants using FEA," *Altair Technol. Conf.*, pp. 1–9, 2015.

[67] F. El Halabi, J. F. Rodriguez, L. Rebolledo, E. Hurts, and M. Doblar, "Mechanical characterization and numerical simulation of polyether-ether-ketone (PEEK) cranial implants," *J. Mech. Behav. Biomed. Mater.*, vol. 4, no. 8, pp. 1819–1832, 2011.

[68] A. Ridwan-Pramana, P. Marcián, L. Borák, N. Narra, T. Forouzanfar, and J. Wolff, "Structural and mechanical implications of PMMA implant shape and interface geometry in cranioplasty - A finite element study," *J. Cranio-Maxillofacial Surg.*, vol. 44, no. 1, pp. 34–44, 2016.

[69] M. K. Freytag, V. Shapiro, and I. Tsukanov, "Scan and Solve: Acquiring the Physics of Artifacts," in *IDETC/CIE 2007*, 2006, pp. 1–12.

[70] M. Freytag, V. Shapiro, and I. Tsukanov, "Finite element analysis in situ," *Finite Elem. Anal. Des.*, vol. 47, no. 9, pp. 957–972, 2011.

[71] T. Kosta and I. Tsukanov, "Three-Dimensional Natural Vibration Analysis With Meshfree Solution Structure Method," *J. Vib. Acoust.*, vol. 136, no. 5, p. 51011, 2014.

[72] S. Singare, Q. Lian, W. Ping Wang, J. Wang, Y. Liu, D. Li, and B. Lu, "Rapid prototyping assisted surgery planning and custom implant design," *Rapid Prototyp. J.*, vol. 15, no. 1, pp. 19–23, 2009.

[73] J. Felipe, I. Saldarriaga, S. C. Vélez, M. E. C. Andrés, and T. Valencia, "Design and Manufacturing of a Custom Skull Implant," *Am. J. engeering Appl. Sci.*, vol. 4, no. 1, pp. 169–174, 2011.

[74] T. Wu, M. Engelhardt, L. Fieten, A. Popovic, and K. Radermacher, "Anatomically Constrained Deformation for Design of Cranial Implant: Methodology and Validation," in *Medical Image Computing and Computer-Assisted Intervention -- MICCAI 2006*, 2006, pp. 9–16.

[75] N. Lynnerup, J. G. Astrup, and B. Sejrsen, "Thickness of the human cranial diploe in relation to age, sex and general body build," *Head Face Med.*, vol. 1, no. 1, p. 13, 2005.

[76] N. Lynnerup, "Cranial thickness in relation to age , sex and general body build in a Danish forensic sample," *Forensic Sci Int.*,vol. 117, no. 1-2, pp. 45–51, 2001.

[77] W. J. van der Meer, R. R. M. Bos, A. Vissink, and A. Visser, "Digital planning of cranial implants," *Br. J. Oral Maxillofac. Surg.*, vol. 51, no. 5, pp. 450–452, 2013.

[78] A. L. Jardini, M. A. Larosa, R. M. Filho, C. A. D. C. Zavaglia, L. F. Bernardes, C. S. Lambert, D. R. Calderoni, and P. Kharmandayan, "Cranial reconstruction: 3D biomodel and custom-built implant created using additive manufacturing," *J. Cranio-Maxillofacial Surg.*, vol. 42, no. 8, pp. 1877–1884, 2014.

[79] D. Larysz, W. Wolański, E. Kawlewska, M. Mandera, and M. Gzik, "Biomechanical aspects of preoperative planning of skull correction in children with craniosynostosis," *Acta Bioeng. Biomech.*, vol. 14, no. 2, pp. 19–26, 2012.

[80] R. Chrzan, A. Urbanik, K. Karbowski, M. Moskala, J. Polak, and M. Pyrich, "Cranioplasty prosthesis manufacturing based on reverse engineering technology.," *Med. Sci. Monit.*, vol. 18, no. 1, p. MT1-6, 2012.

[81] E. Chacón-Moya, J. F. Gallegos-Hernández, S. Piña-Cabrales, F. Cohn-Zurita, and A. Goné-Fernández, "Cranial vault reconstruction using computer-designed polyetheretherketone (PEEK) implant: case report.," *Cir. Cir.*, vol. 77, no. 6, pp. 437–440, 2009.

[82] J. J. Chen, W. Liu, M. Z. Li, and C. T. Wang, "Digital manufacture of titanium prosthesis for cranioplasty," *Int. J. Adv. Manuf. Technol.*, vol. 27, no. 11–12, pp. 1148–1152, 2006.

[83] B. Lethaus, Y. Safi, M. ter Laak-Poort, A. Kloss-Brandstätter, F. Banki, C. Robbenmenke, U. Steinseifer, and P. Kessler, "Cranioplasty with Customized Titanium and PEEK Implants in a Mechanical Stress Model," *J. Neurotrauma*, vol. 29, no. 6, pp. 1077–1083, 2012.

[84] H. Rotaru, H. Stan, I. S. Florian, R. Schumacher, Y. T. Park, S. G. Kim, H. Chezan, N. Balc, and M. Baciut, "Cranioplasty with custom-made implants: Analyzing the cases of 10 patients," *J. Oral Maxillofac. Surg.*, vol. 70, no. 2, pp. e169–e176, 2012.

[85] S. Brimioulle, J. J. Moraine, D. Norrenberg, and R. J. Kahn, "Effects of positioning and exercise on intracranial pressure in a neurosurgical intensive care unit.," *Phys. Ther.*, vol. 77, no. 12, pp. 1682–1689, 1997.

[86] T. Nagasao, J. Miyamoto, H. Jiang, T. Kaneko, and T. Tamaki, "Biomechanical analysis of the effect of intracranial pressure on the orbital distances in trigonocephaly," *Cleft Palate-Craniofacial J.*, vol. 48, no. 2, pp. 190–196, 2011.

[87] "PEEK material properties." [Online]. Available: https://www.makeitfrom.com/material-properties/Polyetheretherketone-PEEK.

[88] M. Viceconti, S. Olsen, L. P. Nolte, and K. Burton, "Extracting clinically relevant data from finite element simulations," *Clin. Biomech.*, vol. 20, no. 5, pp. 451–454, 2005.

[89] M. J. Griffin, "The validation of biodynamic models," *Clin. Biomech.*, vol. 16, no. 1, pp. S81–S92, 2001.

[90] V. A. A. Santamaría, M. Malvè, A. Duizabo, A. Mena Tobar, G. Gallego Ferrer, J. M. García Aznar, M. Doblaré, and I. Ochoa, "Computational methodology to determine fluid related parameters of non regular three-dimensional scaffolds," *Ann. Biomed. Eng.*, vol. 41, no. 11, pp. 2367–2380, 2013.

[91] Z. Luo, Q. Zhang, M. Shi, Y. Zhang, W. Tao, and M. Li, "Effect of pore size on the biodegradation rate of silk fibroin scaffolds," *Adv. Mater. Sci. Eng.*, vol. 2015, pp. 1–8, 2015.

[92] V. P. Bogu, Y. R. Kumar, and A. K. Khanra, "Homogenous scaffold-based cranial / skull implant modelling and structural analysis — unit cell algorithm-meshless approach," *Med. Biol. Eng. Comput.*, vol. 55, no. 11, pp. 2053–2065, 2017.

[93] Q. L. Loh and C. Choong, "Three-Dimensional Scaffolds for Tissue Engineering Applications: Role of Porosity and Pore Size," *Tissue Eng. Part B Rev.*, vol. 19, no. 6, pp. 485–502, 2013.

[94] S. Sadir, M. R. A. Kadir, A. Öchsner, and M. N. Harun, "Modeling of Bio Scaffolds : Structural and Fluid Transport Characterization," *World Acad. Sci. Eng. Technol.*, vol. 5, no. 2, pp. 397–402, 2011.

[95] F. Pennella, G. Cerino, D. Massai, D. Gallo, G. Falvo D'Urso Labate, A. Schiavi, M. A. Deriu, A. Audenino, and U. Morbiducci, "A survey of methods for the evaluation of tissue engineering scaffold permeability," *Ann. Biomed. Eng.*, vol. 41, no. 10, pp. 2027–2041, 2013.

[96] T. Viana, S. Biscaia, H. A. Almeida, and P. J. Bártolo, "Permeability evaluation of lay-down patterns and pore size of PCL scaffolds," *Procedia Eng.*, vol. 59, pp. 255–262, 2013.

[97] V. P. Bogu, "Modelling and structural analysis of skull / cranial implant : beyond mid-line

deformities 2 . Modelling of an implant :," *Acta Bioeng. Biomech.*, vol. 19, no. 1, pp. 125–131, 2017.

[98] E. M. Lillie, J. E. Urban, A. A. Weaver, A. K. Powers, and J. D. Stitzel, "Estimation of skull table thickness with clinical CT and validation with microCT," *J. Anat.*, vol. 226, no. 1, pp. 73–80, 2015.

[99] T. Van Cleynenbreugel, J. Schrooten, H. Van Oosterwyck, and J. Vander Sloten, "Micro-CT-based screening of biomechanical and structural properties of bone tissue engineering scaffolds," *Med. Biol. Eng. Comput.*, vol. 44, no. 7, pp. 517–525, 2006.

[100] D. Yeon Kwon, J. Seon Kwon, S. Hun Park, J. Hun Park, S. Hee Jang, X. Yun Yin, J.-H. Yun, J. Ho Kim, B. Hyun Min, J. Hee Lee, W.-D. Kim, and M. Suk Kim, "A computer-designed scaffold for bone regeneration within cranial defect using human dental pulp stem cells," *Sci. Rep.*, vol. 5, no. 1, p. 12721, 2015.

[101] C. E. P. Aronin, K. W. Sadik, A. L. Lay, D. B. Rion, S. S. Tholpady, R. C. Ogle, and E. A. Botchwey, "Comparative effects of scaffold pore size, pore volume, and total void volume on cranial bone healing patterns using microsphere-based scaffolds," *J. Biomed. Mater. Res. - Part A*, vol. 89, no. 3, pp. 632–641, 2009.

[102] S. J. Simske and R. Sachdeva, "Cranial bone apposition and ingrowth in a porous nickel–titanium implant," *J. Biomed. Mater. Res.*, vol. 29, no. 4, pp. 527–533, 1995.

[103] R. Gasparini, T. Kosta, and I. Tsukanov, "Engineering analysis in imprecise geometric models," *Finite Elem. Anal. Des.*, vol. 66, pp. 96–109, 2013.

[104] S. Nelaturi and V. Shapiro, "Representation and analysis of additively manufactured parts," *Comput. Aided Des.*, vol. 67–68, pp. 13–23, 2015.

[105] N. Chantarapanich, P. Puttawibul, S. Sucharitpwatskul, P. Jeamwatthanachai, S. Inglam, and K. Sitthiseripratip, "Scaffold library for tissue engineering: A geometric evaluation," *Comput. Math. Methods Med.*, vol. 2012, no. 407805, p. 14, 2012.

9. LIST OF PUBLICATIONS

International Journals

1. Phanindra Bogu, V., Ravi Kumar, Y. & Kumar Khanra, A, "**Homogenous scaffold-based cranial /skull implant modelling and structural analysis—unit cell algorithm-meshless approach**", Medical & Biological Engineering & Computing (2017). Vol. 55 Issue 11, pp 2053-2065, Springer Publication. IF 1.9, DOI: 10.1007/s11517-017-1649-3.
2. Phanindra Bogu, V., Ravi Kumar, Y. & Kumar Khanra, A, "**Modelling and structural analysis of skull/cranial implant: beyond mid-line deformities**", Acta of Bioengineering & Biomechanics (2017). Vol. 19 Issue 1, p125-131, IF 0.9, DOI: 10.5277/ABB-00547-2016-04.
3. Phanindra Bogu, V., Ravi Kumar, Y. & Kumar Khanra, A, "**3D printed, customized cranial implant for surgical planning**," Journal of The Institution of Engineers (India): Series C (2016). pp 1–5, Scopus, Springer publication, DOI: 10.1007/s40032-016-0292-3.

International Conferences

1. V Phanindra Bogu, Madhu M N, Y Ravi kumar, K Asit Kumar, " **Design and analysis of various homogeneous interconnected scaffold structures for trabecular bone**", Proceeding of ISME-2017 organized by NIT Warangal, during 23-25 Feb 2017.

10. APPENDIX

10.1 Ansys meshing procedure

Open the STL file in Ansys ICEM CFD for meshing with tetrahedral element size 0.5mm, the procedure as fallows below

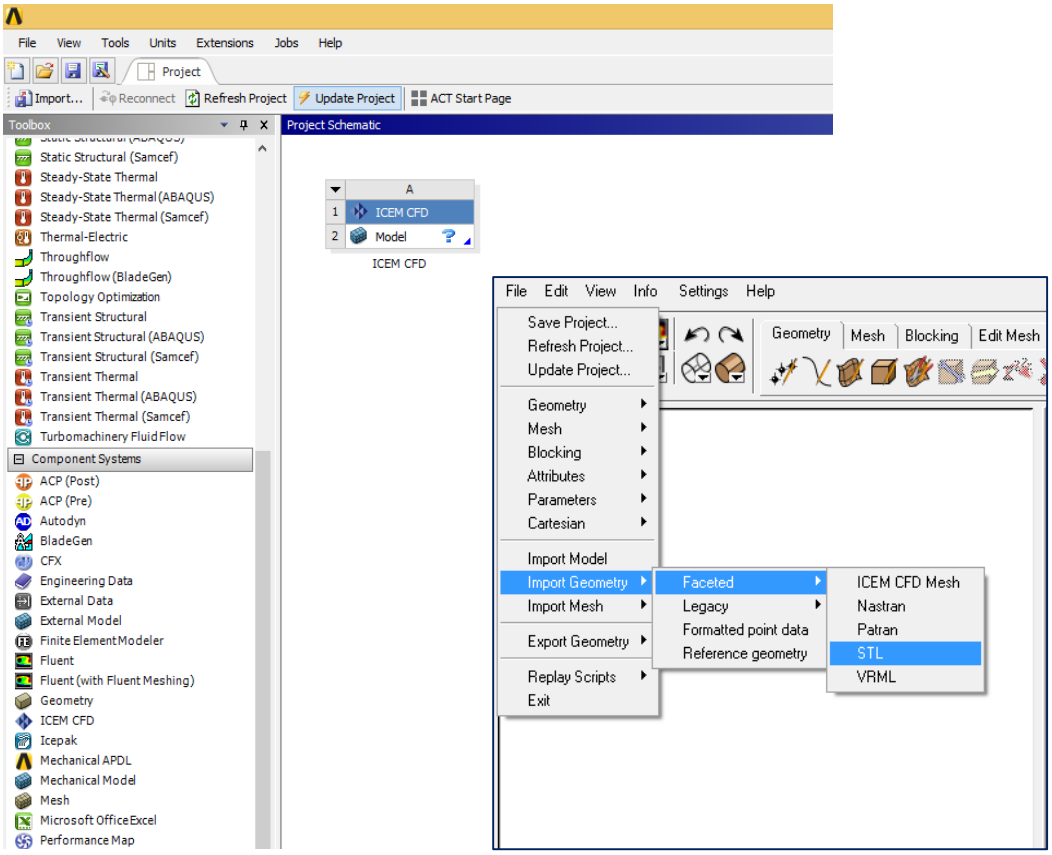

Global Mesh Size

The Global Mesh Size parameters affect meshers at the surface, volume, and inflation (prism) layer levels.

Global Element Scale Factor

Multiplies other mesh parameters to globally scale the model. For a list of parameters affected by this scale factor.

For example, if the **Max Element Size** of a given entity is 4 units, and the **Global Element Scale Factor** is 3.5, then the actual maximum element size used for meshing of that entity will be 4 *

3.5 = 14.0 units. The **Global Element Scale Factor** can be any positive real number, and it allows you to globally control the mesh size instead of changing the mesh parameters for different entities.

Global Element Seed Size

Max Element controls the size of the largest element. The largest element size in the model will not exceed the Max Element size multiplied by the Global Element Scale Factor.

If the **Max Element size** is set to 0, the Automatic Sizing feature will be implemented. Autosizing temporarily sets a Global Max Element size, which produces a uniform mesh, if no surface or curve sizes are smaller.

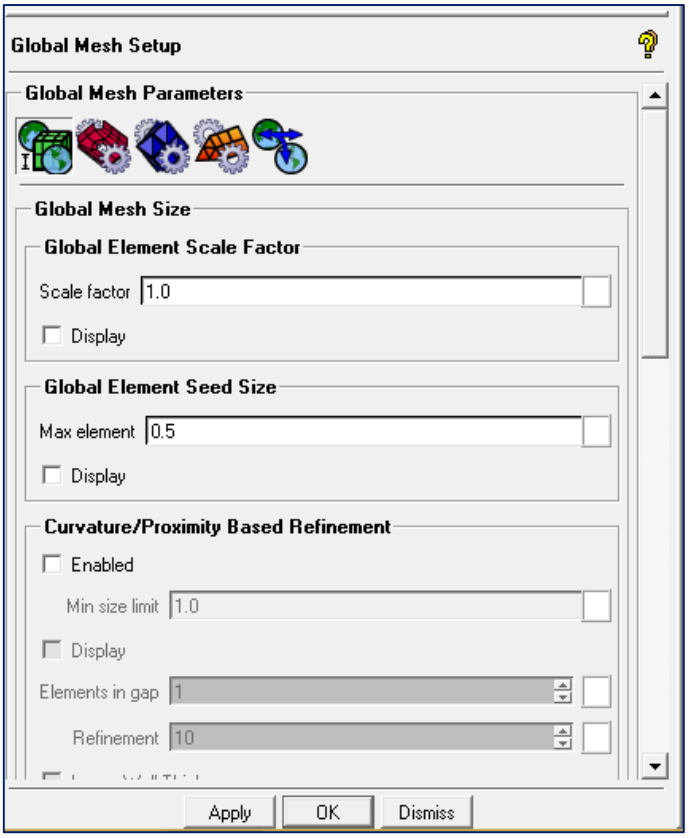

Volume Meshing Parameters

The Volume Meshing Parameters control the various volume meshing algorithms. Each mesh type has different options, as described in the following sections.

Tetra/Mixed

Hexa-Dominant

Cartesian

Tetra/Mixed

The following Mesh Methods are available for Tetra meshing:

Robust (Octree)

Quick (Delaunay)

Smooth (Advancing Front)

The Robust (Octree) option will generate a tetra mesh using a top-down meshing approach. An Octree mesher does not require an existing surface mesh because one is created by the Octree process. The top-down approach is start with very coarse approximation of original mesh then new points are inserted to generate better meshes. The bottom-up approach is start with original fine mesh then remove the elements (vertices, edges, triangles, tetrahedral) and replace with fewer elements.

Edge criterion

Determines to what extent a tetra is cut to represent geometry. The entered value is a factor of the tetra edge. After subdivision, if a tetra edge intersects an entity (surface), the tetra will be cut if the subdivision of the edge from the intersection is less than the prescribed value.

The values can range from 0 to 1. The geometry may not be properly captured if the value is larger (e.g., 0.5). Increasing the value will increase the nodes moving to fit to the geometry. Reducing the value will increase refinement near entities, and will also reduce non-manifold vertices in trailing edges. The default of 0.2 is adequate for most cases. This value is useful in cases where thin cuts fail or are difficult to setup.

Smooth mesh

When enabled, the mesh is smoothed after finishing subdivision down to the specified mesh sizes.

Iterations

Number of iterations to be performed for the smoothing to match the supplied Min quality.

Min Quality

All elements with quality less than the specified value will be smoothed. The default is 0.4.

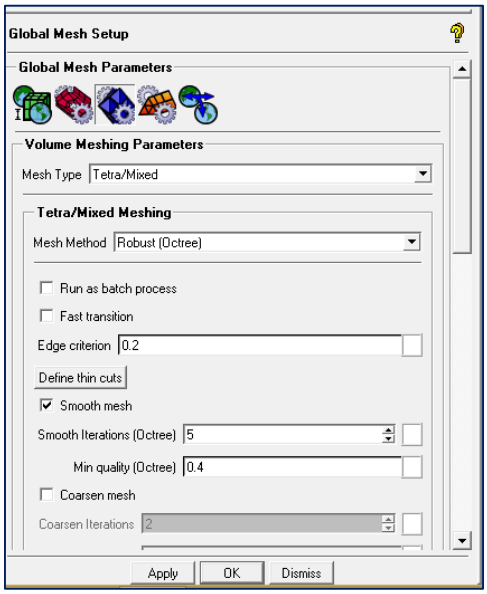

Compute Mesh

The Compute Mesh option allows you to generate the mesh specified by the mesher and various parameters.

Compute Volume Mesh

The Compute Volume Mesh option generates a volume mesh using the selected volume mesh type and method. The descriptions of the different options and their parameters are described in Global Mesh Setup > Volume Meshing Parameters. The volume mesh will be applied using the parameters that are set there.

Load mesh after completion

This option applies to all the Compute Volume Mesh options. If disabled, the surface mesh will not be loaded into the GUI. This may be useful for big models.

Tetra/Mixed Mesh Type

There are four different Mesh Methods available for Tetra/Mixed Meshing: Robust (Octree), Quick (Delaunay), and Smooth (Advancing Front).

Compute the mesh, click ok

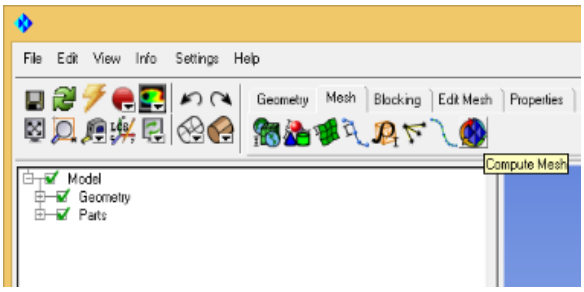

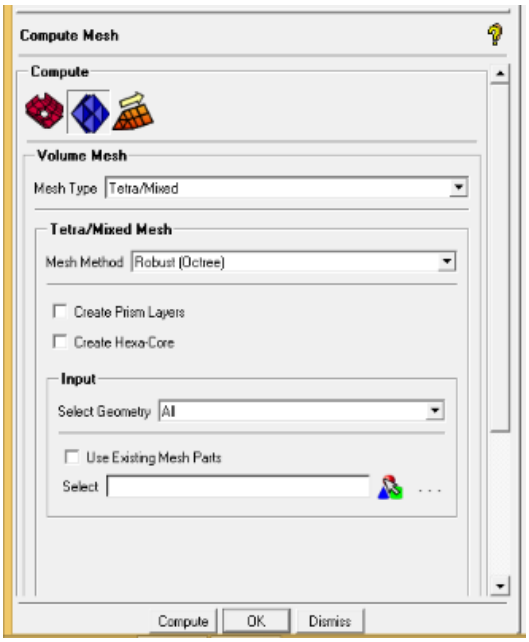

Open the mesh file in static structural Ansys software.

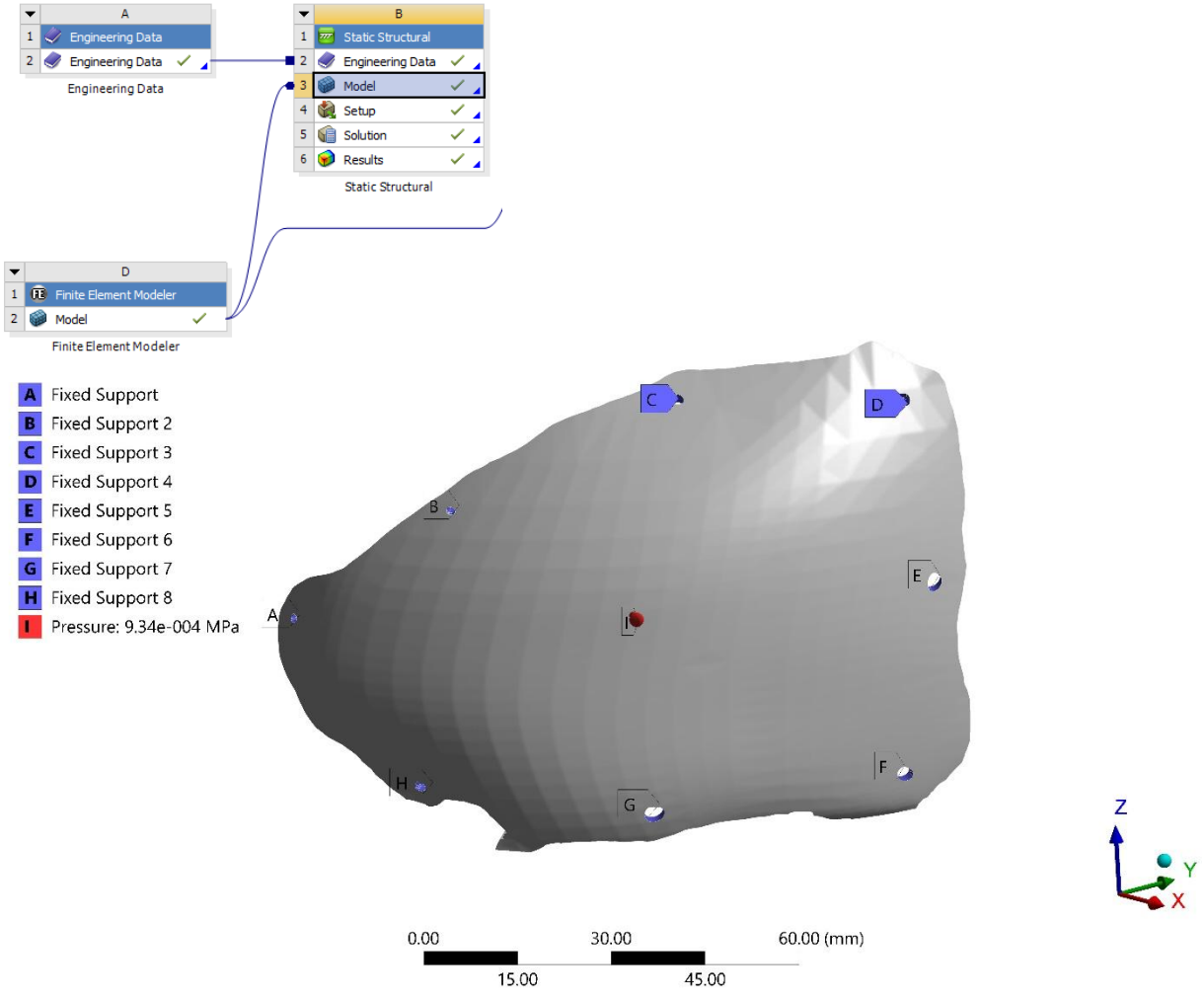

10.2 Finite element analysis vs Meshless approach

Bounding Box	
min. corner	{0, 0, 0}
max. corner	{100, 10, 10}

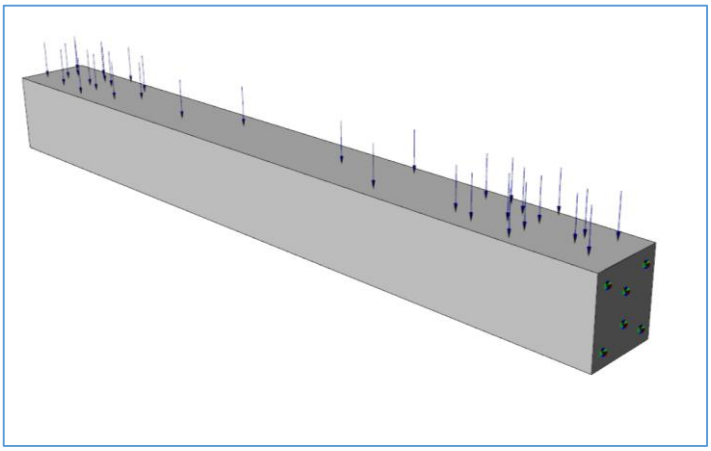

Material Properties

Property	Value
Description	Ti6Al4V
Density	4.43e-09 Kg/mm^3
Elastic Modulus	110000 MPa
Poisson Ratio	0.3
Tensile Yield Strength	800 MPa
Ultimate Tensile Strength	950 MPa

The line pressure is (P) = 5 N/mm

The length of the beam (L) = 100 mm

The force (w) = P*L= 500N

The fixed Beam deflection formula = $\frac{5WL^4}{384EI} = \frac{5wL^3}{384EI} = \frac{5*500*100^3}{384*110000*833.33} = 0.07104$ mm

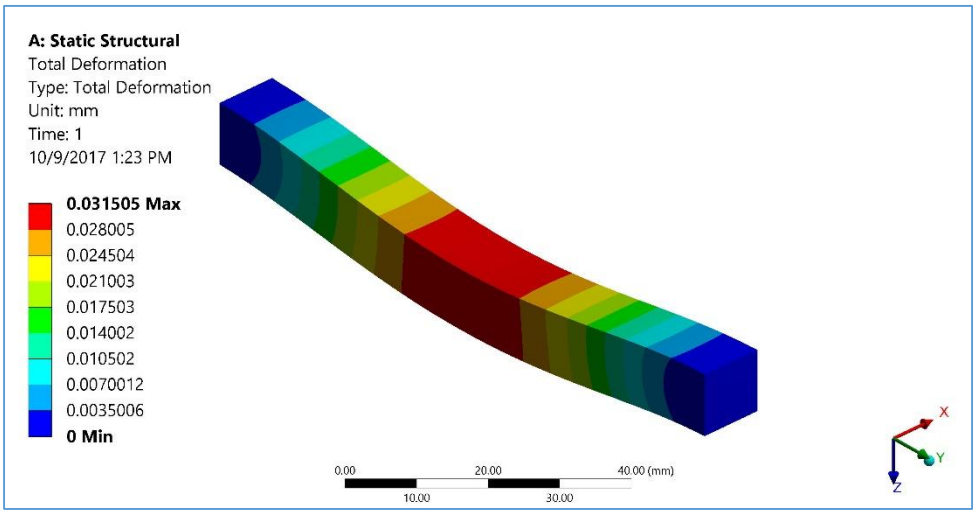

Figure.1 Analysis of fixed beam (solid) in Ansys software

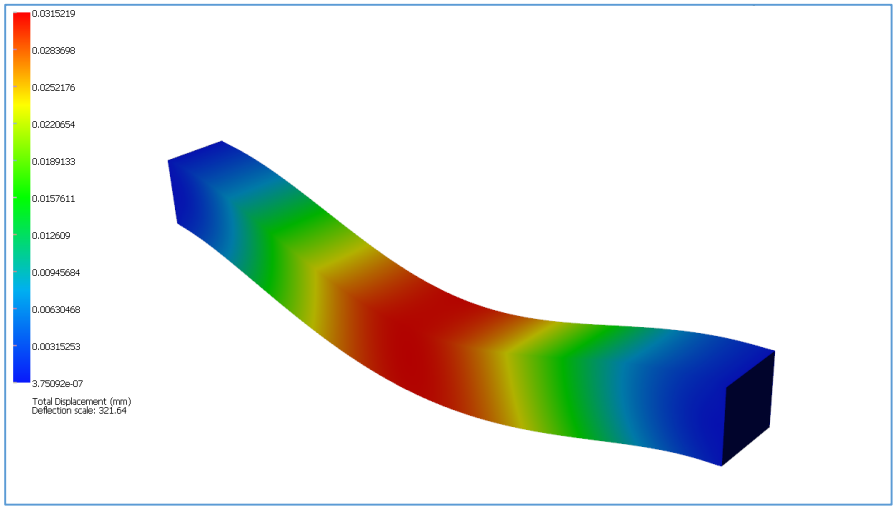

Figure.3 Analysis of fixed beam (solid) in meshless software

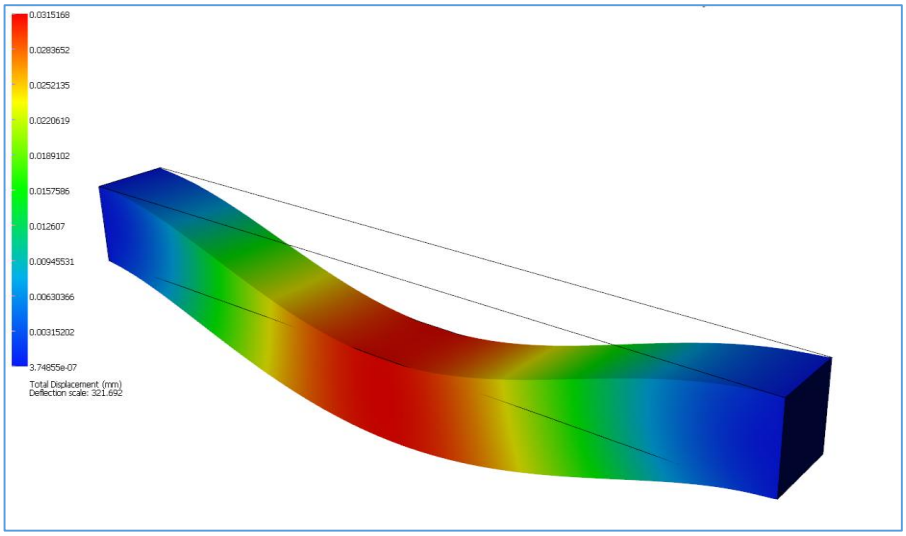

Figure.2 Analysis of fixed Beam (STL file) in Meshless software

10.3 Comparison of FEM Vs Meshless

We compared the results of FEM vs mesh less approach, for cranial implant (STL file). In Ansys software the implant is meshed with 2.3 million elements and done the simulation. The same implant is simulated in this scan&solve software at different elements levels (i.e below 500000), typically the same results were found at few No.of elements. The data presented in below table.

Data:

Material		FEM	Meshless
Titanium	Total Deformation	6.2244e-5 mm	6.76917e-5 mm
Titanium	Total Deformation	3.16107e-5 mm	2.9068e-5 mm

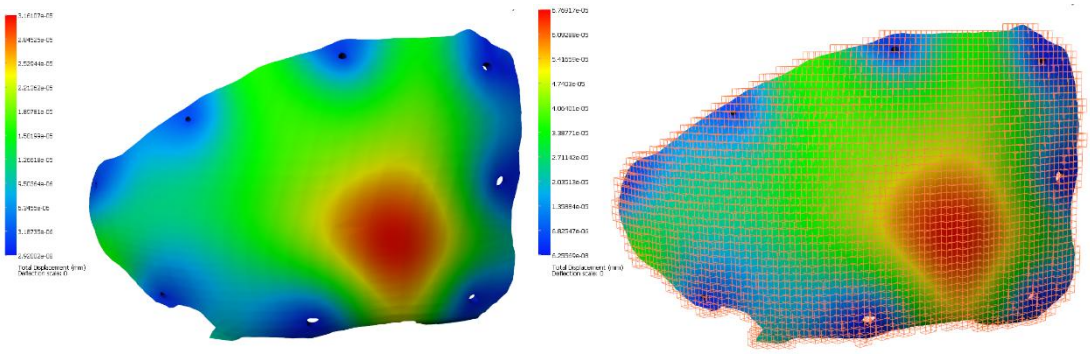

Figure: MESHLESS: Left: 8 fixation point at min load **Right**: 8 fixation point at max

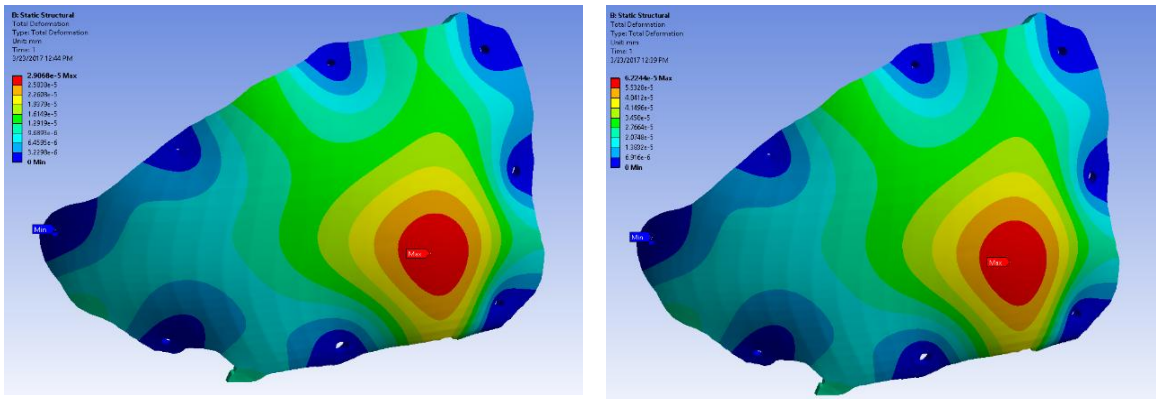

Figure: ANSYS: **Left**: 8 fixation point at min load **Right**: 8 fixation point at max load

10.4 Validation of results

Type 2: The element size is maintained at different levels of 0.46 mm, 0.38 mm and the percentage of change in results is below 1%.

Type of implant	Volume	Material	Loading data	Total Deformation		
				Element size =0.46mm	Element size =0.38mm	% of change
Type 2 (Strut radius = 0.15 mm)	7120.95 mm^3	Ti6Al4V	Minimum	2.17338e-05 mm	2.16732e-05 mm	0.28
			Maximum	4.65594e-05 mm	4.64109e-05 mm	0.32
		PEEK	Minimum	5.57223e-04 mm	5.55668e-04 mm	0.28
			Maximum	1.18103e-03 mm	1.17891e-03 mm	0.18

Type of implant	Volume	Material	Loading data	Equivalent stress (Von-Mises stress)		
				Element size =0.46mm	Element size =0.38mm	% of change
Type 2 (Strut radius = 0.15 mm)	7120.95 mm^3	Ti6Al4V	Minimum	0.417041 MPa	0.416292 MPa	0.18
			Maximum	0.893904 MPa	0.891409 MPa	0.28
		PEEK	Minimum	0.373018 MPa	0.369801 MPa	0.87
			Maximum	0.79757 MPa	0.790378 MPa	0.91

Type 5: The element size is maintained at different levels of 0.52 mm, 0.44 mm and the percentage of change in results is below 1%.

Type of implant	Volume	Material	Loading data	Total Deformation		
				Element size =0.52mm	Element size =0.44mm	% of change
Type 5 (Strut radius = 0.3 mm)	14426.9 mm^3	Ti6Al4V	Minimum	7.6423e-06 mm	7.59672e-06 mm	0.6
			Maximum	1.63679e-05 mm	1.62671e-05 mm	0.62
		PEEK	Minimum	1.97595e-04 mm	1.96965e-04 mm	0.32
			Maximum	4.23874e-04 mm	4.21766e-04 mm	0.5

Type of implant	Volume	Material	Loading data	Equivalent stress (Von-Mises stress)		
				Element size =0.52mm	Element size =0.44mm	% of change
Type 5 (Strut radius = 0.3 mm)	14426.9 mm^3	Ti6Al4V	Minimum	0.301133 MPa	0. 298595MPa	0.85
			Maximum	0.643864 MPa	0.639389 MPa	0.7
		PEEK	Minimum	0.260375 MPa	0.258797 MPa	0.61
			Maximum	0.559267 MPa	0.554169 MPa	0.92